Empowering Antibiotic Polymer Design through Coarse-Grained Molecular Dynamics

Gabriel Nascimento Serafim

Thesis to obtain the Master of Science Degree in

Bioengineering and Nanosystems

Supervisor(s): Dr. Manuel Nuno de Sousa Pereira Simões de Melo
Dr. Vasco Daniel Bigas Bonifácio

Examination Committee

Chairperson: Prof. Dr. Gabriel António Amaro Monteiro
Advisor: Dr. Manuel Nuno de Sousa Pereira Simões de Melo
Members of the Committee: Prof. Dr. Rita Alexandra do Nascimento Cardoso Guedes

December 2020

PREFACE

The work presented in this thesis was performed at the Multiscale Modeling Lab at Instituto de Tecnologia Química e Biológica António Xavier from Universidade Nova de Lisboa (Oeiras, Portugal), during the period of 08/2019 - 10/2020, under the supervision of Dr. Manuel Nuno de Sousa Pereira Simões de Melo. The thesis was co-supervised in the BSIRG group at Institute for Bioengineering and Bioscience from Instituto Superior Técnico (Lisbon, Portugal) by Dr. Vasco Daniel Bigas Bonifácio, Dr. Nuno Martinho and Dr. Sandra Pinto.

I declare that this document is an original work of my own authorship and that it fulfills all the requirements of the Code of Conduct and Good Practices of the Universidade de Lisboa.

ACKNOWLEDGMENTS

First of all I would to thank my supervisors, Dr. Manuel Nuno Melo and Dr. Vasco Bonifácio. Vasco, thank you for giving me the opportunity to work with such a fascinating nanoparticle. *Manel*, thank you for guiding me through this amazing field of Molecular Dynamics and for giving me all the tools and knowledge to be successful. I hope I have met your expectations.

I also want to extended my thank you to Dr. Sandra Pinto and Dr. Nuno Martinho for all the support and help expended with me during this project.

I would like to thank all my colleagues from IST and ITQB. Thank you for helping to transform Portugal into my home during these last 2 years.

I would also like to acknowledge the financial support from Fundação para a Ciência e a Tecnologia (FC&T) through projects PTDC/MEC-ONC/29327/2017, UIDB/04612/2020 and UIDP/04612/2020.

To my closest friends, thank you for all the support and incentives along my journey. Your were essential to keep me going trough this dark times. Love you all.

José and Lea Scheinkman, my godparents, thank you for making sure that a kid like me would be able to fight as equals to others. I am a luck guy to have you both as my family. This Masters is for you.

Raimunda, my mom, thank you for being the ultimate example of what a human being should be. Everything that I've done and do is to make you proud and I am sure that I am in the right path to do so.

Clarice, my lifemate, thank you for being by my side and encourage me to always seek to evolve and be better. I'm grateful to share my life with you. *Te amão demais*.

ABSTRACT

Antibiotic resistance traits appear when bacteria are still able to grow in the presence of therapeutic concentration of antibiotic drugs. The continuous misuse of these drugs coupled with the lack of incentives for the development of new drugs by pharmaceutical industry urge the need for alternatives to counter the current antibiotic crisis. The development of bio-mimetic polymer based upon host defense peptides characteristics is a field with a lot of potential.

In this work, a coarse-grain Martini model of a therapeutic nanoparticle, consistent of a polyurea dendrimer core with oligo(ethylenimine) chains coupled to it, was built and tested against models of phospholipids bilayer membranes in search of understanding what are the possible mechanisms that provide its antimicrobial activity. Furthermore, from these analysis, three modifications to this nanoparticle were tested with the objective of improving the previous outcome.

The results showed that when the nanoparticle has a positive net charge, it presents the desired selectivity towards anionic membrane model, causing negative curvatures that can induce further permeabilization and/or disruption. The insertion of one of the modifications increased the hydrophobic content of the nanoparticle and improved the distance between the nanoparticle and the center of the membrane, without losing the desired selectivity. The ability to modified the ions distribution of the system can be an indicative of a different mode of action.

Keywords: Antibiotics, Poly(ethylenimine), Polyurea dendrimer, Molecular Dynamics, Lipid membrane, Martini Coarse-grain Model.

RESUMO

Os traços de resistência aos antibióticos aparecem quando as bactérias são capazes de crescer na presença de concentrações terapêuticas de medicamentos antibióticos. O contínuo uso indevido desses medicamentos em conjunto com a falta de incentivos para o desenvolvimento de novos medicamentos pela indústria farmacêutica, impõe a necessidade de alternativas para conter a atual crise de antibióticos. O desenvolvimento de polímeros biomiméticos com base nas características de peptídeos de defesa do hospedeiro é um campo com muito potencial.

Neste trabalho, um modelo coarse-grain Martini de uma nanopartícula terapêutica, que consiste de um núcleo de dendrímero de poliureia com cadeias acopladas de oligo(etilenimina), foi construído e testado contra modelos de membrana fosfolipídica para compreender quais os possíveis mecanismos que proporcionam a sua actividade antimicrobiana. Além disso, a partir de análises, três modificações nessa nanopartícula foram testadas com o objetivo de melhorar os resultados anteriores.

Os resultados mostraram que quando a nanopartícula tem uma carga líquida positiva, ela apresenta a seletividade desejada em relação ao modelo de membrana aniônica, causando curvaturas negativas que podem induzir uma maior permeabilização e/ou rompimento. A inserção de uma das modificações aumentou o conteúdo hidrofóbico da nanopartícula e melhorou a distância entre a nanopartícula e o centro da membrana, sem perder a seletividade desejada. A capacidade de modificar a distribuição de íons do sistema pode ser um indicativo de um modo de ação diferente.

Palavras-chave: Antibióticos, Poli(etilenimina), Dendrímero de poliureia, Dinâmica Molecular, Membrana lipídica, Modelo Coarse-Grain Martini.

TABLE OF CONTENTS

Preface **i**

Acknowledgments **iii**

Abstract **v**

Resumo **vii**

Table of Contents **ix**

List of Tables **xiii**

List of Figures **xvii**

List of Abbreviations **xxiii**

1 Introduction **1**

1.1 Antibiotics crisis 1

1.2 Alternatives for antibiotics 4

1.2.1 Bio-mimetic polymers 5

1.2.2 Poly(ethylenimine) 6

1.3 Molecular Dynamics 8

1.3.1 Coarse-grained models 12

1.4 Objectives 14

2 Methods **15**

2.1 Poly(ethylenimine) parameterization within the Amber and Martini FF 15

2.1.1 Optimization of partial atomic charges of PEI tetramers 17

2.2 Polyurea dendrimer parameterization within Martini 3 FF 18

2.3 PURE$_{G4}$-OEI$_{48}$ building process 18

2.4 All-atom Molecular Dynamics simulations 19

2.5 Coarse-grained Molecular Dynamics simulations 19

2.6 Molecular Dynamics simulations with membrane models 19

2.7 End-to-end distance, D_{ee} 20

2.8 Radius of Gyration, R_g 20

2.9 Shape Parameter, S and Asphericity, Δ 21

2.10 Distance-to-core and contacts analysis 22

2.11 Radial distribution function, $g(r)$ 22

3 Results **23**

3.1 Poly(ethylenimine) parameterization within the Amber FF 23

3.1.1 Optimization of partial atomic charges 23

3.1.2 Atom type designation and Lennard-Jones parameters by similarity 23

3.1.3 Optimization of dihedral parameters 23

3.2 Poly(ethylenimine) all-atom Molecular Dynamics 25

3.2.1 Radius of gyration and end-to-end distance analysis 26

3.3 Poly(ethylenimine) mapping 27

3.4 Poly(ethylenimine) parameterization within Martini 3 FF 28

3.5 Comparison between Amber and Martini 3 behavior 31

3.6 Polyurea dendrimer mapping 33

3.7 Polyurea dendrimer parameterization 34

3.8 Nanoparticle's structure 36

3.9 Nanoparticle at the membrane environment 37

3.9.1 Visual analysis 38
3.9.2 Membrane distance and contacts' assay 39
3.9.3 System's ionic distribution 40
3.10 Proposed modifications 43
3.10.1 Structural analysis 44
3.10.2 Membrane distance, contact and ionic distribution vs. original PURE$_{G4}$-OEI$_{48}$ 45

4 Discussion **51**

5 Conclusions **53**

References **55**

Appendix A Partial atomic charges **65**

Appendix B Force fields parameters **67**

Appendix C RDF plots **71**

LIST OF TABLES

1.1 Examples of resistance modes of different classes of antibiotics. Adapted from [7]. 3

3.1 Atom type and Lennard-Jones parameters 23

3.2 Average end-to-end distance, $\langle D_{ee} \rangle$ (nm) 26

3.3 Average radius of gyration, $\langle R_g \rangle$ (nm) 26

3.4 Computed–experimental comparison of end-to-end distance and radius of gyration for PEI 50-mer under no salt conditions 27

3.5 Torsion potential parameters for dihedrals of fully-protonated linear PEI. All values are in kJ mol^{-1} 31

3.6 Average Radius of gyration (in Å), Shape parameters and Asphericity comparison between Atomistic and Coarse-grained topologies for PURE$_{G4}$. 36

3.7 Average Radius of gyration (in Å), Shape parameters and Asphericity of all three state of protonation from PURE$_{G4}$-OEI$_{48}$. 37

3.8 Martini 3 parameters for connection between dendrimer, amino acids and OEI chains. b_0 in nm, k_b in kJ·mol^{-1}·nm^{-2}, θ_0 in degrees and k_θ in kJ/mol. 44

3.9 Comparison between the attributes of the original PURE$_{G4}$-OEI$_{48}$ and the suggested modifications. 44

A.1 *pei*+ final charges 65

A.2 *peis* final charges 65

A.3 *pein* final charges 66

A.1 AMBER final dihedral parameters for all protonation states. Shifts angles ϕ_s in degrees, force constants k_ϕ in kcal/mol and multiplicities n_i. 67

A.2 Martini 3 bond parameters for all PEI models. b_0 in nm and k_b in kJ·mol^{-1}·nm^{-2}. 67

A.3 Martini 3 bending angle parameters for all PEI models. θ_0 in degrees and k_θ in kJ·mol^{-1}. 67

A.4 Martini 3 torsion angle parameters for all PEI models. All values in kJ·mol^{-1}. 68

A.5 Martini 3 bond and angle parameters for Polyurea models. b_0 in nm, k_b in kJ·mol^{-1}·nm^{-2}, θ_0 in degrees and k_θ in kJ·mol^{-1}. 68

LIST OF FIGURES

1.1 Antibiotic discovery and resistance timeline. Left side shows discovery of a specific antibiotic and right side points when the resistance was detected. Adapted from [16]. 2

1.2 Distribution of AMPs entries in respect to percentage of hydrophobic amino acids, net charge and chain size, respectively. Adapted from [26] 4

1.3 Evolution of antimicrobial polymers. The main difference between HDP and polymeric disinfectants are highlighted in the first two boxes. Evolution of both fields lead to the development of HDP-inspired antimicrobial polymers. Adapted from [26] 5

1.4 Butylamine and guanidine groups from Lysine (left) and Arginine (right) amino acids. 6

1.5 a) Ethylene imine monomer, b) linear PEI fragment, c) Branched PEI fragment and d) Second-generation PEI dendrimer. 7

1.6 Evolution of MD publications related to Structural Biology. Adapted from [56]. 9

1.7 Global MD Algorithm. The sequence of steps consist in: 1) input of initial conditions (potential interactions, positions and velocities); 2) computation of forces from bonded and non-bonded interactions between atoms; 3) derivation of new positions and velocities for each atom; 4) storing of desired output. Adapted from [58]. 11

1.8 Example of a FF model. The potential energy will be the sum of the energies related to: A) stretching or compressing of bonded pair of atoms (modeled by a simple spring), B) Increasing or decreasing bond angle formed between three consecutive atoms (modeled by a simple harmonic), C) dihedral angle rotations defined by four consecutive atoms (also modeled by a simple harmonic), D) van der Waals interactions (modeled by Lennard–Jones potential) and E) Electrostatic interactions (modeled by Coulomb's law). The interactions from A) to C) represent the ones from chemically bonded atoms, while D) and E) are the ones from non-bonded atoms. Adapted from [52] 11

1.9 Martini mapping examples of selected molecules: (A) Standard water particle representing four water molecules, (B) Polarizable water molecule with embedded charges, (C) DMPC lipid, (D) Polysaccharide fragment, (E) Peptide, (F) DNA fragment, (G) Polystyrene fragment, (H) Fullerene molecule. In all cases Martini CG beads are shown as cyan transparent beads overlaying the atomistic structure. Taken from [62] 13

2.1 PEI models used in the parameterization of the Amber FF. Dark blue represents nitrogen atoms, cyan represents carbons and white represents hydrogens. a) fully-protonated tetramer b) semi-protonated tetramer and c) non-protonated tetramer. 16

3.1 QM and MM potential torsion energy fit for tetramer *pei*+. 24

3.2 QM and MM potential torsion energy fit for tetramer *peis*. 24

3.3 QM and MM potential torsion energy fit for tetramer *pein*. 25

3.4 Snapshot of a typical configuration of a fully-protonated PEI 49-mer (red dots correspond to Na^+ and green to Cl^-). 26

3.5 Mapping scheme for fully-protonated PEI chains. Blue bead represents TBP (or TBN for non-protonated chains) and green represents MBP (or MBN for non-protonated and semi-protonated chains). 28

3.6 Atomistic (solid) and CG (dashed) probability distribution for the TBP-MBP (black) and MBP-MBP (red) bead bond distances. 29

3.7 Atomistic (solid) and CG (dashed) probability distribution for the TBP-MBP-MBP (black) and MBP-MBP-MBP (red) bending angles. 30

3.8 Atomistic (solid) and CG (dashed) probability distribution for the a) TBP-MBP-MBP-MBP (black) and b) MBP-MBP-MBP-MBP (red) torsion angles. 31

3.9 End-to-end distance and radius of gyration for PEI chains under no salt condition. AA values are represented by full circles and continuous lines while CG are void circles with dashed lines. 32

3.10 End-to-end distance and radius of gyration for PEI chains under 150mM of NaCl. AA values are represented by full circles and continuous lines while CG are void circles with dashed lines. 32

3.11 Partial structure of the $PURE_{G4}$ core (second generation shown). Dashed lines represent further repeating units. 33

3.12 AM (amine; red) and UR (urea; blue) beads that represent the general mapping choice for the $PURE_{G4}$ dendrimer. Three extra red circles represent the amine groups of the dendrimer's next generation. 34

3.13 Atomistic (solid) and CG (dashed) probability distribution for all bonds' distances. 35

3.14 Atomistic (solid) and CG (dashed) probability distribution for all bending angles. 35

3.15 Atomistic probability distribution for all torsion angles. 36

3.16 Average representation of $PURE_{G4}$-OEI_{48} in all three different protonation state. 37

3.17 Side and top view of PURE$_{G4}$-OEI$_{48}$ interaction with POPC/POPG membrane, where red represents the dendrimer core, blue the OEI chains, gray the PO$_4$$^-$ beads from POPG and brown PO$_4$$^-$ from POPC. 38

3.18 Distance-to-core distribution for PURE$_{G4}$-OEI$_{48}$ and POPC/POPG (solid) or POPC (dashed) membranes, at the three protonation levels. 40

3.19 Percentage of a PURE$_{G4}$-OEI$_{48}$ nanoparticle's beads in contact with either POPC/POPG (red) or POPC (blue) membranes. 41

3.20 Radial distribution function of ions around outer leaflet of membranes under presence of fully-protonated PURE$_{G4}$-OEI$_{48}$. Note that in b) the Na$^+$ plots completely superimpose at distances below 7 Å, as do the plots for Cl$^-$. 42

3.21 Coarse-grained representation of chosen amino acids. Adapted from [106]. 44

3.22 Structures for all modifications of PURE$_{G4}$-OEI$_{48}$, in all three different protonation states. Amino acids are represented in green color. 45

3.23 Distances probability of non-protonated nanoparticles at POPC/POPG (solid) and POPC(dashed) membranes. 46

3.24 Distances probability of fully-protonated nanoparticles at POPC/POPG (solid) and POPC(dashed) membranes. 47

3.25 Distances probability of semi-protonated nanoparticles at POPC/POPG (solid) and POPC (dashed) membranes. 47

3.26 Percentage of contacts for all nanoparticle modifications and state of protonation at POPC/POPG membranes. 48

3.27 Trajectory views of fully-protonated Phenylalanine mod PURE$_{G4}$-OEI$_{48}$ interaction with POPC/POPG and POPC membranes. 49

3.28 Trajectory views of fully-protonated Leucine and Tryptophan mods PURE$_{G4}$-OEI$_{48}$ interaction with POPC/POPG membranes. 49

3.29 Trajectory views of semi-protonated mods PURE$_{G4}$-OEI$_{48}$ interaction with POPC/POPG membranes. 50

A.1 Atomistic (solid) and CG (dashed) probability distribution for the TBP-MBN (black) and MBN-MBP (red) bead bond distances of semi-protonated PEI. 68

A.2 Atomistic (solid) and CG (dashed) probability distribution for the TBP-MBN-MBP (black), MBN-MBP-MBN (red) and MBP-MBN-MBP (green) bending angles of semi-protonated PEI. 69

A.3 Atomistic (solid) and CG (dashed) probability distribution for the TBP-MBN-MBP-MBN (black) and MBN-MBP-MBN-MBP (red) dihedral angles of semi-protonated PEI. 69

A.4 Atomistic (solid) and CG (dashed) probability distribution for the TBN-MBN (black) and MBN-MBN (red) bead bond distances of non protonated PEI. 69

A.5 Atomistic (solid) and CG (dashed) probability distribution for the TBN-MBN-MBN (black) and MBN-MBN-MBN (red) bending angles of non protonated PEI. 70

A.6 Atomistic (solid) and CG (dashed) probability distribution for all the dihedrals angles of non protonated PEI. 70

A.1 Radial distribution function of ions around outer leaflet of membranes under presence of semi-protonated PURE$_{G4}$-OEI$_{48}$. 71

A.2 Radial distribution function of ions around outer leaflet of membranes under presence of non-protonated PURE$_{G4}$-OEI$_{48}$. 71

A.3 Radial distribution function of ions around outer leaflet of membranes under presence of all Leucine modification PURE$_{G4}$-OEI$_{48}$. 72

A.4 Radial distribution function of ions around outer leaflet of membranes under presence of all Phenylalanine modification PURE$_{G4}$-OEI$_{48}$. 73

A.5 Radial distribution function of ions around outer leaflet of membranes under presence of all Tryptophan modification PURE$_{G4}$-OEI$_{48}$. 74

LIST OF ABBREVIATIONS

AA All-atom.

AMP Antimicrobial peptide.

BAC Benzalkonium chlorides.

CG Coarse-grained.

CL Cardiolipin.

ESP Electrostatic potential.

FF Force field.

HDP Host defense peptide.

Leu Leucine.

MD Molecular Dynamics.

MM Molecular mechanics.

OEI Oligo(ethylenimine).

PAMAM Poly(amidoamine).

PEI Poly(ethylenimine).

pei+ poly(ethylenimine) tetramer model with all nitrogens protonated.

pein poly(ethylenimine) tetramer model non-protonated nitrogens.

peis poly(ethylenimine) tetramer model with alternately protonated nitrogens.

Phe Phenylalanine.

PL Phospholipid.

POPC 1-palmitoyl-2-oleoyl-sn-glycero-3-phosphocholine.

POPG 1-Palmitoyl-2-oleoyl-sn-glycero-3-(phospho-rac-(1-glycerol)).

QAS Quaternary ammonium salt.

QM Quantum mechanics.

RBC Red blood cell.

RDF Radial distribution function.

RESP Restrained electrostatic potential.

RMS Root mean square.

RMSE Root mean square error.

Trp Tryptophan.

CHAPTER 1 - INTRODUCTION

1.1 Antibiotics crisis

Antibiotics can be defined as substances that are used to treat or prevent infections by killing or inhibiting the growth of bacteria. These molecules can be obtained by isolates from cultures of certain microorganisms (such as fungi) or by semi-synthetic or synthetic origin [1]. They might act by inhibiting the microbial synthesis of the cell wall, protein or nucleic acids (DNA or RNA); by acting as a membrane disorganizing agent or through other specific actions [2]. Antibiotics may also enter the cell wall of bacteria by binding to them and then use energy dependent transport mechanisms in ribosomal sites, which subsequently leads to the inhibition of protein synthesis [3]. The use of these substances to combat infections, caused by different types of microbes, has saved millions of lives along history, and allowed the development of human society as it is.

Contrary to the common belief that the exposure to antibiotics is confined to the modern “antibiotic era”, research has revealed that this is not the case [4]. Traces of tetracycline have been found in human skeletal remains from ancient Sudanese Nubia dating back to 350 – 550 BC [5] and from histological study of samples from late Roman period of Dakhleh Oasis in Egypt [6].

For decades, multiple varieties of antibiotics have not only been used for therapeutic purposes but also as prophylactic practice across other industries such as agriculture and animal husbandry. This is possible due to theirs ability to target the microorganism responsible for the infection without having effects to the host [7]. In the past decades the production of new classes of antibiotics has increased exponentially due to the demand across many sectors and allowed for less expensive and off-label drugs. As a side effect, the wide availability of different compounds that possess antimicrobial properties and increased irresponsible use of these drugs have contributed significantly to the advent of resistant strains of microbes [8] and the reduction of their capability to fight infections caused by those microorganisms [8].

Antibiotic resistance traits appear when bacteria are still able to grow in the presence of therapeutic concentration of antibiotic drugs [7]. This feature is developed by the natural evolutive selection process, where a stress environment pressures and selects the microbes with mutations [9] that lead to antibiotic resistance [3]. The more frequent the use of these types of drugs, the higher will be the probability for natural selection to act and select the mutant variants with antibiotic resistance traits [10]. It is important to highlight that since this is an evolutive process, the same species of microbe can evolve in different directions. While one study shows that medicines like sulfamethoxazole, trimethoprim, ampicillin and tetracycline no longer have the capability to fight non-cholera diarrhea disease in Thailand [11], the same drugs are still effective in the treatment of the same disease in Bangladesh [12].

In the last century, with the development and introduction of new antibiotics, new types of resistance have emerged. Introduction of sulfonamides in 1937 led to the development of resistance mechanisms that are still present nowadays [8]. Within six years of the first production of the aminoglycosides, aminoglycoside resistant strains of *Staphylococcus aureus* appeared [13]. Introduced in 1960s, Methicillin was the first of the semi-synthetic penicillinase-resistant antibiotic to target strains of penicillinase-producing *Staphylococcus aureus*. However, resistance to methicillin was reported soon after its initiation [14]. In recent years, clinical isolates of Vancomycin-resistant *Staphylococcus aureus* were found in 2002, after 44 years of its introduction to the market [15]. A detail timeline of antibiotic discovery and resistance events can be seen in Figure 1.1.

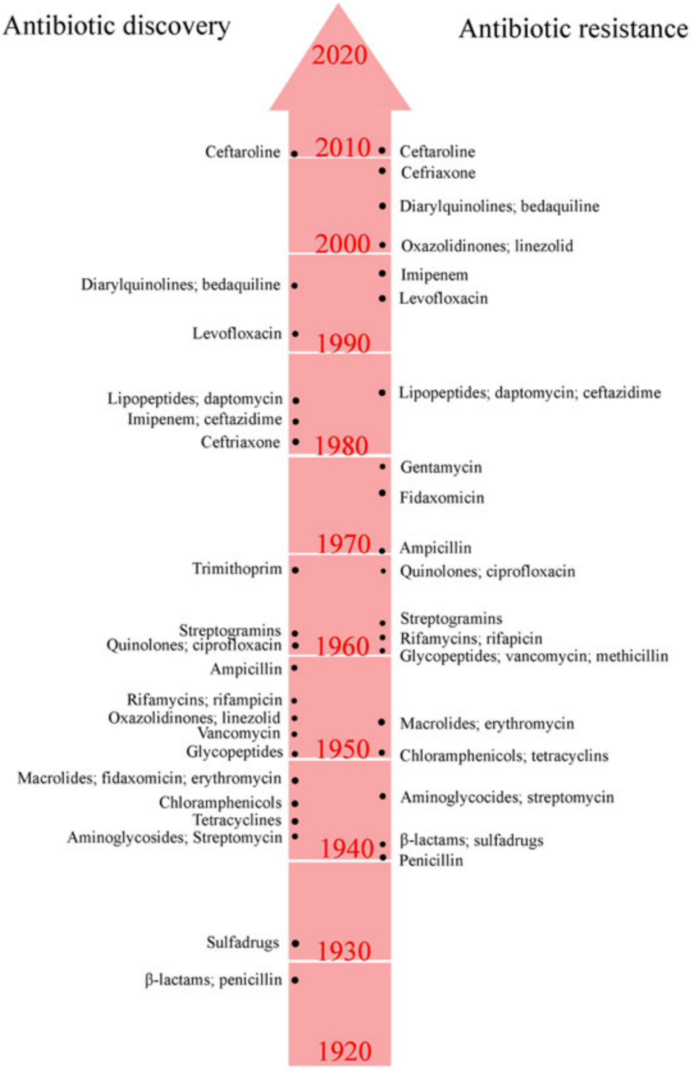
Antibiotic discovery
Antibiotic resistance
2020
2010
2000
1990
1980
1970
1960
1950
1940
1930
1920
Ceftaroline
Diarylquinolines; bedaquiline
Levofloxacin
Lipopeptides; daptomycin
Imipenem; ceftazidime
Ceftriaxone
Trimithoprim
Streptogramins
Quinolones; ciprofloxacin
Ampicillin
Rifamycins; rifampicin
Oxazolidinones; linezolid
Vancomycin
Glycopeptides
Macrolides; fidaxomicin; erythromycin
Chloramphenicols
Tetracyclines
Aminoglycosides; Streptomycin
Sulfadrugs
β-lactams; penicillin
Ceftaroline
Cefriaxone
Diarylquinolines; bedaquiline
Oxazolidinones; linezolid
Imipenem
Levofloxacin
Lipopeptides; daptomycin; ceftazidime
Gentamycin
Fidaxomicin
Ampicillin
Quinolones; ciprofloxacin
Streptogramins
Rifamycins; rifapicin
Glycopeptides; vancomycin; methicillin
Macrolides; erythromycin
Chloramphenicols; tetracyclins
Aminoglycocides; streptomycin
β-lactams; sulfadrugs
Penicillin

Figure 1.1: Antibiotic discovery and resistance timeline. Left side shows discovery of a specific antibiotic and right side points when the resistance was detected. Adapted from [16].

As depicted in Figure 1.1 is possible to observe a discovery void of novel antibiotics. This impaired pipeline of development has different causes, the most pertinent being the lack of incentive for pharmaceutical companies over economic obstacles [17]. The fact that these drugs present themselves as fast acting, limits the patients need to a short period of usage, which as consequence brings a low return on the investments made.

Thereby, the usage of novel antibiotics becomes reserved and their longtime efficiency becomes unpredictable as resistance evolves [18].

The development of resistant strains by the use of antibiotics is potentialized when its therapeutic usage is not done correctly, and patients fail to take their full course of prescribed antibiotic treatment. With that, the microbe responsible for the infection in question is put in a stress condition that is not enough to promotes its death but serves the purpose of applying selective pressure favoring antibiotics resistance [19]. Another way for the emergence of drug resistance is the over usage of those substance in agriculture, since antibiotics used in this area are the same or very similar to the ones prescribed for clinical treatment [20]. Recent evidence suggests that poultry or pork might be a possible source of quinolone-resistant *Escherichia coli* in the rural villages of Barcelona, where one fourth of children were found to be fecal carriers of these organisms, despite never having been exposed to quinolones [21].

Another problem regarding resistant bacteria is the fact that they may collect multiple resistance traits over time and can become resistant to multiple classes of antibiotics [22]. Moreover the fact that a single antibiotic can help to select resistance against other structurally related compounds of the same class, is a clear evidence of the problem being faced. Table 1.1 shows some of the common mechanisms for drug resistance.

Table 1.1: Examples of resistance modes of different classes of antibiotics. Adapted from [7].

Antibiotic class	Examples	Resistance mode
P-Lactams	Penicillins, Cephalosporins, Penems, Monobactams	Hydrolysis, efflux, altered target
Aminoglycosides	Gentamicin, Streptomycin, Spectinomycin	Phosphorylation, acetylation, nucleotidylation, efflux, altered target
Glycopeptides	Vancomycin, Teicoplanin	Reprogramming peptidoglycan biosynthesis
Tetracyclines	Minocycline, Tigecycline	Monooxygenation, efflux, altered target
Macrolides	Erythromycin, azithromycin	Hydrolysis, glycosylation, phosphorylation, efflux, altered target
Lincosamides	Clindamycin	Nucleotidylation, efflux, altered target
Streptogramins	Synercid	Carbon-Oxygen lyase, acetylation, efflux, altered target
Oxazolidinones	Linezolid	Efflux, altered target
Phenicols	Chloramphenicol	Acetylation, efflux, altered target
Quinolones	Ciprofloxacin	Acetylation, efflux, altered target
Pyrimidines	Trimethoprim	Efflux, altered target
Sulfonamides	Sulfamethoxazole	Efflux, altered target
Rifamycins	Rifampin	ADP-ribosylation, efflux, altered target
Lipopeptides	Daptomycin	Altered target
Cationic peptides	Colistin	Altered target, efflux

The lack of a global management guideline for daily antibiotics usage practices is also another point that has been contributing to the emergence of resistance on a global scale [7]. While some countries have acted to provide guidance for those practices, most still haven’t taken any action toward interventions [7].

The consequence of antibiotic resistance has already shown its impacts around the world. The World Economic Forum has identified antibiotic resistance as a global risk beyond the capacity of any organization or nation to manage or mitigate alone [23]. In developed economies, the impact of this issue is reflected in the higher healthcare costs and decreases in labor supply, productivity, household incomes, and national income and tax revenues [24]. The Europe Union has reported that, annually, around 25000 deaths are due to a subset of drug resistant bacteria, with the extra health care costs and lost productivity due to antimicrobial resistance amounting to at least 1500€ million. Similar impacts should also be present in low- and middle-income countries [24].

1.2 Alternatives for antibiotics

From the rising challenge of fighting the insurgence of antibiotics resistant microbes, it became necessary to develop new alternatives different from the traditional ones being used until current days [25]. Host defense peptides (HDPs) are defined as a class of innate immunity components expressed by multi-cellular organisms [26]. As far as it is known, one part of their functions is to kill invasive cells without damage to the host and without presenting themselves as a stress agent for the development of resistance traits [26]. This is due to their mechanism of action, which is thought to involve membrane permeabilization [26]. Since this is not a ”lock and key” type of mechanism, the pathway to membrane disruption is not as straight forward and thus more demanding for the microbe to bypass [26].

Since the discovery of HDPs, thousands of those substances have been encountered and catalogued in an online antimicrobial peptide (AMP) database curated by Wang and Wang, containing, to date, more than 3200 entries from six different kingdoms [22, 27, 28]. Among those substances, different amino acids sequencing and secondary structures are presented, and physiochemical properties seems to be the common factor in respect to their antimicrobial effectiveness [26]. The presence of a cationic net charge at neutral pH, coupled with a significant fraction of hydrophobic residues and relative short chain size are frequent attributes for this class of compounds (Fig. 1.2). Of these three main attributes, the hydrophobicity of the molecule is integral for their interaction with phospholipids (PLs) bilayers [29], and the presence of positive net charge is central for their electrostatic attraction to anionic components of the bacterial cell surface [30].

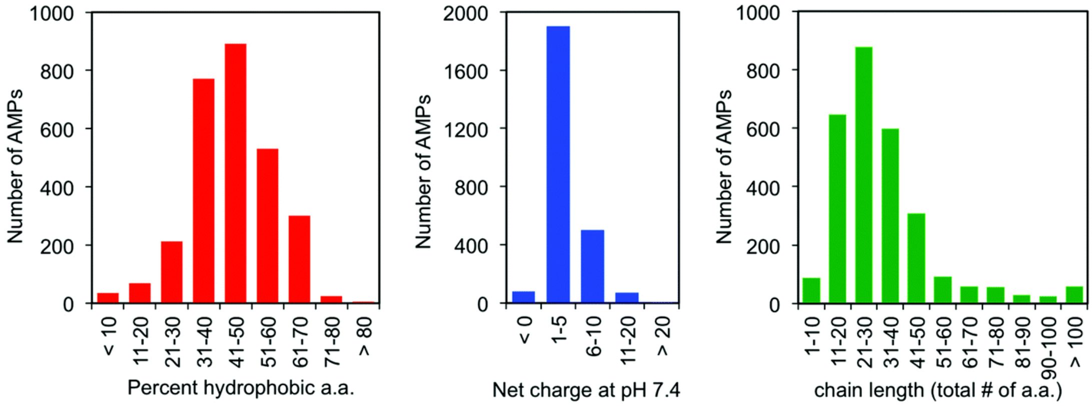

Figure 1.2: Distribution of AMPs entries in respect to percentage of hydrophobic amino acids, net charge and chain size, respectively. Adapted from [26]

While HDPs were being discovered, the field of disinfectant polymers begun its development [31]. It started with the introduction of benzalkonium chlorides (BAC) polymer (a benzyl quaternary ammonium as a side chain of a long alkyl chain) and styrene derivatives containing BAC [32] and in the late 90s developed to the creation of polymers that mimics HDPs, such as β-peptides [29, 33], α/β-peptides [34] and peptoids [35].

Although HDPs are excellent potential substitutes for antibiotics, due to their antimicrobial and non-toxic characteristics, the bioprocesses involved in the manufacture of cheap and scalable volumes are still not developed enough [28]. At the same time, while chemical processes are well known and developed for production in large scale, the potential toxicity of these compounds is something that cannot be neglected [28]. With these points, in the early 2000s, the fields of HDPs and biocidal polymers started to merge seeking the development of HDP mimetic polymers (Fig. 1.3). The rationale behind this merge is to combine the advantages of peptide activity with the cost effectiveness and scalability of synthetic polymer chemistry, without the need for precise sequence, uni-molecular chain length, or defined secondary structure. [26].

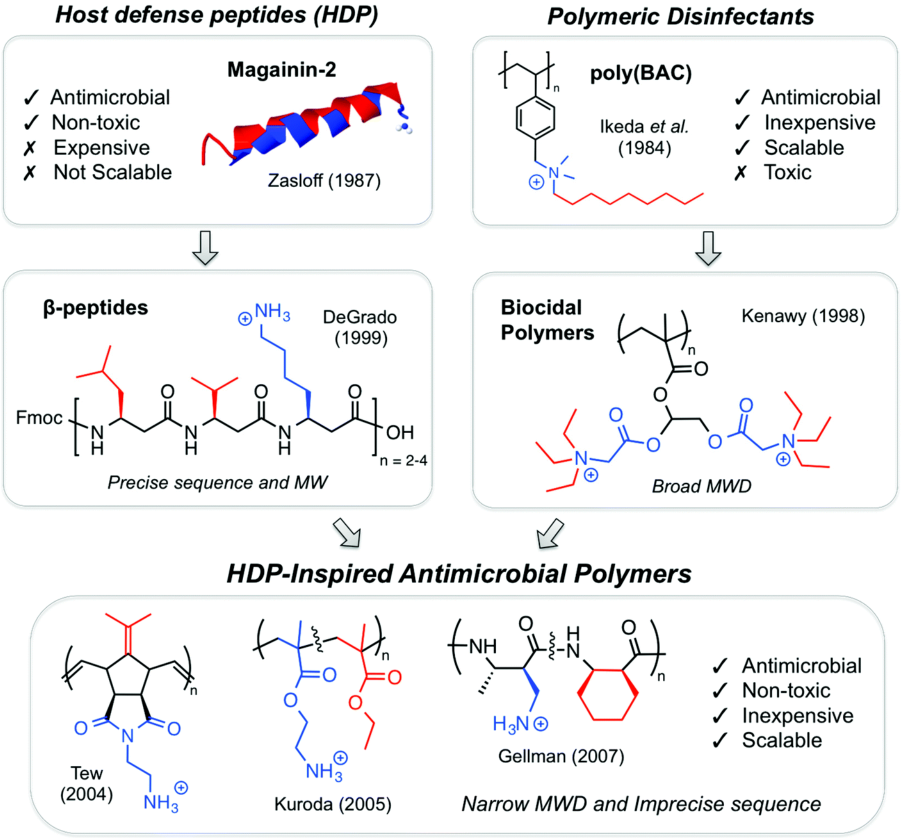
Host defense peptides (HDP)
Polymeric Disinfectants
Magainin-2
✓ Antimicrobial
✓ Non-toxic
✗ Expensive
✗ Not Scalable
Zasloff (1987)
poly(BAC)
Ikeda et al. (1984)
✓ Antimicrobial
✓ Inexpensive
✓ Scalable
✗ Toxic
β-peptides
DeGrado (1999)
Fmoc
OH
n = 2-4
Precise sequence and MW
Biocidal Polymers
Kenawy (1998)
Broad MWD
HDP-Inspired Antimicrobial Polymers
Tew (2004)
Kuroda (2005)
Gellman (2007)
✓ Antimicrobial
✓ Non-toxic
✓ Inexpensive
✓ Scalable
Narrow MWD and Imprecise sequence

Figure 1.3: Evolution of antimicrobial polymers. The main difference between HDP and polymeric disinfectants are highlighted in the first two boxes. Evolution of both fields lead to the development of HDP-inspired antimicrobial polymers. Adapted from [26]

1.2.1 Bio-mimetic polymers

The relationship between the structure and activity of the HDP-mimetic polymers lays upon two fundamental design principles: 1) the hydrophobic/hydrophilic component ratio; and 2) the presence of a structured cationic group [18]. In 2009, Kuroda, Caputo, and DeGrado [36] showed that a poly(methacrylate) random copolymer with 40% methyl side chains (hydrophobic group) and 60% aminoethyl side chains (hydrophilic and charge group) is at the same time a potent antibacterial compound and has minimum hemolytic activity. They also reported that a fully cationic homopolymer shows no effect against *E. coli*, while fully hydrophobic homopolymers have high hemolytic activity and poor solubility. The study reported that excess of hydrophobicity has the potential to generate polymers with high toxicity and poor solubility whereas polycation polymers with very low hydrophobicity were not potent antibacterial candidates and also show the tendency to aggregate red blood cells (RBCs). Similar results were obtained when amphiphilic balance was optimized with poly(norbornene) [37] and nylon-3 copolymers [38, 39].

While the amphiphilic balance of the polymer dictates, mostly, cell type selectivity of the compound, the cationic net charge of the polymer will dictate the electrostatic attraction to the bacterial cell surface. That happens because positive net charge will have a stronger interaction with the negatively charged PL headgroups of the lipid bilayers [40]. For example, HDPs are normally rich in Lysine and/or Arginine. Both amino acids contain amine groups (Fig. 1.4), which, at physiological pH, have cationic charge [41].

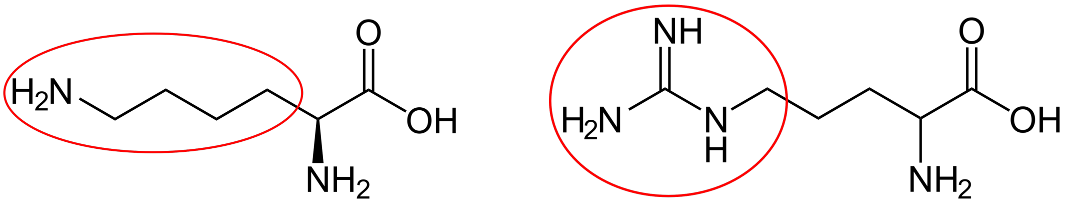

Figure 1.4: Butylamine and guanidine groups from Lysine (left) and Arginine (right) amino acids.

The difference from building a polymer possessing primary amine groups instead of the traditional quaternary ammonium salt (QAS) was investigated by Palermo and Kuroda in 2009 [42]. For the same polymer type, the one with primary amine groups outperformed the ones with tertiary or quaternary in terms of antimicrobial activity and toxicity. Following this study, the role of cationic functionality was investigated and it was observed that primary ammonium groups can form a stronger complex with PL headgroups when compared to QAS analogues [40]. Also, the effect of the density of amine groups was investigated, with Al-Badri et al. [43] showing that the increase at amine density in each monomer unit enhances the efficacy of the polymers by highly decreasing its hemolytic toxicity.

On the other hand, the functionality of guanidinium can be explained by its ability to complex anionic PLs by a combination of Coulombic attraction and precisely orientated bidentate hydrogen bonding interactions. This led to the development, by several groups, of cationic amphiphilic polymers containing the guanidinium functional group as the source of cationic charge, instead of primary ammonium cations [26]. Polymethacrylates with guanidinium cations were more active against *S. epidermidis* and *C. albicans* relative to primary ammonium containing analogues [44], with similar results being presented for guanidinium functionalized poly(methacrylamide)s [45].

1.2.2 Poly(ethylenimine)

By understanding the design principles that will provide the desired antimicrobial activity, characteristic of HDP mimetic polymers, one can propose structural modifications that allow increased efficiency and a straightforward synthesis. As one of the many polymers present in the market, poly(ethylenimine) (PEI) has been shown to be a potent alternative to combat antibiotic resistant organism, due to its intrinsic features.

PEI is a synthetic, non-biodegradable, cationic polymer that can contain primary, secondary and/or tertiary amino functional groups. It is found in both branched and linear forms (Fig. 1.5) and can be synthesized by acid catalyzed polymerization of aziridine and ring opening polymerization of 2-ethyl-2-oxazoline followed by hydrolysis, respectively [46, 47]. Due to the abundance of reactive amino groups, PEI can be modified to display the necessary hydrophobicity and positive charge densities that are primary requirements for antimicrobial activity [48]. Also, the ammonium groups of PEI, which are cationic, coupled with the ethylene spacer of its structure, which serves as hydrophobic moiety, create a repeating cationic amphiphilic motif along the polymer backbone at neutral pH without any further chemical modification by hydrophobic groups [25].

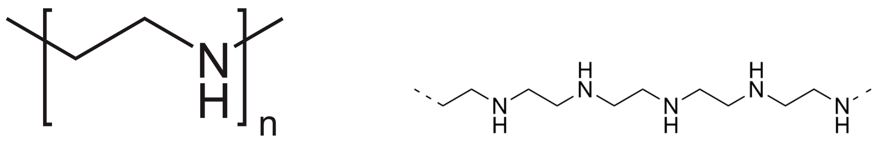

(a) Ethylene imine monomer.

(b) Fragment of linear PEI chain.

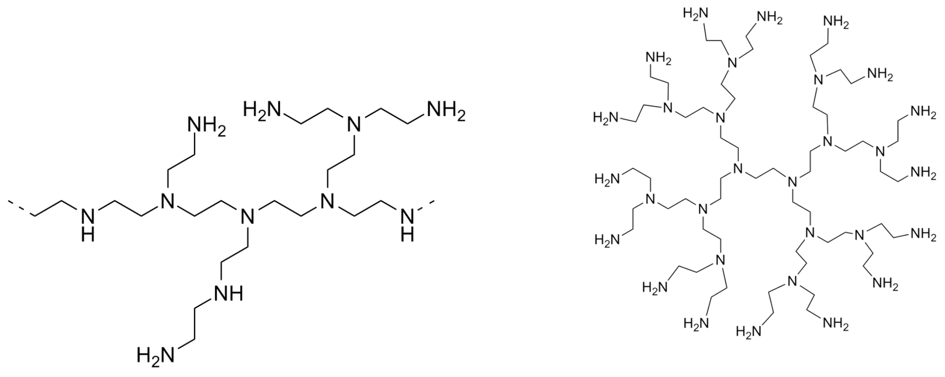

(c) Fragment of branched PEI chain.

(d) PEI dendrimer of second-generation.

Figure 1.5: a) Ethylene imine monomer, b) linear PEI fragment, c) Branched PEI fragment and d) Second-generation PEI dendrimer.

In 1997, Helander et al. [49] investigated the effect of the polycation PEI on the permeability effects on Gram-negative bacterial outer membrane using *E. coli*, *P. aeruginosa* and *S. typhimurium* as target organisms. The results showed that in concentrations inferior to 20 μg/ml, PEI increased the bacterial hydrophobic permeation of the outer membrane. It showed an increase in the susceptibility of the tested species to the hydrophobic antibiotics Clindamycin, Erythromycin, Fucidin, Novobiocin and Rifampicin. Without being directly bactericidal, polycation PEI was been shown to be in fact a potent permeabilizer of the outer membrane of Gram-negative bacteria.

Lin et al. [48] assessed if PEI could be used as functionalized antimicrobial coating material in glass and plastic slides. Their study pointed that alkylated PEIs attached to flat macroscopic surfaces and/or to nanoparticles make these materials highly bactericidal toward both Gram-positive and Gram-negative pathogenic bacteria [48]. These systematic chemical modifications of the immobilized PEI shed some light on the relationship between the structure of the polymer and the antibacterial efficiency of the resulting coating. Later, *N*-hexyl-*N*-methyl-poly(ethylenimine) covalently bound to amino glass slides resulted in almost 100% inactivation of both water borne and airborne bacteria, and fungi, including pathogenic and antibiotic-resistant strains without any report of emergence of resistance while being nontoxic to mammalian cells (COS-7, African green monkey) [50]. In addition, several studies have investigated the antibacterial activity of water-soluble PEI derivatives containing quaternary ammonium salt groups with long alkyl or aromatic groups and applications for water-insoluble hydrophobic PEIs including nanoparticles and antibacterial coatings, as promising materials for coating of medical devices [25].

Although the properties of PEI derivatives have been extensively studied and presented as good alternative antimicrobials, conventional unmodified PEI also possesses antimicrobial activity and low cytotoxicity. In 2012, Gibney et al. [25] investigated a series of branched and linear PEIs (b-PEI and l-PEI, respectively) with relatively low molecular weight to understand the effect of molecule's architecture and size on antibacterial activity. The activity was tested against *E. coli* and *S. aureus* and results showed that it is intrinsically dependent on both parameters. The membrane permeabilization assays performed indicate that PEI may exert their antibacterial activity by mechanisms other than membrane disruption [25]. The polymer is also selective to bacteria over RBCs, and cytotoxic assays indicate that b-PEI is less toxic to human Hep-2 cells than their linear counterparts, although still significantly reduced cell viability after a 24h exposure. The study results can help refine the design of this polymers towards optimal activity and cell selectivity. Most recently, Venkatesh et al. [51] investigated the antimicrobial and cytotoxic properties of cationic polymers with peptide/isopeptide and polyethylene/PEI backbones. The study was conducted with different strains of *S. aureus, P. aeruginosa* and *C. albicans* and biocompatibility for primary human dermal fibroblasts. The results showed that l-PEI displayed superior antimicrobial activity against bacterial pathogens over poly(allylamine), with and cytotoxicity only at concentrations above 500 μg/ml.

PEI and other synthetic analogs, are easy to produce and low-cost polymer, and well established methods enables the tuning of chemical and physical properties via simple structural modifications. These features facilitate further development and turn them attractive alternatives as novel antibacterial agents [25].

1.3 Molecular Dynamics

By having the possibility to change and tune synthetic polymers to present the desired functionality, a huge variety of options can be manufactured. These possibilities demonstrate the wide range of potential novel therapeutic polymer that can be developed. However, creating and testing each one of these alternatives presents itself as a challenge. It is necessary to have a guide that allows the understanding of the direction taken prior initiating costly and time-consuming experimental works *in vitro*.

In recent years, computational experiments have become crucial for the progress of science. The rise of high-performance computing has enabled experimentation *in silico* as a powerful tool that bridges the gap between theory and laboratory experiments [52]. Taking into consideration that bio-mimetic antimicrobial polymers demonstrate to have some type of interaction with microbial membranes, it is important to have a tool that shows if the molecule being tested presents promising interactions and effects. With that, Molecular

Dynamics (MD) appears as an important computational tool for understanding the physical basis of structure, dynamic evolution of systems, and the function of biological macro-molecules [53] and is a tool that aids the development of new drugs.

Molecular Dynamics is based on Newtonian physical models governing inter-atomic interactions, to predict how every atom in a molecular system moves over time [53]. These simulations can capture a wide variety of important biomolecular processes, describing the positions of every atom with femtosecond temporal resolution. MD has its origin in the late 1950s, with the simulations of simple gases by Alder and Wainwright [54] and was first used to simulate protein in the late 1970s, by Salomon-Ferrer et al. [55]. It is important to remark the groundwork performed by Martin Karplus, Michael Levitt and Arieh Warshel that enabled these simulations, for which they were awarded the 2013 Nobel Prize in Chemistry [54]. MD simulations have, however, become substantially more popular and visible in recent years, particularly from the perspective of experimental molecular biologists. Simulations have begun to appear frequently in experimental structural biology papers, where they are used both to interpret experimental results and to guide experimental work (Fig. 1.6) [56].

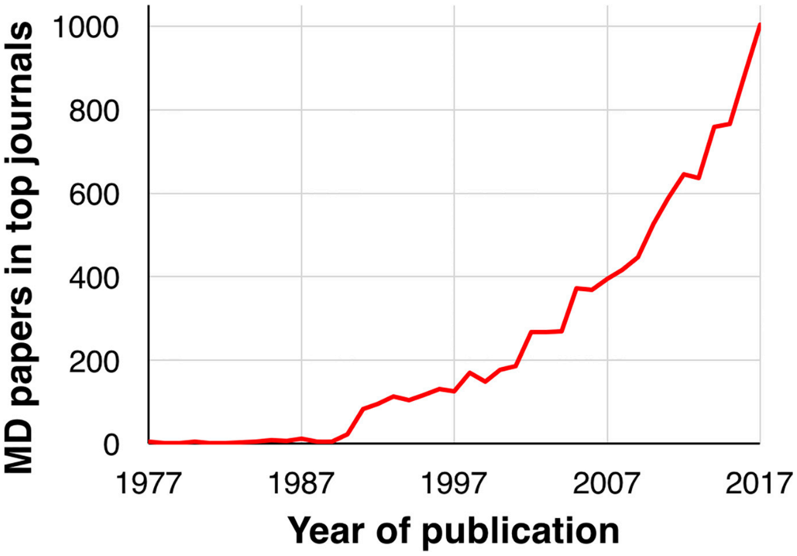

Figure 1.6: Evolution of MD publications related to Structural Biology. Adapted from [56].

The increase in use of MD simulations is possible, mainly, due to two under-laying drivers. First, the advance of techniques, such as crystallography and cryogenic electron microscopy, allows for a much better resolution of structures, providing a better starting point for MD simulations [56]. Second, the evolution of computing power and MD simulations themselves, make possible to run MD simulations outside supercomputers [56]. That can be exemplified by the introduction of graphics processing units, that allows powerful simulations to be run locally and at a modest cost [55, 57], the evolution of software packages, that became easier, more user-friendly and with better user support and also by the constant work done in improving the accuracy of the physicals models behind the simulations [56].

To calculate how a given system will evolve over time, MD uses Newton's equations of motion to determine the net force and acceleration experienced by each atom in the system (all-atom MD — AA MD) and with that simulates the time evolution of each atom considering the interactions generated by each net force from each time step [52]. To apply the motion's equation, each atom i is treated as a single point and must have an associated position r_i, mass m_i and fixed charge q_i. The relationship between the force on each one of the system's atoms and its acceleration is described by Newton's second law of motion where F_i is the force exerted on the mass and a_i is the respective acceleration (eq. 1.1):

$$F_i = m_i a_i \tag{1.1}$$

This force can also be interpreted as a gradient of the potential energy of the system, V, as the acceleration is taken as the second derivative in time of the position, so (eq. 1.2):

$$-\nabla_i V = m_i \frac{d^2 r_i(t)}{dt^2} \tag{1.2}$$

The time step used in MD calculations is approximately one order of magnitude smaller than the fastest motion - hydrogen molecule's bond vibration - which oscillates roughly about every 10 fs. The MD simulation will follow the algorithm describe in Figure 1.7 until desired conditions are achieved:

Since the starting point of any MD simulations requires the potential energy of the system, it is crucial to have it well defined. The potential is defined in terms of a force field (FF); that describe the different particle interactions that may happen during simulation. It can be divided into interactions between atoms chemically bonded and into interactions between atoms that are non-bonded. A general description of the potential energy of a system modeled by a FF can be seen in the Figure 1.8:

The determination of the parameters for a specific FF is done taking into account physiochemical experiments and/or electronic structure calculations, using quantum mechanics (QM) methods (e.g., ab initio molecular orbital or density functional theory calculations) [52]. QM methods, in a simple way, perform nuclear and/or electronic interactions between particles by solving the time independent Schrödinger's equation and its approximated forms (e.g., Born-Oppenheimer) [59]. A set of parameters should be defined for different types of atoms and for each one of the potentials that define a FF. This means that a FF will have discrete parameters for an oxygen atom in a carbonyl functional group and in a hydroxyl group [52]. An example of FF parameter set is: atomic masses, van der Waals radii, partial charges for individual atoms, equilibrium values of bond lengths, bond angles, dihedral angles and values corresponding to the effective spring constants for each potential. Some popular FFs used in classical MD atomistic simulations are Amber, CHARMM, and GROMOS [52].

THE GLOBAL MD ALGORITHM

---

1. Input initial conditions

Potential interaction V as a function of atom positions
Positions $\boldsymbol{r}$ of all atoms in the system
Velocities $\boldsymbol{v}$ of all atoms in the system
$\Downarrow$

---

repeat 2,3,4 for the required number of steps:

---

2. Compute forces

The force on any atom

$$\boldsymbol{F}_i = -\frac{\partial V}{\partial \boldsymbol{r}_i}$$

is computed by calculating the force between non-bonded atom pairs:

$$\boldsymbol{F}_i = \sum_j \boldsymbol{F}_{ij}$$

plus the forces due to bonded interactions (which may depend on 1, 2, 3, or 4 atoms), plus restraining and/or external forces.
The potential and kinetic energies and the pressure tensor may be computed.
$\Downarrow$

3. Update configuration

The movement of the atoms is simulated by numerically solving Newton's equations of motion

$$\frac{\mathrm{d}^2\boldsymbol{r}_i}{\mathrm{d}t^2} = \frac{\boldsymbol{F}_i}{m_i}$$

or

$$\frac{\mathrm{d}\boldsymbol{r}_i}{\mathrm{d}t} = \boldsymbol{v}_i ; \quad \frac{\mathrm{d}\boldsymbol{v}_i}{\mathrm{d}t} = \frac{\boldsymbol{F}_i}{m_i}$$

$\Downarrow$

4. if required: **Output step**
write positions, velocities, energies, temperature, pressure, etc.

Figure 1.7: Global MD Algorithm. The sequence of steps consist in: 1) input of initial conditions (potential interactions, positions and velocities); 2) computation of forces from bonded and non-bonded interactions between atoms; 3) derivation of new positions and velocities for each atom; 4) storing of desired output. Adapted from [58].

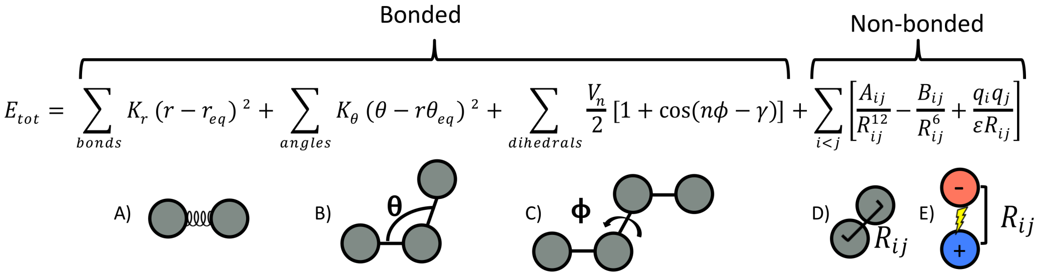

$$E_{tot} = \overbrace{\sum_{bonds} K_r\,(r - r_{eq})^2 + \sum_{angles} K_\theta\,(\theta - r\theta_{eq})^2 + \sum_{dihedrals} \frac{V_n}{2}[1 + \cos(n\phi - \gamma)]}^{\text{Bonded}} + \overbrace{\sum_{i<j}\left[\frac{A_{ij}}{R_{ij}^{12}} - \frac{B_{ij}}{R_{ij}^{6}} + \frac{q_i q_j}{\varepsilon R_{ij}}\right]}^{\text{Non-bonded}}$$

Figure 1.8: Example of a FF model. The potential energy will be the sum of the energies related to: A) stretching or compressing of bonded pair of atoms (modeled by a simple spring), B) Increasing or decreasing bond angle formed between three consecutive atoms (modeled by a simple harmonic), C) dihedral angle rotations defined by four consecutive atoms (also modeled by a simple harmonic), D) van der Waals interactions (modeled by Lennard–Jones potential) and E) Electrostatic interactions (modeled by Coulomb's law). The interactions from A) to C) represent the ones from chemically bonded atoms, while D) and E) are the ones from non-bonded atoms. Adapted from [52]

1.3.1 Coarse-grained models

Despite the advantages of MD simulations, large systems and longtime scales - beyond the 10^1 nm size and the μs timescale - are still computationally demanding for atomistic systems. This is because atomistic MD simulations generate force calculations for each time step of the process, which by itself already requires considerable computation effort, and those calculations must be repeated several times for each atom of the system [52]. However, since some biological processes such as protein folding, aggregation and biological assembly occur at longer time scales, it became necessary the use of a different approach than AA MD [60].

One of the alternatives used to circumvent the limitations of AA MD is the use of coarse-grained (CG) models. These models present a platform to bridge the gap between AA based simulation studies and the macroscopic behavior of biological mechanisms [60], being well suited to study large scale biological complexes, since they can probe the time and size scales of systems beyond what is feasible with AA models [59].

The idea behind CG models is to make a reduced representation of the AA model of the system of interest without losing the main molecular characteristics that dictate its behavior [60], by representing groups of atoms as a single CG pseudo atom. From this reduced version comes faster computation sampling due to the decrease in the degrees of freedom and with that the possibility to run simulations for a longer period of time [60]. Additionally, bonded interactions tend to have much lower force constants — hence, longer periods of motion — allowing for the use of significantly larger MD timesteps.

To develop a CG models it is necessary to define the pseudo atoms that will represent the group of multiple atoms; derive the energy function (potential energy of the system) which defines the interaction between those pseudo atoms and also define the dynamical equations to study the time-based evolution of the CG system [60]. That can be done considering structural information of the system (obtained experimentally) or through the derivation of statistical data acquired from AA MD simulations [61].

The most popular CG model in use is the Martini force field, being first proposed for lipids and later extended for protein, carbohydrates and other type of systems [59]. The Martini force field is parameterized in a systematic way, combining top-down and bottom-up strategies, where non-bonded interactions are based on the reproduction of experimental partitioning free energies between polar and apolar phases of a large number of chemical compounds and bonded interactions are derived from reference AA MD simulations [59]. The model uses a four-to-one mapping (Fig. 1.9), meaning that every four heavy atoms group (and its associated hydrogens) are replaced by a unique single interaction center, also called “bead”. In order to keep the model simple, only four main types of interaction sites are defined: polar, non-polar, apolar, and charged. Each bead type has a number of subtypes (for a total of 18 types), which allow for an accurate representation of the chemical nature of the underlying atomistic structure [59].

Some of the recent works done involving the use of Martini in the protein field are the study of protein ligand binding processes (2014) [63], mechanisms of allostery (2015) [64], predicting the binding mode of peptides

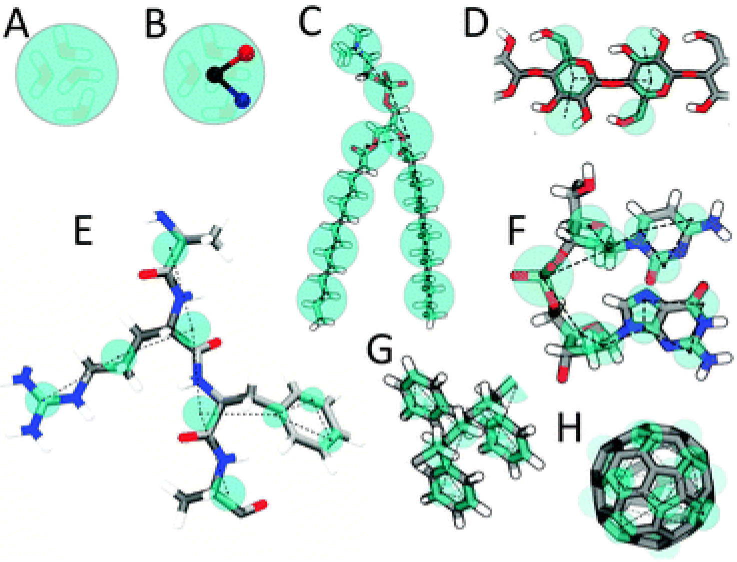

Figure 1.9: Martini mapping examples of selected molecules: (A) Standard water particle representing four water molecules, (B) Polarizable water molecule with embedded charges, (C) DMPC lipid, (D) Polysaccharide fragment, (E) Peptide, (F) DNA fragment, (G) Polystyrene fragment, (H) Fullerene molecule. In all cases Martini CG beads are shown as cyan transparent beads overlaying the atomistic structure. Taken from [62]

to G-Protein coupled receptors (2017) [65] and determining the role of hydrophilicity and hydrophobicity in the self-assembly of (AF) 6H5K15 peptide derivatives (2014) [66].

Due to the complex nature of the structural dynamics of biological macromolecules and their working mechanism, that range from atomic to molecular level, the use of multiscale simulations has emerged as an important approach. This consists in the integration of CG models within AA ones to define different components of the system which allows for an in depth understanding of the macromolecular dynamics with an insight on the atomic picture [60]. The study of rotary motor proteins through free energy landscapes and CG based simulation is a good example of multiscale simulations [67].

CG force fields a powerful alternative to AA ones, but also have their own set of limitations. First, they represent a simplified version of the system under investigation, which, by elimination of atomic details, may impact the determination of precise properties under study [60]. They are also sometimes tailored for specific features of systems or phenomena of interest, so it is harder to transfer properties between varied systems. As an example, the Martini FF is based upon the calibration of non-bonded interactions against the oil/water partitioning coefficients [59], which happens to be highly correlated with membrane–peptide binding and protein–protein recognition. Consequently, the Martini model has found dominant applications in studying the membrane protein systems and their interaction with lipids, while others CG force fields will be better suited to predict other types of systems and interactions [59].

The increase modeling demand of new and challenging systems, coupled with reported insufficiencies in the representation of some biomolecular interactions, led to a recent ongoing improvement effort of the Martini FF. A beta version of the upcoming version 3 of Martini has been released and some of the new features of the new version consist in: new specific parameterization of beads corresponding to two-to-one or three-to-one mappings; improvements in the interaction matrix between the multiple possible types of particles, including more interaction levels and reformulation of charged beads.[68]

1.4 Objectives

This project's main goal was to apply computational tools to power the development of bio-mimetic antimicrobial nanoparticles. This was done by exploring and trying to gain insights on the killing mechanism of an already existing nanoparticle by means of MD simulations. For this, it was necessary to develop and build the corresponding CG model of the nanoparticle being investigated and run simulations against CG membrane models that can capture the difference between bacteria and mammalian PL membranes. The results from theses simulations enabled the proposal of modifications to synthesize novel nanoparticles with the desired functionality and biophysical properties. These novel compounds were tested *in silico*, against those same PL membrane models. All the results helped to point the necessary characteristic that must be involved in enhanced design of antimicrobial nanoparticles, and how to improve the synergy among them. The used methodology, as well as the order of the work done, is described below:

i The studied nanoparticle - PURE$_{G4}$-OEI$_{48}$ - is a fourth-generation polyurea dendrimer (PURE$_{G4}$) core with 48 linear oligo(ethylenimine) chains (OEI$_{48}$) connected to its surface [69];

ii The development of the suitable CG topology for this nanoparticle was splitted into two parts:

  (a) Development the Martini 3 topology for linear OEI. This was done through QM and atomistic MD simulations that will be used to derive the necessary set of parameters for the Martini 3 force field model. The validation of the model built in Martini 3 was carried by comparing some of its properties (e.g. end-to-end distance and radius of gyration) against the ones from atomistic topology and also from data in the literature.

  (b) Develop the Martini 3 topology for the polyurea dendrimer. This was done in a similar fashion to what was done for OEI, but in this case an already existing atomistic topology will serve as a starting point for the parameters' derivation. Again, the validation of the topology was done by the comparison of properties between atomistic and CG models.

iii To simulate the difference between mammalian and bacterial membrane bilayer, two different models was used. The first one is composed of anionic 1-palmitoyl-2-oleoyl-sn-glycero-3-phosphocholine (POPC) while the second has a composition of POPC/1-Palmitoyl-2-oleoyl-sn-glycero-3-(phospho-rac-(1-glycerol)) (POPG) at a 1:3 ratio [70].

The results from the simulation of the nanoparticle against both membrane models were analyzed, and the results helped understand the killing mechanism of the nanoparticle. From the acquired insight we aimed to propose specific modifications to improve selectivity and toxicity. These novel molecules model were also tested *in silico*.

CHAPTER 2 - METHODS

2.1 Poly(ethylenimine) parameterization within the Amber and Martini FF

Although there are already parameters for CHARMM FF and a Martini model for PEI in the semi- and non-protonated states [71], the lack of parameters for the fully-protonated form along with the objective of using the new Martini 3 version of this CG FF justify the work to create a full set of parameters for the Amber FF, until now absent. Also, the building process of the CG model for PEI will take into consideration numerical stability enough to allow running simulation with the standard Martini time step of 20 fs, which does not happen for the previously mentioned model [71].

The CG parameters of this model will follow the recommended strategy to assign the bead type for each building block of the polymer by chemical similarity to already-parameterized models; bonded parameters will be taken from Amber AA reference data, generated using amber99sb-ildn [72]. Since the chosen AA FF does not have specific parameters for partial charges and torsions involving protonated secondary amines, those were derived using a comprehensive body of *ab initio* calculations.

The term Amber is used to refer to the family of empirical force fields implemented by a collective of suite programs that allow users to carry out molecular dynamics simulations, particularly on biomolecules [73]. The simplest implementation form of this family of FF is described by the Hamiltonian equation below:

$$\begin{aligned} E_{total} = \sum_{bonds} k_b(r-r_0)^2 \\ + \sum_{angles} k_\theta(\theta-\theta_0)^2 \\ + \sum_{dihedrals} V_n[1+cos(n\phi-\gamma)] \\ + \sum_{i=1}^{N-1}\sum_{j=i+1}^{N}[\frac{A_{ij}}{R_{ij}^{12}} - \frac{B_{ij}}{R_{ij}^{6}} + \frac{q_i q_j}{\epsilon R_{ij}}] \end{aligned} \tag{2.1}$$

where

$$A = \epsilon R_{min}^{12} \quad and \quad B = 2\epsilon R_{min}^{6} \tag{2.2}$$

The first three lines of equation 2.1 correspond, respectively, to the harmonic term for bond stretching (where k_b is the force constant and r_0 is the equilibrium distance), the harmonic angle bending terms (force constant k_θ and an equilibrium angle of θ_0) and the Fourier-series expansion for torsional terms (torsion barrier term V_n, the angle phase γ and periodicity n). The last term of the equation encompasses the non-bonded interactions: the standard formulation of the 6-12 Lennard-Jones (LJ) potential and the electrostatic interaction, where ϵ is the depth of the potential well for the interaction of atoms i and j, R_{ij} is the distance separating atoms i and j, R_{min} is the sum of the van der Waals radii and q_i and q_j are the atomic partial charges.

In a bottom-up approach to develop an AA description of PEI, we resorted to QM calculations to derive the necessary parameters of the molecular mechanics (MM) FF. To build PEI Amber models for different protonation states we perform the adjustment of the AA FF relative to QM data for three minimal PEI tetramers. Tetrameric length was chosen to include characteristic central repetition units, less influenced by terminal behavior, while keeping an acceptable computational QM cost. Figure 2.1 demonstrates the structure of each one of the models. PEI with all nitrogen atoms protonated will be referred to as *pei+* (Fig. 2.1 a)), semi-protonated PEI, with protonation of alternating nitrogens (Fig. 2.1 b)) as *peis*, and non-protonated PEI as *pein* (Fig. 2.1 c)).

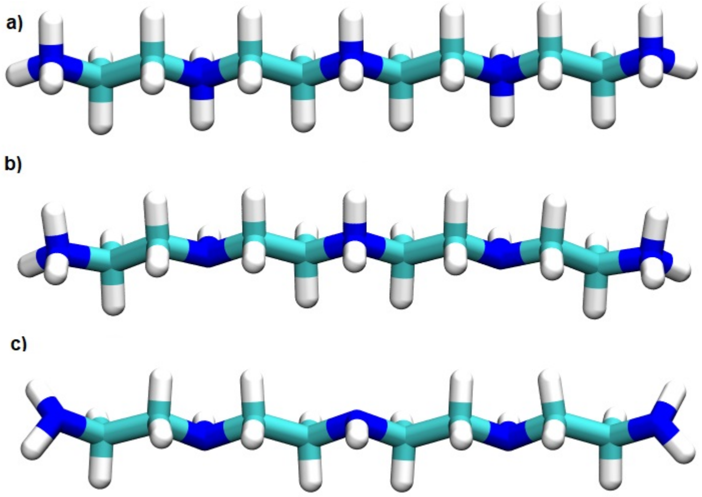

Figure 2.1: PEI models used in the parameterization of the Amber FF. Dark blue represents nitrogen atoms, cyan represents carbons and white represents hydrogens. a) fully-protonated tetramer b) semi-protonated tetramer and c) non-protonated tetramer.

Taking into account the further parameterization of Martini 3 model, all the tetramers above can be described by five different types of residues:

- **PEIQ** – protonated polymer monomer ($CH_2{-}NH_2^+{-}CH_2$);
- **PEI** – non-protonated polymer monomer ($CH_2{-}NH{-}CH_2$);
- **TPEIQ** – protonated terminal residue for *pei+* ($NH_3^+{-}CH_2{-}CH_2{-}NH_2^+{-}CH_2$);
- **TPEIS** – protonated terminal residue for *peis* ($NH_3^+{-}CH_2{-}CH_2{-}NH{-}CH_2$);
- **TPEI** – terminal residue for *pein* ($NH_2{-}CH_2{-}CH_2{-}NH{-}CH_2$)

The choice of these residue divisions takes into consideration a symmetry around the N atom of each residue (excluding terminals) and of the overall molecule, which simplifies further work with the Martini FF. Terminal residues encompass 1.5 units each, that we consider to not have central behavior.

The first step in the development of an Amber PEI model is to derive the partial atomic charges that each atom will have. The Amber force field is built around the concept of accurate pair-wise charges, with constraints typically imposing integer charges to the entirety of a residue (or a monomer unit). In Amber, the method used for point-charge calculation is the Restrained Electrostatic Potential (RESP) method [74]. It is employed on a QM geometry-optimized structure of the molecule of interest, for which the spatial distribution of the electrostatic potential (ESP) has also been computed. RESP collapses this potential into single point charges by optimizing atomic charge assignment while restraining the resulting ESP to that computed by QM. QM geometry optimizations were done at Hartree-Fock (HF) level of theory with a 6-31G(d) basis set. Final electronic probabilities were computed on the optimized structure, using Møller–Plesset perturbation of second order (MP2) theory and a 6-31+G(d,p) basis set. All QM calculation were performed using the Gaussian 09 program.

With the partial charges derived (better explained in the subsection 2.1.1), torsions were probed by geometry-optimizing molecular structures at both MM and QM levels while restraining or constraining the torsion of interest to a range of values. Dihedral torsion potentials were obtained by linearly decomposing the difference between the resulting MM and QM potential energies into combinations of cosinusoids of different periods.

The optimization procedure for the dihedrals consist in a scan of torsion coordinates with the objective of minimizing the torsion dihedral potential energy difference between QM and MM by fitting the force constant, phase and multiplicity of the dihedral potential function (eq. 2.1). Both dihedrals of interest for each tetramer were rotated a full 360° in steps of 5°. For each angle the configuration with the minimum energy between all possible arrangement of H atoms was chosen as the input for the QM calculation.

2.1.1 Optimization of partial atomic charges of PEI tetramers

The charge fitting procedure for all the tetramers has the objective to make each one of the residue type described above to have fully integer charges. The RESP was performed in two stages with different charge constraints to minimize the relative root mean square (RMS) difference to the precomputed QM ESP.

The first RESP stage for *pei+* imposes a total charge of +1 for both TPEIQ residues and for the central PEIQ residue. All symmetric heavy atoms were set to have the same derived partial charge and the H atoms of each symmetric heavy atom were also set to have the same charge. Second stage received as input the charges from stage one. Now, the partial charges of each N atom and its respective H atoms were frozen (will not be changed in this new stage) making the new derivation to affect allow the C atoms and its H atoms. Again, this stage was performed respecting the symmetry of each atom and the same constraints as the prior stage.

For *peis* and *pein* a similar two stage RESP were also performed, but with slight differences at the constraints. The first stage RESP of *peis* used constraints for all the 5 residues present in the tetramers with TPEIQ residues and PEIQ residue having total charge of +1 and the PEI residues with total charge of zero. Second stage kept the partial charges of heavy atoms and allow for all the H atoms to have a new partial charge. Both stage respect the symmetry of all the atoms involved. For *pein* the first stage used constraints of total zero charge for TPEI and PEI and symmetry of heavy atoms, while the second stage kept the constraints but now allow for new partial charges for H atoms with respect to them symmetry to the whole tetramer.

2.2 Polyurea dendrimer parameterization within Martini 3 FF

The setup of the Martini 3 topology for a fourth-generation polyurea dendrimer was based on AA simulations performed by N. Martinho (unpublished work). This simulation was performed with NAMD v.2.9.[75] and parameterized with CGenFF [76, 77, 78] for a duration of 20 ns at explicit solvent and kept at constant temperature and pressure of 310k and 1 bar, respectively.

The AA-to-CG mapping was done following the Martini philosophy, where each bead represents a specific set of atoms (with up to 5 non-hydrogen atoms per bead) and their type is determined by the properties of the chemical moieties that they represent. The symmetry of the dendrimer was considered when the substructure representation of each bead was elected. The step by step and rationale behind this stage is reported at the results section.

The target bonded parameters for the dendrimer topology were generated by converting the AA MD trajectory into a CG trajectory, following the mapping chosen. Distributions were plotted for the relevant bond distances, angle bendings and dihedral torsions. The choice of all bonded parameters was made so that CG simulations reproduced as close as possible these distributions. The fitting procedure was done in a trial and error manner, where each of the bonded parameters of a new simulation was refined based upon the fit from the previous run.

2.3 PURE$_{G4}$-OEI$_{48}$ building process

Two different strategies were used during the process of building the nanoparticle topology. The first one, consisted in represent the dendrimer structure of PURE$_{G4}$-OEI$_{48}$ as a hollow sphere with a “dummy” particle (without non-bonded interaction with others beads from the system) at its center; all 48 OEI chains were restricted at a distance of 1.725 nm from this center, thus lying on the sphere’s surface. This simplified first approach was used in the hope that the high density of OEI chains was able to “hide” the dendrimeric core from interacting with the rest of the system and thus avoid the need for its explicit modeling.

After initial simulations were ran, we found that the OEI chains were not able to efficiently shield the nanoparticle’s core: solvent and ion beads were able to access the hollow core. A second approach was implemented, which consisted in explicitly representing the polyurea dendrimer core of the nanoparticle coupled to all OEI chains as a single topology. All parameters were taken from the parameterization process of both OEI and PURE. The connection between each OEI chain and its respective NH_3^+ anchoring terminal is described in section 3.6.

2.4 All-atom Molecular Dynamics simulations

To perform all AA MD simulations, Gromacs version 2018.3 [58] or higher were used implementing a leap-frog algorithm for integrating Newton's equations of motion with a time step of 2 fs. The neighbor searching as set with Verlet cut-off scheme with grid type and a cut-off distance of 14 Å for both Van der Waals and Coulombic interactions. Periodic boundary conditions were applied in all directions, while the system was solvated with TIP3P water model and the long-range electrostatic interactions were treated with the Particle Mesh Ewald method of order 4 and using a grid spacing of 1.6 Å. The temperature was fixed at 300 K using a temperature coupling using velocity rescaling with a stochastic term with time constant of 1 ps. Pressure was treated using an isotropic Parrinello-Rahman coupling with a time constant of 5 ps and reference pressure of 1 bar.

2.5 Coarse-grained Molecular Dynamics simulations

All CG MD simulations were carried out using Gromacs version 2018.3 or higher employing leap-frog propagation with a time step of 20 fs, a Verlet cut-off scheme of type grid and periodic boundary conditions in all directions using a 11 Å cutoff for the short-range interactions (Van der Waals and Coulombic interactions). Long range electrostatics were treated with the reaction-field method with a relative dielectric constant ϵ_r = 15 in conjunction with with standard water beads, and infinite screening beyond the cutoff distance. The temperature was kept fixed at 300 K using stochastic velocity rescaling with a (weak) coupling constant of 1 ps, while pressure was treated with an isotropic Parrinello-Rahman coupling, a time constant of 12 ps and reference pressure of 1 bar. For equilibration purposes the berendsen thermo- and barostats were used instead.

2.6 Molecular Dynamics simulations with membrane models

The initial configuration for the POPC:POPG (1:3) bilayer was built using Martini's bilayer building tool – ”insane.py” [79]. This tool randomly distributes both lipids in the corresponding ratio into a planar bilayer centered around the midpoint of a specific box's height. In this case a hexagonal box of dimensions 70.0 nm X 60.6 nm X 20.0 nm was used. For the simulations with only POPC a bilayer of the same size was created using only this type of lipid.

The nanoparticle was added into the lipid bilayer box with the aid of VMD [80]; water beads that overlapped with it were removed for initial numerical stability. Enough Na^+ and Cl^- ions were added to neutralize the overall charge and have a salt concentration of 150 mM.

The two membrane systems were minimized and equilibrated as the PURE$_{G4}$-OEI$_{48}$ nanoparticle, with the difference that semi-isotropic pressure coupling was used, to decouple solvent pressure in z from membrane tension in xy. Both minimization an equilibration were performed with a restraint at the central bead of the nanoparticle to avoid displacement towards the membrane during these steps. All production simulations were run for at least 3 μs. As a strategy to confirm the lack of interaction between the nanoparticle and the POPC membrane, after the system was equilibrated a small simulation with an acceleration of -1.0 nm·ps^{-2} was performed to produce a initial position were the nanoparticle is in close contact with membrane. After achieving this, the simulation ran freely, the same way as the POPC:POPG system.

2.7 End-to-end distance, D_{ee}

The end-to-end distance, D_{ee} correspond to the norm of the vector that points from one end of the polymer chain to the other. This property helps indicate how extended a polymer chain is and is given by the equation 2.3:

$$D_{ee} = \sum_i \vec{r_i} \tag{2.3}$$

Where $\vec{r_i}$ represents the translation vectors that connects the polymer chains joints.

2.8 Radius of Gyration, R_g

The Radius of Gyration (R_g) was used to determine if the topology generated could reproduce the same behavior as the one measured from the atomistic model. R_g corresponds to the RMS of distance from all beads to the particle center of mass, and was calculated with equation 2.4:

$$R_g = \sqrt{\frac{1}{M}\sum_{i=1}^{N} m_i(r_i - R)^2} \tag{2.4}$$

Where, m_i is the mass of each bead i and $M = \sum_{i=1}^{N} m_i$, N is the number of beads that compose the particle, r_i is the position of bead i and R is the position of the particle center of mass.

2.9 Shape Parameter, S and Asphericity, Δ

To evaluate the general shape that the nanoparticle assumes along the entire trajectory, two properties were investigated: the shape parameter (S), that evaluates the shape itself, and asphericity (Δ) that is an indication of the extent of the shape's anisotropy [81]. Both properties are calculated using the moment of inertia tensors, $T_{\alpha\beta}$:

$$T_{\alpha\beta} = \frac{1}{2N^2} \sum_{i,j=1}^{N} (r_{i\alpha} - r_{j\alpha})(r_{i\beta} - r_{j\beta}) \tag{2.5}$$

Where α and β represent the components x, y, z of r_i. From T, its eigenvalues, λ_i are defined as the squares of the three principal radii of gyration, thus:

$$R_g^2 = trT = \sum_{i=1}^{3} \lambda_i \tag{2.6}$$

With inertia tensors and their eigenvalues defined, the overall shape can be characterized as:

$$S = 27 \frac{\prod_{i=1}^{3} (\lambda_i - \lambda)}{(trT)^3} \tag{2.7}$$

S can assume values from (-1/4) up to 2. The negatives values indicate an oblate shape, whereas positive values indicate a prolate shape; a perfect sphere yields $S = 0$. Asphericity is determined as:

$$\Delta = \frac{3}{2} \frac{\sum_{i=1}^{3} (\lambda_i - \overline{\lambda})^2}{(trT)^2} \tag{2.8}$$

In the same fashion as S, Δ will take values from 0 up to 1, where zero indicates the perfect isotropy of a sphere, and 1 maximal anisotropy.

2.10 Distance-to-core and contacts analysis

Two quantitative assays were performed where the distance-to-core and the percentage of contacts were investigated. The distance to the core of the membrane was defined as the minimum distance between each external bead of the nanoparticle's dendrimer layer (the beads that anchor the polymer chains) and the last beads of the phospholipids tails (C4A and C4B) of each membrane's inner leaflet. This metric is being used as a proxy for particle–membrane in-depth interaction but without the requirement to define a membrane normal — which can be troublesome where there is membrane curvature. Membrane contacts were defined as the percentage of a nanoparticle's beads been within 5 Å of any phospholipid bead. Distance-to-core results were expressed in the form of histograms. The percentage of contacts indicates how much of the whole particle indeed interacts with the membrane.

2.11 Radial distribution function, $g(r)$

The radial distribution function ($g(r)$ or RDF) describes how the density of a certain system component, relative to the bulk, varies as a function of the distance to a reference. An interparticle RDF is calculated by histogramming the distances between all particles pairs from a test and a reference groups, a and b. It can be calculated by the following expression:

$$g(r) = \frac{1}{N_a N_b} \sum_{i=i}^{N_a} \sum_{j=i}^{N_b} < \delta(|r_i - r_j| - r) > \tag{2.9}$$

This equation is normalized to the bulk density of the test group, so that for large distances in a macroscopically homogeneous system the RDF tends to 1 (indicating no influence from one particle on another's position at large distances).

All numerical analysis were performed using the MDAnalysis package for Python 3 [82, 83], either directly or in tools developed in-house.

CHAPTER 3 - RESULTS

3.1 Poly(ethylenimine) parameterization within the Amber FF

3.1.1 Optimization of partial atomic charges

The optimization of the partial charges was done following the RESP method. After finishing the charge assignment all the results were assessed to make sure that the two main conditions imposed were followed: same atomic charge for symmetric atoms and resulting integer charge of +1 or zero for each one of the residues of each tetramer. For *pein* the geometry-optimized structure is not absolutely symmetric due to the asymmetry of the single N–H bonds; final atomic charges of the H atoms in groups CH_2 were taken as the average of each pair. The final atomic charge for all the tetramers can be found in tables A.1, A.2 and A.3

3.1.2 Atom type designation and Lennard-Jones parameters by similarity

The atom type and LJ parameters were assigned based on analogy from existing atom type provided by amber99sb-ildn. Table 3.1 display the full list of all the atoms present in this work.

Table 3.1: Atom type and Lennard-Jones parameters

Atom type	ϵ (kJ/mol)	σ (nm)	Description
CT	0.4577300	0.339967	sp^3 aliphatic C
H	0.0656888	0.106908	H bonded to nitrogen atoms
H1	0.0656888	0.247135	H aliphatic bonded to C with 1 electrwd. group
HP	0.0656888	0.195998	H bonded to C next to positively charged gr
N3	0.7112800	0.325000	sp^3 N for amino groups

3.1.3 Optimization of dihedral parameters

As described above, the optimization procedure for the dihedrals consist in a scan of torsion coordinates with the objective of minimizing the torsion dihedral potential energy difference between QM and MM by fitting the force constant, phase and multiplicity of the dihedral potential function (eq. 2.1).

Both dihedrals of interest for each tetramer were rotated a full 360° in steps of 5°. For each angle the configuration with the minimum energy between all possible arrangement of H atoms was chosen as the input for the QM calculation.

After addition of the fit potentials to the MM energy, the agreement between the MM torsion profiles and the QM references for all dihedrals can be seen in figures 3.1, 3.2 and 3.3 . The parameters obtained for each one of the fits can be seen in table A.1.

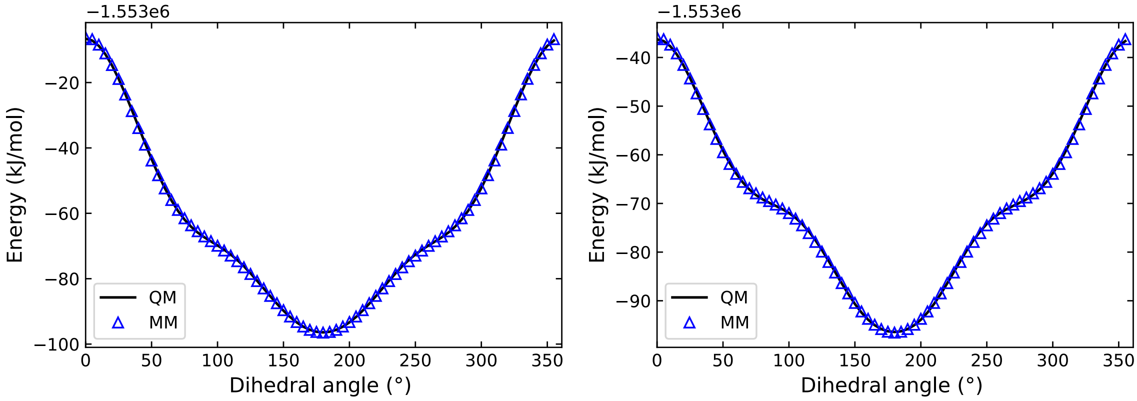

(a) N3-CT-CT-N3 dihedrals.

(a) CT-CT-N3-CT dihedrals.

Figure 3.1: QM and MM potential torsion energy fit for tetramer *pei*+.

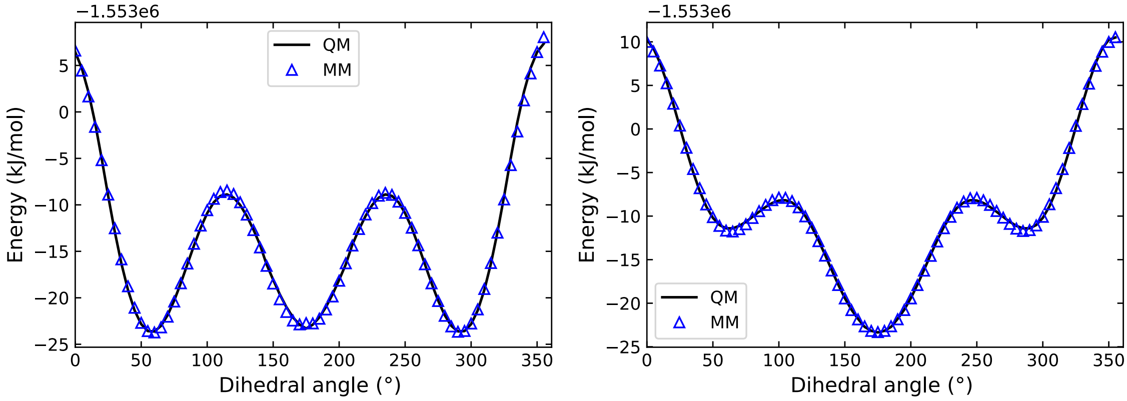

(a) N3-CT-CT-N3 dihedrals.

(a) CT-CT-N3-CT dihedrals.

Figure 3.2: QM and MM potential torsion energy fit for tetramer *peis*.

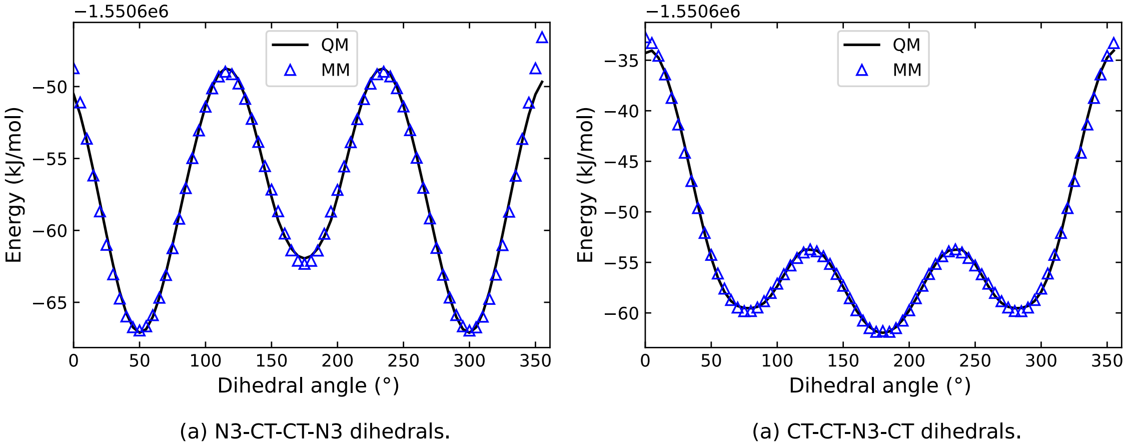

(a) N3-CT-CT-N3 dihedrals.

(a) CT-CT-N3-CT dihedrals.

Figure 3.3: QM and MM potential torsion energy fit for tetramer *pein*.

For the dihedrals from *pei+*, the RMS error (RMSE) of 0.164 and 0.231, respectively, are quite minimal and the superposition of profiles are almost perfect (Fig. 3.1). The fit for the dihedrals from *peis* also present a good superposition of profiles (Fig. 3.2) and RMSE values (0.924 and 0.184, respectively) not far from those for *pei+*. Of all the fits, the results for *pein* were the ones that presented the largest deviation and RMSE values, but still with a good overall fit (1.926 and 0.675, respectively). Discrepancies may stem from the multitude of asymmetric states in *pein* and the above-mentioned need to average charges after RESP.

The results are in agreement with the observation by others [84, 71] that a higher degree of protonation implies higher rotational barriers. This is a result of the repulsion between the positively charged amines pushing towards a fully trans configuration.

3.2 Poly(ethylenimine) all-atom Molecular Dynamics

The newly parameterized Amber model was used for systematically study the dynamic behavior of linear PEI of different lengths and degrees of protonation. Also, to understand how ionic strength impacts the structure of the polymer, simulations was also performed in a solvated system with 150 mM NaCl for each one of the length and protonation states. This is important since most biological systems of relevance have similar salt concentrations [85]. To performed the necessary analysis, three different sizes were chosen, to enable a comparative analysis with the literature. These sizes are of 25, 37 and 49 repeating units.

The neutrality of all the simulated systems was ensured by adding a number of Cl^- counterions matching the number of protonated PEI monomers. For the system with salt, the amount of additional Na^+ and Cl^- ions needed was calculated specifically for each system, since the amount of water particles changes between them.

All simulation boxes were made as dodecahedral unit cells and had initial size to accommodate the fully extended polymer chain and screen its interactions with its periodic replicas. For each one of the combinations a minimum of 200 ns was collected from small sets of 20 ns trajectories, which were individually energy-minimized and equilibrated prior to simulation. Figure 3.4 shows a snapshot of the typical extension of the fully protonated PEI 49-mer under physiological salt conditions.

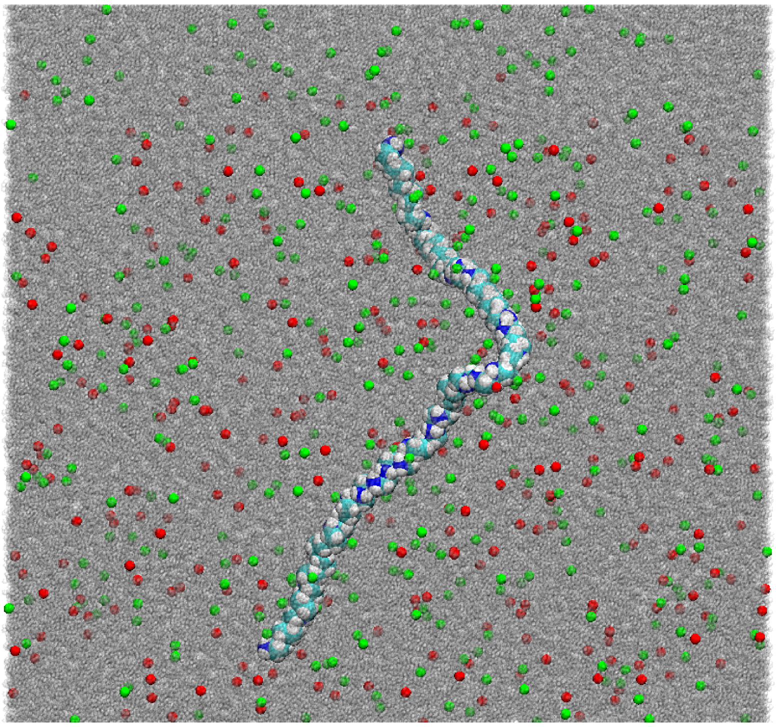

Figure 3.4: Snapshot of a typical configuration of a fully-protonated PEI 49-mer (red dots correspond to Na^+ and green to Cl^-).

3.2.1 Radius of gyration and end-to-end distance analysis

To investigate the behavior and the spatial evolution of the simulated PEI chains in the above solvated systems, we utilized two common indicators of polymer structure: the end-to-end distance, D_{ee}, and the radius of gyration, R_g. Tables 3.2 and 3.3 shows the averaged values for both indicators for the three different sized polymer chains (described above) in all protonation states studies and in both salt concentration conditions.

Table 3.2: Average end-to-end distance, $\langle D_{ee} \rangle$ (nm)

Chain size	Non-protonated		Semi-protonated		Fully-protonated	
	no salt	salt	no salt	salt	no salt	salt
25-mer	2.23 ± 0.84	2.31 ± 0.79	3.95 ± 0.74	3.57 ± 0.84	6.25 ± 0.51	5.96 ± 0.77
37-mer	2.78 ± 1.03	2.93 ± 1.15	5.92 ± 0.95	4.76 ± 1.17	8.98 ± 0.94	8.11 ± 1.49
49-mer	3.32 ± 1.29	3.28 ± 1.22	7.74 ± 1.27	5.92 ± 1.51	11.73 ± 1.21	9.92 ± 2.07

Table 3.3: Average radius of gyration, $\langle R_g \rangle$ (nm)

Chain size	Non-protonated		Semi-protonated		Fully-protonated	
	no salt	salt	no salt	salt	no salt	salt
25-mer	0.98 ± 0.19	1.01 ± 0.18	1.39 ± 0.15	1.31 ± 0.17	1.94 ± 0.09	1.89 ± 0.13
37-mer	1.20 ± 0.23	1.25 ± 0.26	2.03 ± 0.19	1.77 ± 0.23	2.82 ± 0.15	2.67 ± 0.24
49-mer	1.41 ± 0.29	1.42 ± 0.25	2.65 ± 0.25	2.19 ± 0.29	3.70 ± 0.19	3.35 ± 0.37

The values stated for both $\langle D_{ee} \rangle$ and $\langle R_g \rangle$ indicate that they are dependent on the degree of protonation and the salt concentration. The more charged amino groups are present in the polymer chain, the higher these averages are. This shows that the polymer tends to prefer a more coiled configuration at a lower protonation degree, and with the increase of protonation the chain start to become more extended — a clear effect of electrostatic repulsion between the positive charges of the protonated amines. In the presence of ionic strength, the tendency is the opposite and the polymer chain shrinks, showing that the ions mediate interactions between charges and reduce the repulsion effect. These can be better perceived when comparing the non-protonated chains: the statistical difference between the two ionic concentrations, for all PEI lengths, is essentially null, implying that the salt ions have no charge repulsion to mediate and the polymer behaves equally.

The sizes and conditions simulated also allowed for comparison with previous work that employed Amber FF. Choudhury and Roy [84] presented results for $\langle D_{ee} \rangle$ and $\langle R_g \rangle$ that follow the same dependence upon protonation, but with averages around 14% and 17% smaller for the end-to-end distance and radius of gyration, respectively. This difference is a reflection of higher force constants for the dihedrals torsion derived from the QM data of this work, which returns a polymer chain more rigid then previously reported.

Most recently Beu, Ailenei, and Farcaş [86] in 2018, published a CHARMM FF for linear PEI. The results for the non- and semi-protonated version under non salt concentration conditions are compared in table 3.4. As can been seen, all the values are within statistical error showing the good agreement between the parameterization performed for this polymer under different force fields. Also the values are in agreement with some experimental results reported so far: in 2007, Zakharova et al. [87] reported experimental values for a 20-mer size PEI for D_{ee} of 2.2 nm and R_g of 0.9 nm that are close to the ones for our size 25-mer, while Beu, Ailenei, and Farcaş [86] and Perevyazko et al. [88] reported a similar increase of end-to-end distance of linear PEI chains with molecular weights in the range 1100 to 13,900 g/mol.

Table 3.4: Computed–experimental comparison of end-to-end distance and radius of gyration for PEI 50-mer under no salt conditions

	Non-protonated		Semi-protonated	
50-mer	Ref. [86]	This Work	Ref. [86]	This Work
D_{ee} (nm)	3.96 ± 0.21	3.32 ± 1.29	7.02 ± 0.27	7.74 ± 1.27
R_g (nm)	1.63 ± 0.05	1.41 ± 0.29	2.64 ± 0.05	2.65 ± 0.25

3.3 Poly(ethylenimine) mapping

The modeling of our Martini 3 PEI starts out by defining the CG beads mapped to represent the residues defined in the Amber model (terminal residues, encompassing 1.5 units each, are represented by two beads). Figure 3.5 shows the mapping used for all PEI chains, where both three-to-one (S or ‘small’, green) and two-to-one (T or ‘tiny’, blue) bead types are used. The beads’ respective mass-centers and identifications are:

- TBP: terminal protonated bead - $NH_3^+{-}CH_2$ -
- TBN: terminal non-protonated bead - $NH_2{-}CH_2$ -
- MBP: protonated monomer bead - $CH_2{-}NH_2^+{-}CH_2$ -
- MBN: non-protonated monomer bead - $CH_2{-}NH{-}CH_2$ -

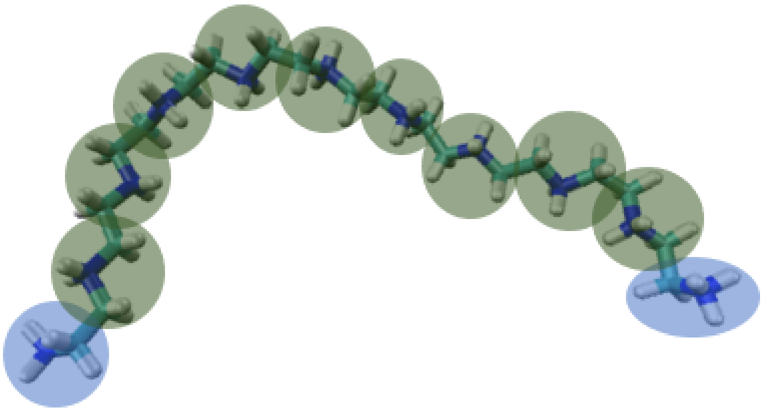

Figure 3.5: Mapping scheme for fully-protonated PEI chains. Blue bead represents TBP (or TBN for non-protonated chains) and green represents MBP (or MBN for non-protonated and semi-protonated chains).

3.4 Poly(ethylenimine) parameterization within Martini 3 FF

The determination of the non-bonded LJ parameters for a CG Martini model is based upon the physico-chemical similarities between the chemical group mapped into each bead and the standard types already parameterized by the FF in question. Martini 3 expands the different types already present in Martini, allowing for more refined interaction levels to choose from. For our case, and following the guidelines for Martini 3 — already generally laid out in the Martini 3 open beta version [68] — the general idea is that beads with positive charge must be of type 'Q' and receive a p (for positive) label. Beads without charge were assigned the type 'N', since they represent moderately-to-weakly polar groups; of those, beads encompassing NH_2 will receive a hydrogen-bond-donor label ('d'), since they have one more hydrogen bond donor than acceptors, while beads with NH are going to be regular (no such label), since they have the same number of hydrogen-bond donors and acceptors. To determine the size of the beads, an 'S' or 'T' prefix indicates small and tiny beads, respectively, while normal size (four-to-one mapping) beads have no prefix. Finally, the polarity level within each type is dictated by the production of partition behavior, leading to the following assignment:

- TBP: $NH_3^+{-}CH_2$ - TQ4p
- TBN: $NH_2{-}CH_2$ - TN6d
- MBP: $CH_2{-}NH_2^+{-}CH_2$ - SQ3p

- MBN: $CH_2-NH-CH_2$ - SN3

With bead types assigned to each of the residues of our polymer, the bottom-up process of getting bonded interactions derived from reference all-atom simulations can start. The generated AA trajectories were all converted to the mapping described above by placing single beads at the center of mass of the corresponding atoms. Afterward, histograms of the different bond, bending angle and dihedral distributions were calculated, from which initial estimates for the parameters of the bonded potential functions could be made. A subsequent trial-and-error approach was employed, where polymers with tentative CG parameters were simulated, their bonded distributions plotted and compared to the CG-mapped AA ones, and parameters adjusted by hand before simulating anew. The procedure ended when a good overlap with AA distributions was achieved.

The set of AA trajectories used consisted of polymer chain of size 5, 8, 10, 11 and 13-mer, for each of the protonation states, with at least 300 ns of simulation each. To better reflect physiological behavior, the CG parameterization of bonds, bending angles and dihedrals was done under 150 mM NaCl and compared to the AA simulations also with ionic strength. For simplicity, the main text focuses on the distribution obtained for the fully-protonated PEI chain, while for the other chains all plots and parameters are in Figures A.1 - A.6 and Tables A.2 - A.4. Each one of the different bonds, bending angles and dihedrals are described by the bead names that form them, so, for the chain in question, two bonds, two bending angles and two dihedrals had to be parameterized. Figure 3.6 shows the plot fit for the bonds. The TBP-MBP bond has a well defined peak around 0.265 nm and a smaller one at 0.295 nm. With the object to better reproduce this distribution in the CG level, b_0 adopted was 0.275 with a force k_b of 13,000 kJ mol^{-1} nm^{-2}. With only one peak, bond MBP-MBP has it equilibrium value at 0.310 nm and force k_b of 15,000 kJ mol^{-1} nm^{-2}. The slight difference in forces between the two bonds reflects a more narrow or wider distribution profile around the equilibrium distance, which in turn is a consequence of the different degrees of freedom of the underlying atoms.

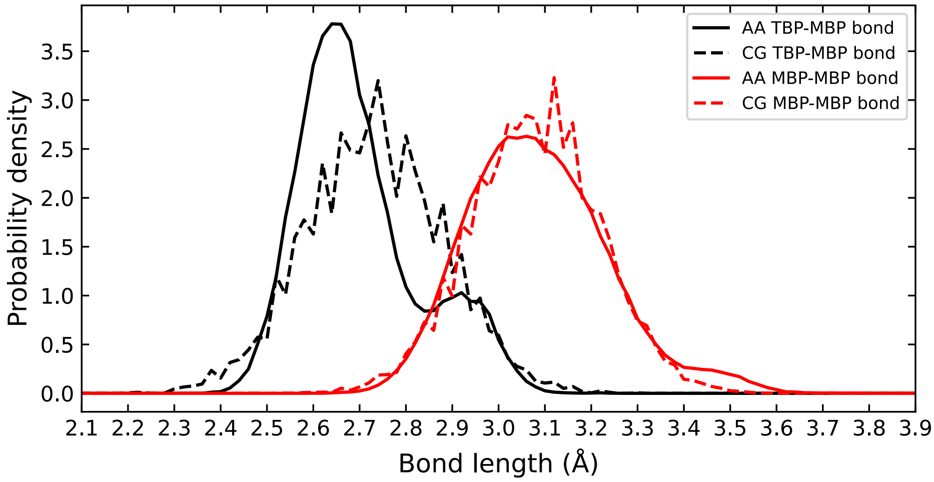

Figure 3.6: Atomistic (solid) and CG (dashed) probability distribution for the TBP-MBP (black) and MBP-MBP (red) bead bond distances.

Regarding the bending angle distribution (Fig. 3.7), two well-defined profiles were obtained for TBP-MBP-MBP and MBP-MBP-MBP, with both values of equilibrium above 150°. The structural averaging involved in the CG mapping of AA coordinates highlights the tendency of the fully-protonated linear PEI to prefer a more extended conformation (mapped bending angles closer to 180°) than a coiled one. For angle TBP-MBP-MBP the parameters are $\theta_0 = 153^\circ$ and k$_\theta$ $= 250 kJmol^{-1}$, while angle MBP-MBP-MBP has values of $\theta_0 = 170^\circ$ and k$_\theta$ $= 225 kJmol^{-1}$.

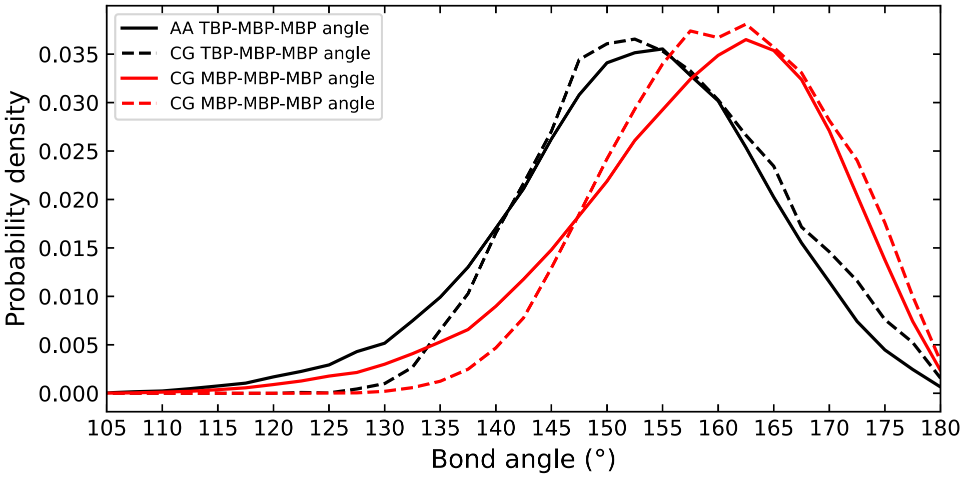

Figure 3.7: Atomistic (solid) and CG (dashed) probability distribution for the TBP-MBP-MBP (black) and MBP-MBP-MBP (red) bending angles.

Prior to defining the parameters for the dihedral torsions, the above analysis of CG-mapped bending angles indicates the possibility of TBP-MBP-MBP or MBP-MBP-MBP beads to become close to colinear. This tendency, coupled with the relatively large 20 fs integration time step leads to singularities in the differentiation of torsion potentials, and unrealistically high forces that will crash the simulation [89]. To work around this problem, while keeping the advantages of a larger time step from CG simulations, we used the combined bending-torsion potential proposed by Bulacu et al. [90]:

$$V_{CBT}(\theta_{i-1}, \theta_i, \phi_i) = k_\phi sin^3\phi_{i-1} sin^3\phi_i \sum_{n=0}^{4} a_n cos^n \phi_i \tag{3.1}$$

Equation 3.1 couples the dihedral torsion potential, in a cosine form, with the potential functions of the adjacent bending angles in a single expression. This has two main advantage: first, the two sine pre-factors cancel the torsion potential and force when either of the two bending angles approaches the value of 180°. Second, the dependency in ϕ_i is expressed by the cosine polynomial that avoids the singularities in the torsional force computation. Table 3.5 show the parameters obtained for the accurate fit from figure 3.8.

Table 3.5: Torsion potential parameters for dihedrals of fully-protonated linear PEI. All values are in kJ mol^{-1}

Dihedrals	k_ϕ	a_0	a_1	a_2	a_3	a_4
TBP-MBP-MBP-MBP	75	1.41	2.95	1.36	1.33	1.00
MBP-MBP-MBP-MBP	65	1.41	2.95	1.36	1.33	1.00

Is clear that both dihedrals behave similarly. The slight difference in k_ϕ (10 kJ mol^{-1}) is reflected by distributions of slightly different widths.

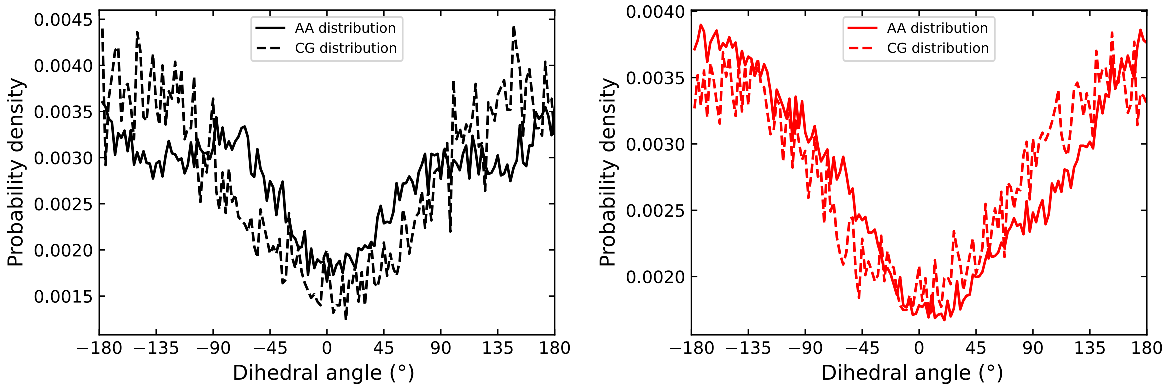

(a) TBP-MBP-MBP-MBP dihedral

(a) TBP-MBP-MBP-MBP dihedral

Figure 3.8: Atomistic (solid) and CG (dashed) probability distribution for the a) TBP-MBP-MBP-MBP (black) and b) MBP-MBP-MBP-MBP (red) torsion angles.

3.5 Comparison between Amber and Martini 3 behavior

With the set of parameters that reproduce all the bonded interactions of linear PEI, it becomes necessary to check if they will also be able to simulate the previously described structure indicators. Again, simulations were performed with the whole set of conditions used so far. Since now we are working with a CG model, a longer trajectory is much more feasible to produce and all the values were calculated considering at least 1 μs. Figure 3.9 depicts the averaged end-to-end distance and radius of gyration for the no salt condition for the CG simulations (marked as void circles) and the reference AA values (marked as full circles).

Both plots at Figure 3.9 show that the CG model developed can reproduce the atomistic behavior of the non- and fully-protonated states of the linear PEI. When observing the results for the non-protonated state, since the polymer does not present any charge, the high electrostatic screening does not apply to the polymer and the CG model is able to reproduce faithfully the AA description. Another observation is that there may be a small tendency for the values from the CG simulations to be lower than the ones from AA. This is partly explained by the fact that parameterization was performed emphasizing the reproduction of behavior at high ionic strengths, where the polymer is less extended. Nevertheless, the values are still within the error of each other.

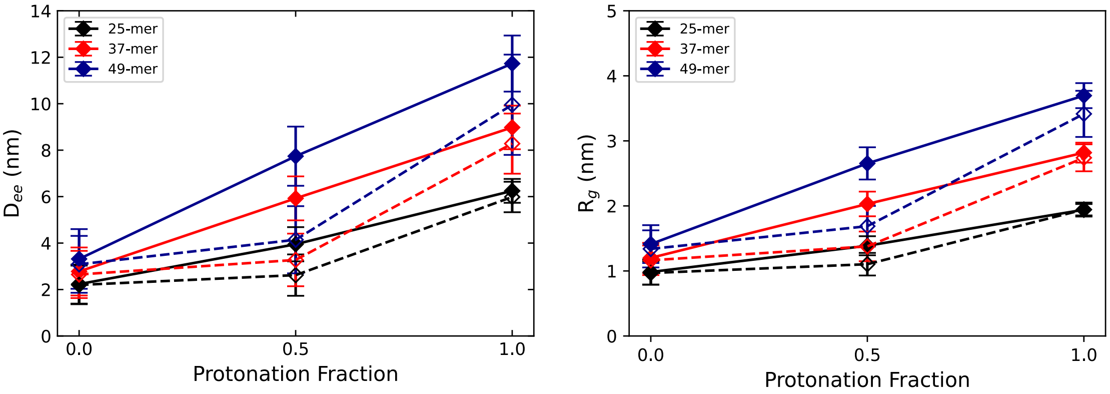

Figure 3.9: End-to-end distance and radius of gyration for PEI chains under no salt condition. AA values are represented by full circles and continuous lines while CG are void circles with dashed lines.

For the semi-protonated state, we can observe that the CG model under-represents the behavior of the polymer when semi-protonated, with the values of R_g and D_{ee} being, on average, 29 and 41% smaller then the atomistic one. The excessive compactness of the CG model for this protonation state is a consequence of the coarseness with which explicit charges are treated in Martini: because water is not explicitly polar (polar/polarizable CG water models do exist [91] but are not yet developed for Martini 3) dielectric screening is mimicked by a large relative permittivity of 15 in the simulation. This implicit screening seems to overly dampen electrostatic interactions at the longer distances involved in nonconsecutive amine repulsion. The same shortcomings were observed by Beu, Ailenei, and Costinaş for Martini 2, where a correction could be made by using a polarizable water model [91] — at the cost of a heavier computational effort.

When looking into the simulations under salt conditions (fig. 3.10), we are able to see that the agreement between CG and AA models for the the semi-protonated state improves by about 40% for both the averaged D_{ee} and R_g. This, again, can be explained by the excess of positively and negatively charges provident of NaCl that explicitly mediate the electrostatic interactions within the system, and thus also explaining a better agreement for the non and fully protonated versions.

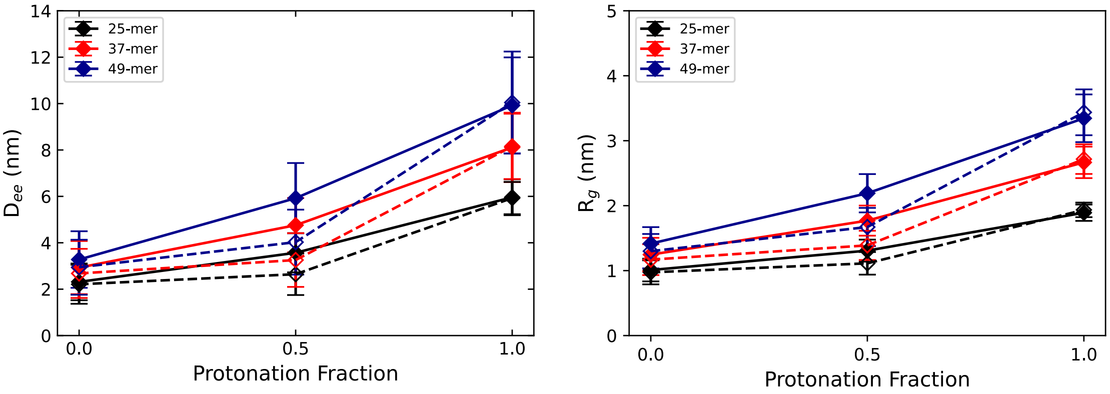

Figure 3.10: End-to-end distance and radius of gyration for PEI chains under 150mM of NaCl. AA values are represented by full circles and continuous lines while CG are void circles with dashed lines.

3.6 Polyurea dendrimer mapping

To create the most suitable mapping for PURE$_{G4}$, first it is necessary to know the structure of the molecule. Figure 3.11 shows a representation of the dendrimer core structure (up to second-generation):

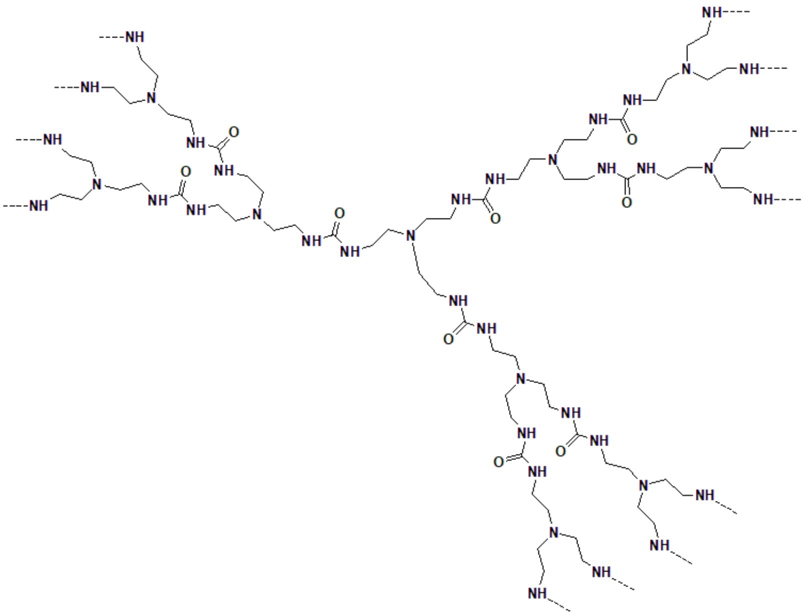

Figure 3.11: Partial structure of the PURE$_{G4}$ core (second generation shown). Dashed lines represent further repeating units.

The dendrimeric core keeps growing following the representation above until desired size is achieved. In this case, two more layers are added up and the final structure finishes with 48 NH_3^+ terminals, where the OEI chains will be added.

Taking into consideration the rationale from Martini philosophy and the structure above, the most adequate mapping to ensure the symmetry of the nanoparticle without splitting chemical groups and integer charges is to center the bead representation on two well defined chemical groups: the urea and the tertiary amine. Although Martini 3 allows for a greater refinement with three-to-one and two-to-one size beads — besides the original four-to-one mapping —, it was not possible to group the atoms in a way that respected the principles to be followed, so a larger representation had to be made where certain CH_2 groups were shared between beads. This strategy led to a five-to-one representation for the beads centered on the urea groups and a ”five-and-a-half”-to-one for the beads centered on the tertiary amines, with each shared methylene (CH_2) counting as half towards each bead. Figure 3.12 shows the representation of the tertiary amine (AM) and urea (UR) centered beads for the coarse-grained topology.

With the knowledge of what each bead represents, it is necessary to assign the correct type to each one. Since each bead represents branched structures, they will be treated as regular size beads, despite representing a larger amount of atoms from that of the traditional four-to-one mapping. This undermapping is not out of line with the philosophy of Martini 3, in which branched moieties are represented by beads corresponding to

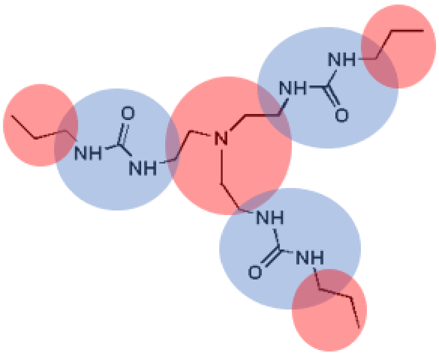

Figure 3.12: AM (amine; red) and UR (urea; blue) beads that represent the general mapping choice for the PURE$_{G4}$ dendrimer. Three extra red circles represent the amine groups of the dendrimer's next generation.

fewer atoms [68]. The AM bead, defined by a triethylamine scaffold, is considered to be nonpolar (type N) and receives an *a* label that represents the capacity to accept hydrogen bonds, while the UR bead, with its dimethylurea frame, is a polar (P) type bead, also with capacity to accept hydrogen bond and having the same *a* label. The interaction level of each particle was determined based on the chemical similarity between each group and validated examples provided by Martini 3. Since part of the representation of each bead is shared with, at least, another bead, the choice of interaction level was slightly tuned down from its reference and the level 3 and 4 were assigned, respectively, for AM and UR beads. To finish the bead type assignment all terminal NH_3^+ will be treated as TQ4p and named as 'NT' beads. This matches what was used as the first bead of the OEI chain topology and results in a perfect symmetry of the final nanoparticle PURE$_{G4}$-OEI$_{48}$ once it is assembled. In summary, the used Martini 3 bead types were N3a for AM beads, P4a for UR beads and TQ4p for NT beads.

3.7 Polyurea dendrimer parameterization

After establishing the dendrimer CG representation and the non-bonded parameters through bead type assignment, it is necessary to derive the values for all bonded features to finish the desired topology. There are three different kind of bonds: AM-UR and AM-NT bonds, and the NT-NT distance. The NT-NT distance, though not representing a covalent link, is parameterized to ensure the correct distancing between NT beads, especially after OEI chains are linked to them. Figure 3.13 shows all the fit between atomistic and CG probability distribution for all the bonds assigned.

While AM-UR and AM-NT bonds have well defined normal Gaussian distribution around 0.467 and 0.260 nm, and forces of 5000 and 6500 kJ mol^{-1} nm^{-2}, respectively, NT-NT distances spread over a range of values. To better reproduce this distribution, b_0 adopted was 0.425 nm with a force k_b of 1,750 kJ mol^{-1} nm^{-2}.

In a similar fashion, the same procedure was performed in order to obtain parameters for bending and torsion angles. The total of bending angles is four, defined by the coupling of the following beads: AM-UR-AM, UR-AM-UR, UR-AM-NT and NT-AM-NT. Figure 3.14 shows all probability distribution for the bending

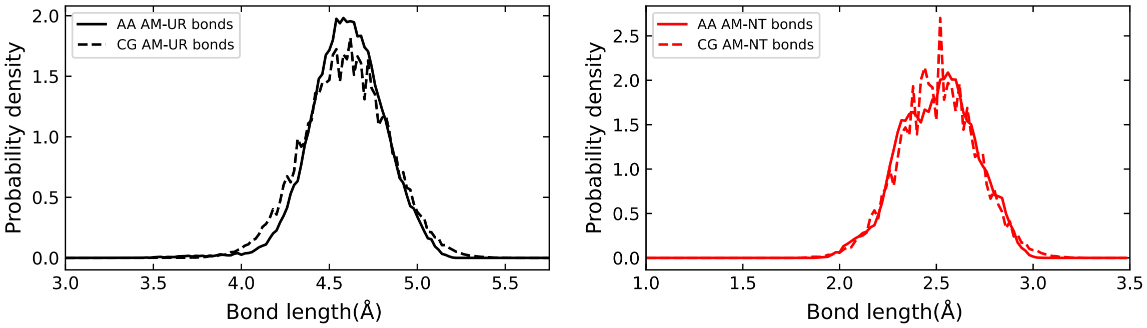

(a) AM-UR bond distance distribution

(b) AM-NT bond distance distribution

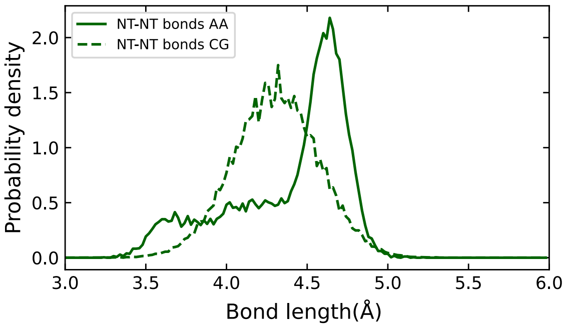

(c) NT-NT bond distance distribution

Figure 3.13: Atomistic (solid) and CG (dashed) probability distribution for all bonds' distances.

angles:

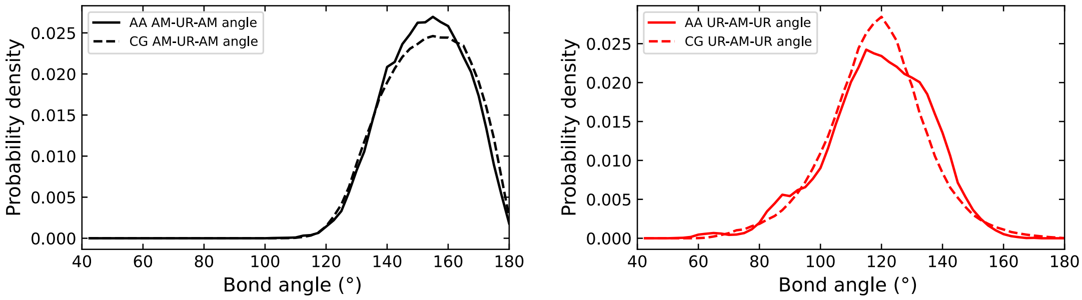

(a) AM-UR-AM bending angle distribution

(b) UR-AM-UR bending angle distribution

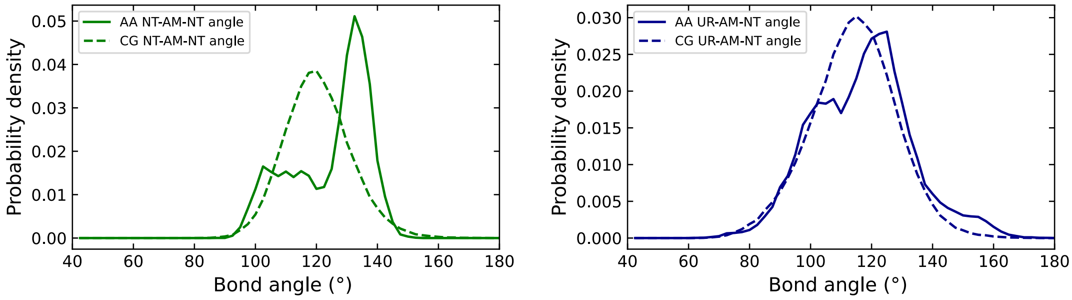

(c) UR-AM-NT bending angle distribution

(d) NT-AM-NT bending angle distribution

Figure 3.14: Atomistic (solid) and CG (dashed) probability distribution for all bending angles.

Again, the fit between atomistic and CG simulations is well defined, and the parameters for θ_0 and k_θ are, respectively: 180° and 80 kJ mol^{-1}; 130° and 30 kJ mol^{-1}; 120° and 50 kJ mol^{-1} and 117° and 40 kJ mol^{-1}.

In terms of torsion angles, Figure 3.15 shows that for all four dihedrals defined, there is no particularly strong distribution tendency. Because of this, and for parameter simplicity, it was chosen not to impose any torsion potential.

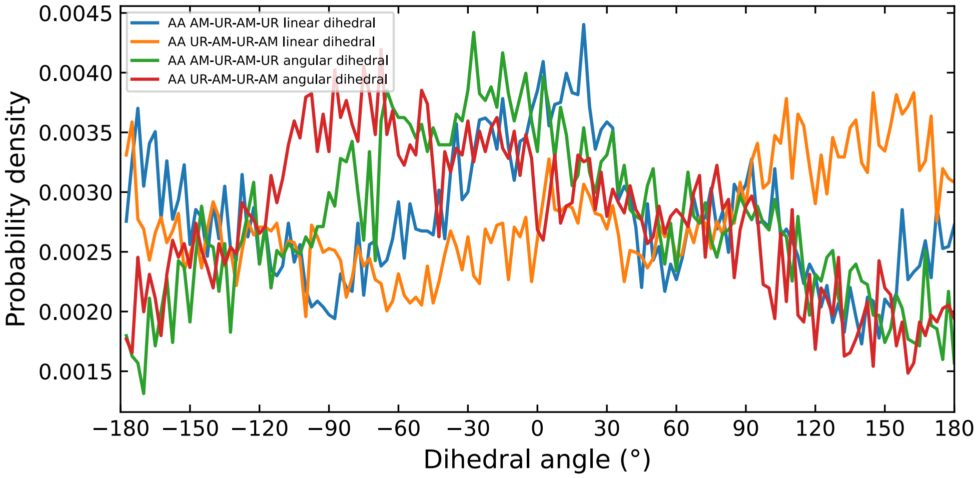

Figure 3.15: Atomistic probability distribution for all torsion angles.

As an evaluation of the relevance of the created polyurea topology, emergent properties of the dendrimer, such as the average simulated R_g, should match between atomistic and CG simulations. Table 3.6 shows that the CG is quite able to reproduce the physiochemical property of interest. The table hints that the CG topology may have a small deviation into a prolate shape and some asymmetry compared to the atomistic behavior, but not significantly enough to negate its validity.

Table 3.6: Average Radius of gyration (in Å), Shape parameters and Asphericity comparison between Atomistic and Coarse-grained topologies for PURE$_{G4}$.

	Atomistic	Coarse-grained
$\langle R_g \rangle$	21.44 ± 0.43	21.08 ± 1.09
$\langle \mathbf{S} \rangle$	0.001 ± 0.013	0.025 ± 0.045
$\langle \Delta \rangle$	0.050 ± 0.014	0.090 ± 0.045

3.8 Nanoparticle's structure

Having built the Martini 3 topology for PURE$_{G4}$-OEI$_{48}$ nanoparticle, it is imperative to check and understand its dynamics. Additionally, it is important to understand how the protonation state of the polymer chains can impact its overall behavior and shape. To do so, the average R_g, Δ and S of all protonation states (fully, semi and non-protonated OEI chains) of the nanoparticle were determined. To better understand the dynamics characteristics studied, all parameters were calculated considering two distinct groups of beads. First group consist solely of the beads of the dendrimer layer while the second one corresponds to the whole nanoparticle. Since the dynamics of the dendrimer was already studied separately, this strategy helps to point the contribution of the polymers' chains and, consequently, its protonation (Table 3.7).

From the table below its possible to notice that the average R_g for the dendrimer layers has the same

Table 3.7: Average Radius of gyration (in Å), Shape parameters and Asphericity of all three state of protonation from PURE$_{G4}$-OEI$_{48}$.

	Fully-protonated		semi-protonated		Non-protonated	
	Dendrimer	Nanoparticle	Dendrimer	Nanoparticle	Dendrimer	Nanoparticle
$\langle R_g \rangle$	19.723 ± 0.622	30.338 ± 0.894	20.889 ± 0.530	29.524 ± 0.638	19.562 ± 0.805	26.043 ± 1.034
$\langle \mathbf{S} \rangle$	0.022 ± 0.031	0.006 ± 0.014	-0.004 ± 0.018	0.000 ± 0.007	0.008 ± 0.040	0.006 ± 0.022
$\langle \Delta \rangle$	0.094 ± 0.039	0.039 ± 0.024	0.054 ± 0.025	0.026 ± 0.014	0.085 ± 0.041	0.053 ± 0.029

value (considering the error) across all three-protonation situation. That shows that the polymer chains that are attached has close to no effect in the dynamics of the dendrimer itself. When considering the whole particle, the difference in the average values of R_g starts to get the expected contribution from the polymer's behavior in solution. The smallest value for the non-protonation indicates that the OEI chains are, on average, in a coiled conformation, contributing less to the overall size of the nanoparticle when compared to the other two protonated states. The fully-protonated state presents the highest size for the nanoparticle, which agrees with the outspread conformation of OEI chains due to the strong charge repulsion encountered in this setting. The semi-protonated size tends towards that from fully-protonated. Despite anticipating a size midway fully and non-protonated, since this is the tendency already observed for the polymer chain in solution, this behavior can be an indicative that the charge concentration of all chains is high enough to provide a behavior closer to extended chains then coiled ones.

The shape assumed by PURE$_{G4}$-OEI$_{48}$ is almost perfectly spherical, since the average S is close to zero, independent of the state and if the structure been assessed is the dendrimer layer or the whole nanoparticle. The slightly anisotropy observed can be attributed to the minute deviation to a prolate shape, that is mostly being a contribution of the dendrimer. This behavior can also be perceived by figure 3.16, where the polymer chains (in red) changes conformation upon protonation, but the dendrimer itself (in blue) tends to have the same shape.

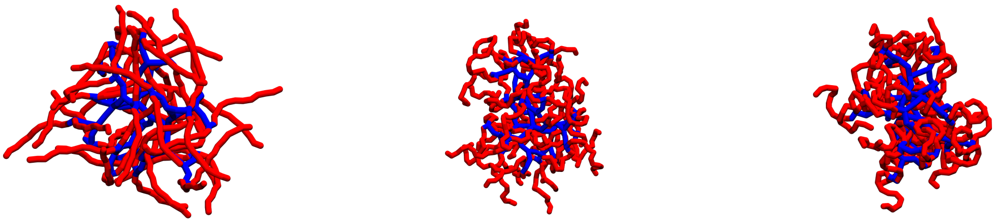

(a) Fully-protonated state (b) semi-protonated state (c) Non-protonated state

Figure 3.16: Average representation of PURE$_{G4}$-OEI$_{48}$ in all three different protonation state.

3.9 Nanoparticle at the membrane environment

With knowledge about the dynamic behavior of the nanoparticle, the next stage of this work was to evaluate how the interaction with different membrane systems occur and whether the desired selectivity towards bacterial membrane model can be observed. All trajectories were visually inspected to understand the mode of action related to possible permeabilization of membranes and distance-to-core and contacts numerical analysis were used to support such results.

3.9.1 Visual analysis

During visual analysis, it was clear that all protonation states tend to move towards and interact with the POPC/POPG membrane to some extent. When comparing interactions with POPC membrane, the fully- and semi-protonated stages move away from it, while the non-protonated nanoparticle is the only one to have interaction. This confirms that the presence of positive charges dictates the selectivity relative to different types of membranes.

Both fully- and semi-protonated states were able to induce the formation of binding pockets by forming negative curvatures upon interaction with the POPC/POPG system. It was possible to observe two different type of curvature interaction, which are possible early mechanisms in the antimicrobial activity of PURE$_{G4}$-OEI$_{48}$ (Fig. 3.17).

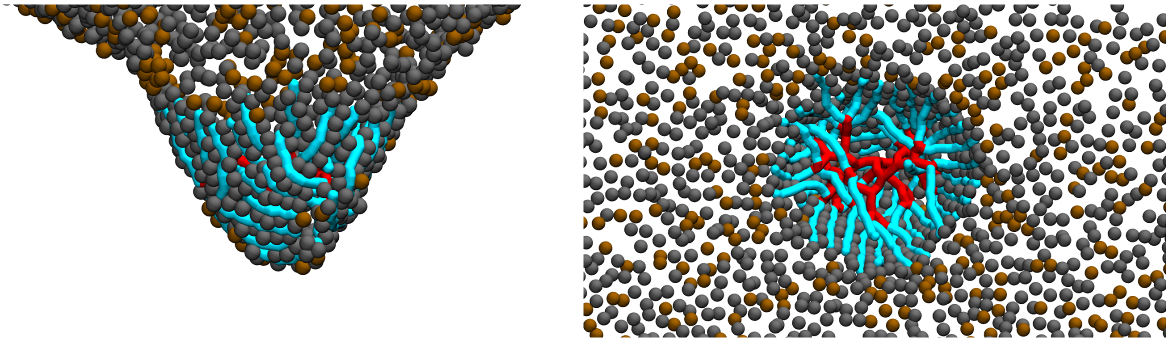

(a) Side view of fully-protonated interaction.

(b) Top view of fully-protonated interaction.

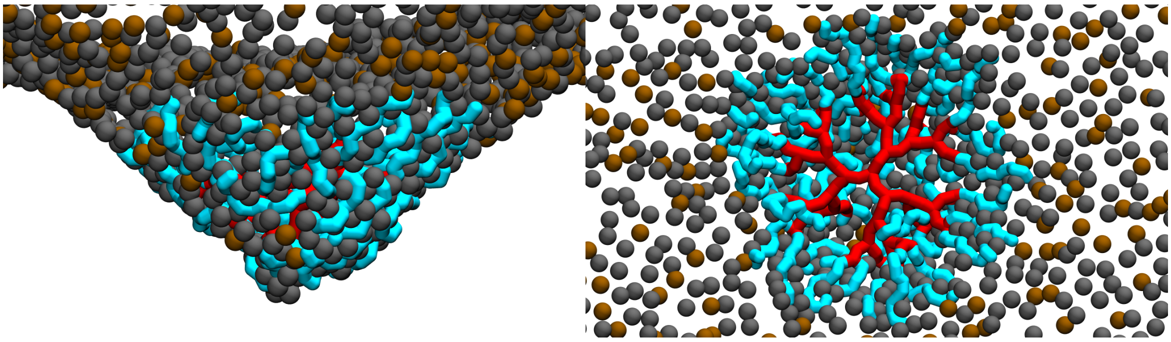

(c) Side view of semi-protonated interaction.

(d) Top view of semi-protonated interaction.

Figure 3.17: Side and top view of PURE$_{G4}$-OEI$_{48}$ interaction with POPC/POPG membrane, where red represents the dendrimer core, blue the OEI chains, gray the PO_4^- beads from POPG and brown PO_4^- from POPC.

Both Figures 3.17a and 3.17c show that after nanoparticle interaction it forms a cavity with negative curvature. In the case of the fully-protonated state, this cavity is deeper, and the OEI chains are arranged in an alternating and radial manner between the PO_4^- (dark gray beads) from POPG. For the semi-protonated nanoparticle, the generated cavity had shallower depth and the organization of the polymer chains along the PO_4^- no longer follows a defined pattern.

The difference in interaction between protonation states could also be observed from the top views (figs. 3.17b and 3.17d), where the dendrimer layer of the semi-protonated is more spread out and all external branches (the beads that anchor the polymers) are in closer contact with all PO_4^- beads, while part of the dendrimer from fully-protonated tends to curve up and away from the top of the outer leaflet.

This behavior can be explained by the difference in positive charge density express by each protonation state. With a charge density two times greater, the fully-protonated OEI chains will have more affinity for the anionic phospholipid and repulsion between chains, creating more tension that allows for the depth of the cavity and for the curvature of the dendrimer. For the semi-protonated, the charge density generates a more balance scenario between the attraction with the anionic lipid and repulsion between chains, which leads to less tension.

The ability to induce curvature has also been identified as one of the ways of AMPs to compromise the barrier function of membranes. Negative curvatures are generated by the strong electrostatic interactions between the cationic part of an AMP and the anionic headgroups of membrane phospholipids, while positive curvatures arise from the penetration of hydrophobic parts of the AMP into the lipids' tails due to the hydrophobic effect, and steric crowding interactions from coordinated stacking of lipid headgroups [92]. The combination of positive and negative curvatures at the same location can induce a saddle-splay type of curvature, which is the topology necessary to form a variety of known membrane destabilizing processes included budding, blebbing, vesicularization, as well as pore formation [92]. Negative curvatures also display the capacity to sort and modify the arrangement of cardiolipin (CL) into clusters [93] and bacterial cell membranes contain greater amounts of both anionic and negative intrinsic curvature lipids (such as CL) are more susceptible to be destabilized by deformation from curvatures [92]. It has also been computationally shown that curvature (either negative or positive) increases from one to three orders of magnitude the permeability to hydrophilic compounds, such as ions and water molecules [94]. The perturbation caused by this change in permeation can contribute to cell function destabilization and death.

The absence of pores and/or rupture of the membranes along the whole trajectories analyzed can be an indicative that the time scale of the simulations was not long enough to allow their development. In any case, the results so far point into a disruptive direction that can led to the desired final effects.

3.9.2 Membrane distance and contacts' assay

Following the visual observations, both distance-to-core and contact analyses help get a better insight regarding the interaction difference between protonation states. From the distance-to-core plots (Fig.3.18) some conclusions can be made. First, the higher selectivity towards charged states is again confirmed, with the distribution of fully and semi-protonated centered around 22.5 Å in the POPC/POPG systems, while for the POPC systems there is no significant interaction and plots reflecting uniform distribution in water are obtained. Also, the absence of positive charge results in the nanoparticle interacting with both membrane types in a similar manner. In fact, the lack of charge results in a closer contact with POPC than POPC/POPG, even though the preferred position is also centered around 22 Å. Another interesting point taken from these results is that even with preferred distribution centered around the same distance, the semi-protonated nanoparticle has just one peak, while the fully-protonated has two (one at 20.5 and a larger one at 26.5 Å). This may reflect the observed differences in the nanoparticle's structural conformation when in contact with the membrane.

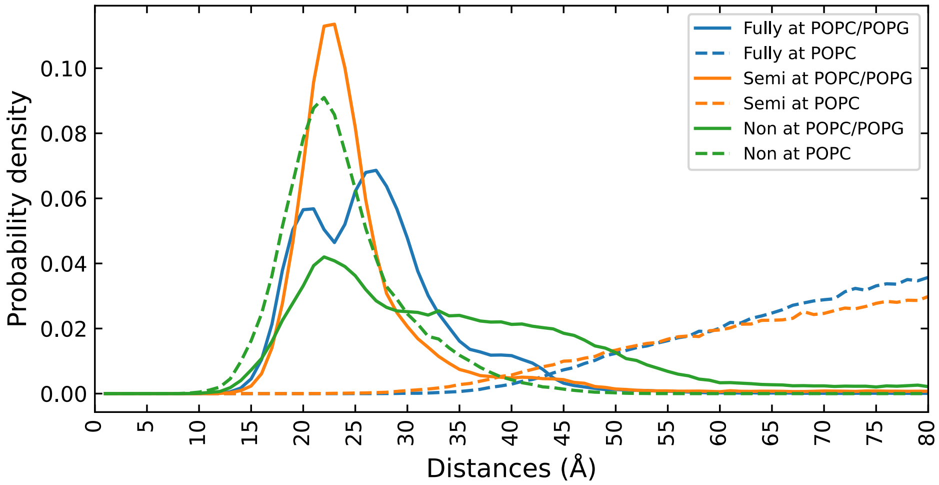

Figure 3.18: Distance-to-core distribution for PURE$_{G4}$-OEI$_{48}$ and POPC/POPG (solid) or POPC (dashed) membranes, at the three protonation levels.

In addition to the distances-to-core plots, the percentage of contacts (Fig.3.19) also reflects the observations made so far. In the case of the non-protonated state, there are almost twice as many contacts with the POPC membrane than with the POPC/POPG one, which may be explained by a higher tendency for the less charged nanoparticle to stay closer to the zwitterionic membrane. Still, the protonated nanoparticles all have more contacts with POPC/POPG than the non-protonated with either membrane. A similar relation between distance and contact can be inferred for both of the protonated states with the POPC/POPG membrane: the 38% more contacts of semi- over fully-protonated are in agreement with the distance distribution in Fig.3.18; and the larger error bar of the fully-protonated state in reflects its bimodal distances-to-core distribution.

3.9.3 System's ionic distribution

Another approach that can be of interest and help to understand the mode of action of this nanoparticle is to examine how its charge density can alter the ionic distribution around the membrane. Ions are essential to the correct metabolic function of all organism as they take part as being cofactors for enzymes, are involved into redox reactions and energetic pathways and also are crucial for the maintenance of the osmotic pressure of cells. Any limitation or imbalance of those micronutrients can drive delay in cell growth or even cause cell death [95]. Some important examples are Potassium as the main ion involved in the adaptation to osmolarity changes [96], Sodium involved in symporter and antiporter systems for different nutrients [97] and inorganic phosphate for ATP synthesis [98].

To understand the way that the ions of the system (Na^+ and Cl^-) are distributed at the proximity of the outer

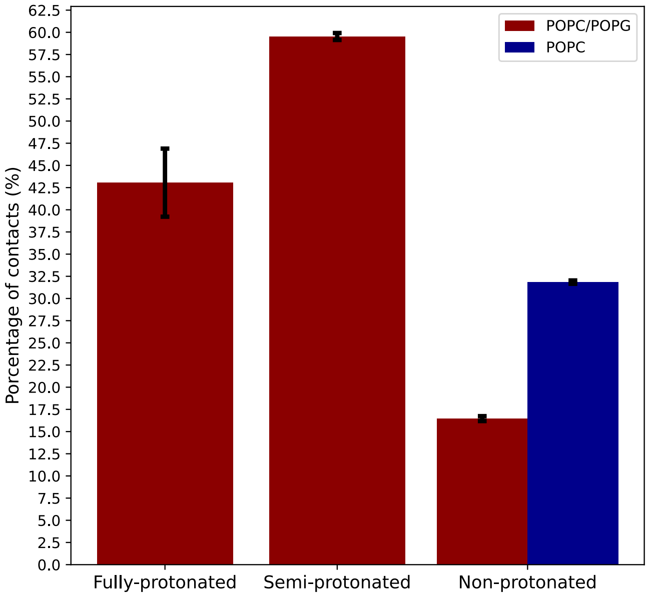

Figure 3.19: Percentage of a PURE$_{G4}$-OEI$_{48}$ nanoparticle's beads in contact with either POPC/POPG (red) or POPC (blue) membranes.

leaflet of both POPC/POPG and POPC membranes, their radial distribution function relative to the membrane was used and the results for the fully-protonated nanoparticle are shown in Fig. 3.20. This analysis was performed considering two distinct groups for each of the ions involved, divided into"close" and "far" groups, according to whether they are PO_4^- within 3 nm of the nanoparticle ("close") or not ("far"). From Figure 3.20 it is possible to notice that the Na^+ distribution changes a lot at the regions where the nanoparticle interacts with the membrane. The presence of this cation is reduced by around 3-fold in the vicinity of the membrane regions interacting with a nanoparticle, when compared to the regions that do not. Of course, this is explained by the repulsion generated by the positive charges from Na^+ and the nanoparticle, and the latter's effective substitution of membrane-adsorbed cations. The plot also shows that the Cl^- ions are dragged by the nanoparticle and their concentration increases at closer distances to the membrane when it interacts with the nanoparticle. In contrast to the ionic distribution around POPC/POPG membranes, Figure 3.20 shows that Na^+ concentration stays uniform along the whole extension of the POPC membrane, even when nanoparticle contacts do occur (both orange lines completely superimpose). The nanoparticle does not interact with non-ionic phospholipids, neither does it disturb their ionic shells. The high distribution of Cl^- at a distance far from the membrane simply reflects that the nanoparticle spends most of the time away from the membrane, and that it tends to aggregate negative charges around itself.

The semi-protonated nanoparticle displays a similar influence in the ionic distribution around both membranes (fig. A.1). At the interface with the POPC/POPG membrane, the presence of Na^+ is depleted 7-fold compared to regions without nanoparticle interaction, and the displacement of Cl^- towards the nanoparticle is very clear. The lack of charge in the non-protonated state makes the presence of the nanoparticle to have less to no influence in how both Na^+ and Cl^- are distributed within system (fig. A.2).

The capacity of certain dendrimers and polymeric nanoparticles to sequester ions has been previously in-

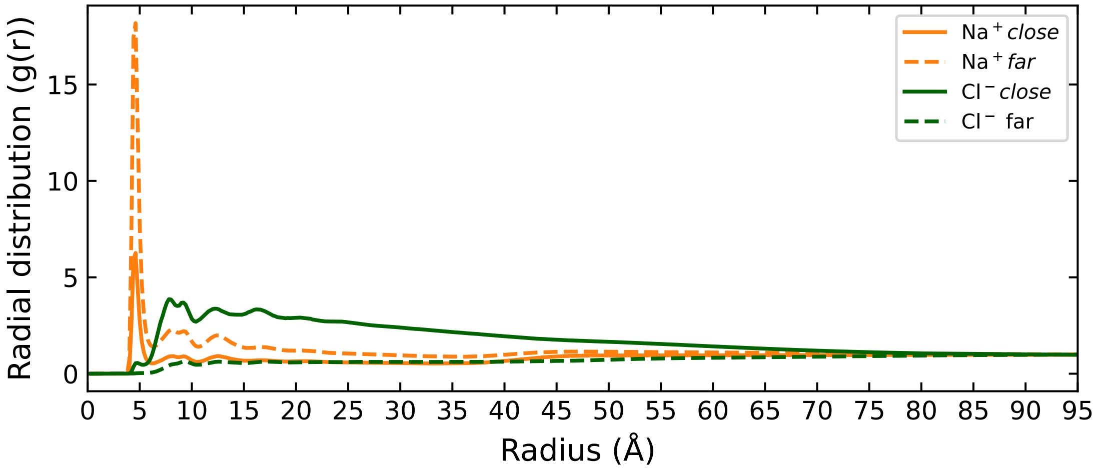

(a) Original nanoparticle at POPC/POPG

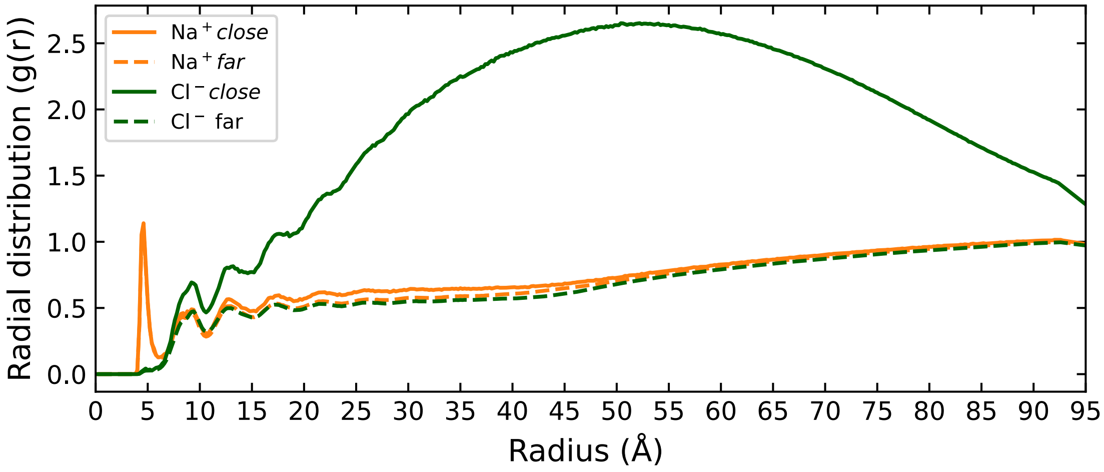

(b) Original nanoparticle at POPC

Figure 3.20: Radial distribution function of ions around outer leaflet of membranes under presence of fully-protonated PURE$_{G4}$-OEI$_{48}$. Note that in b) the Na$^+$ plots completely superimpose at distances below 7 Å, as do the plots for Cl$^-$.

vestigated. In early 2000s study, Majtyka and Kłos [99], using Monte Carlo simulations, demonstrated that for a positively charged dendrimer of fifth-generation the increase in the number of salt ions and the decrease of temperature resulting in encapsulation of anions with condensation at the terminal charged groups, with the penetration of anions being higher than cations. For poly(amidoamine) (PAMAM), one of the most studied dendrimers, the proximity of Cl^- ions to the dendrimer was shown to correlate with the pH of the environment, where an increase in pH caused a depletion of anions [100]. It has also been shown that fifth-generation PAMAM can incorporate phosphate ions into its structure [101] through hydrogen bonds with tertiary amines. The capacity of the dendrimer to complex with cations was also investigated: Shao et al. [102] presented a poly(acylthiourea)–poly(ethyleneglycol) co-dendrimer able to quench ${Cu_2}^+$ ions while Mazzitelli and Brodbelt [103] showed that PAMAM first-generation amine-terminated and second-generation hydroxyl-terminated dendrimers can complex Ag^+ with 1:1 stoichiometry.

With the property to interact with different types of anions, it is possible that one mode of action related to the antimicrobial ability of PURE_{G4}-OEI_{48} is to form a layer around the bacterial cell that will alter the concentration distribution of cations and anions and progressively disrupt ion-dependent functions, leading to cell death.

3.10 Proposed modifications

The simulations described so far show the potential of Molecular Dynamics in interpreting nanoparticle action. Here we extend it to screening the activity of new nanoparticles. Specifically, the building block philosophy and the larger timescales attainable with Martini make this force field a powerful tool in the screening of new compositions at the early stage of development.

With the knowledge acquired, the next step was to study possible modifications to the original PURE_{G4}-OEI_{48} that may increase its overall antimicrobial effects. The objective was to increase the hydrophobic interaction of the whole nanoparticle with the membrane by taking advantage of already known parameterized building block in Martini 3. Following this strategy, amino acid residues were suitable starting points for the development of modifications of the original nanoparticle. For this study, Leucine (Leu), Phenylalanine (Phe) and Tryptophan (Trp) were chosen for their side-chain hydrophobicity (from the Wimley–White whole residue hydrophobicity scales [104, 105]), and their different propensities for interfacial membrane interaction. Their atomistic structure and the Martini 3 bead representation are displayed in Figure 3.21:

A total of 48 amino acids residues were inserted between the dendrimer and the polymer chains, one per dendrimer–polymer link, forming a lipophilic layer. The bonds and angles parameters between AM beads from the dendrimer, the BB beads from amino acids residues and NT beads from OEI chains were drawn directly from the Martini 3 parameters for a random-coiled protein backbone and are described in table 3.8 below:

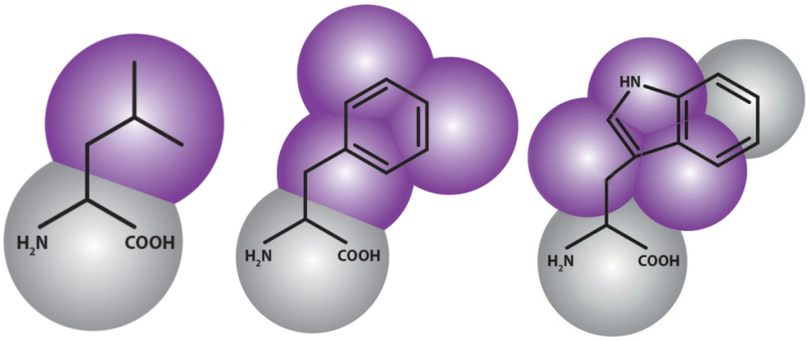

(a) Leucine. (b) Phenylalanine. (c) Tryptophan.

Figure 3.21: Coarse-grained representation of chosen amino acids. Adapted from [106].

Table 3.8: Martini 3 parameters for connection between dendrimer, amino acids and OEI chains. b_0 in nm, k_b in kJ·mol^{-1}·nm^{-2}, θ_0 in degrees and k_θ in kJ/mol.

Bond	b_0	k_b	Angle	$\theta 0$	k_θ
AM-BB / BB-NT	0.350	4000	AM-BB-NT	127	20

3.10.1 Structural analysis

Prior to analyzing whether any of the suggested modifications improve the nanoparticle's antimicrobial activity, we check dynamic behavior to understand if the alterations cause any significant changes. Table 3.9 shows the average values of R_g, **S** and Δ for all the variants produced:

Table 3.9: Comparison between the attributes of the original PURE$_{G4}$-OEI$_{48}$ and the suggested modifications.

Attribute		Fully-protonated		semi-protonated		Non-protonated	
		Dendrimer	Nanoparticle	Dendrimer	Nanoparticle	Dendrimer	Nanoparticle
$\langle R_g \rangle$	Orig	19.723 ± 0.622	30.338 ± 0.894	20.889 ± 0.530	29.524 ± 0.638	19.562 ± 0.805	26.043 ± 1.034
	Leu	20.006 ± 0.552	31.230 ± 0.949	21.166 ± 0.522	30.364 ± 0.640	19.666 ± 0.740	26.583 ± 0.944
	Phe	17.296 ± 0.722	27.853 ± 0.781	20.374 ± 0.648	28.931 ± 0.653	17.340 ± 0.837	23.464 ± 0.938
	Trp	18.476 ± 0.776	27.102 ± 1.039	20.208 ± 0.675	27.922 ± 0.679	17.616 ± 0.827	23.380 ± 0.920
$\langle \mathbf{S} \rangle$	Orig	0.022 ± 0.031	0.006 ± 0.014	-0.004 ± 0.018	0.000 ± 0.007	0.008 ± 0.040	0.006 ± 0.022
	Leu	-0.002 ± 0.029	0.004 ± 0.012	-0.007 ± 0.019	-0.000 ± 0.007	0.005 ± 0.037	0.005 ± 0.018
	Phe	0.012 ± 0.057	0.006 ± 0.013	0.005 ± 0.042	0.003 ± 0.014	0.032 ± 0.068	0.019 ± 0.041
	Trp	0.014 ± 0.041	0.006 ± 0.013	-0.008 ± 0.041	-0.001 ± 0.016	0.025 ± 0.057	0.015 ± 0.034
$\langle \Delta \rangle$	Orig	0.094 ± 0.039	0.039 ± 0.024	0.054 ± 0.025	0.026 ± 0.014	0.085 ± 0.041	0.053 ± 0.029
	Leu	0.070 ± 0.032	0.038 ± 0.021	0.057 ± 0.027	0.026 ± 0.015	0.081 ± 0.039	0.048 ± 0.026
	Phe	0.132 ± 0.036	0.039 ± 0.019	0.091 ± 0.042	0.043 ± 0.022	0.115 ± 0.055	0.079 ± 0.041
	Trp	0.125 ± 0.044	0.045 ± 0.027	0.091 ± 0.042	0.046 ± 0.024	0.106 ± 0.050	0.072 ± 0.037

In regard to the size, it was possible to notice that the phenylalanine and tryptophan modifications reduce the average values for both the dendrimer layer and for the whole particle at all protonation states. This may be explained by the relative size and presence of aromatic ring of those residues, which favors the occurrence of π stacking interactions and a small collapse of this lipophilic layer, countering the expansion of the nanoparticle as a whole. With leucine, its size and type of interaction do not seem to be strong enough to significantly affect R_g values, keeping the behavior like the one from the original nanoparticle.

In terms of shape and asphericity, again, the phenylalanine and tryptophan residues have more impact than leucine. Both increased the deviation of the shape to a more prolate configuration and increase its asphericity. However, the effect of polymer chain protonation still dominates, and amino acid contribution becomes more visible for non-protonated chains. In general, however, amino acid effects are small, probably because the nanoparticle can undergo large changes at its core without major implications at the overall size and shape.

Figure 3.22 displays the nanoparticle structure for all modifications, and aids in the interpretation of the observations in table 3.9, namely, the decrease in size according to the change in protonation and the more spherical shape for all semi-protonation states (Fig. 3.22b, 3.22e and 3.22h). With the polymer chains in the fully-protonated states (Fig. 3.22a, 3.22d and 3.22g), all amino acids become more visible to the medium, while for the other states, the amino acids are more buried into the core of the nanoparticle.

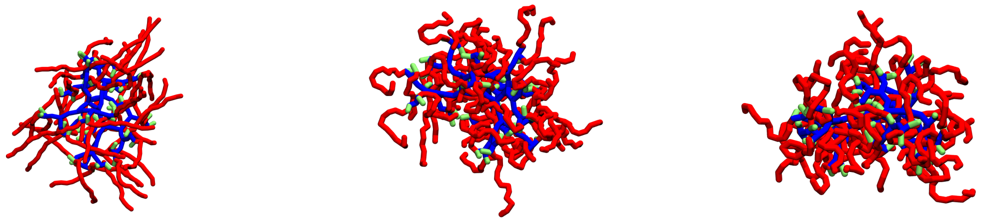

(a) Leu mod at fully-protonated state (b) Leu mod at semi-protonated state (c) Leu mod at non-protonated state

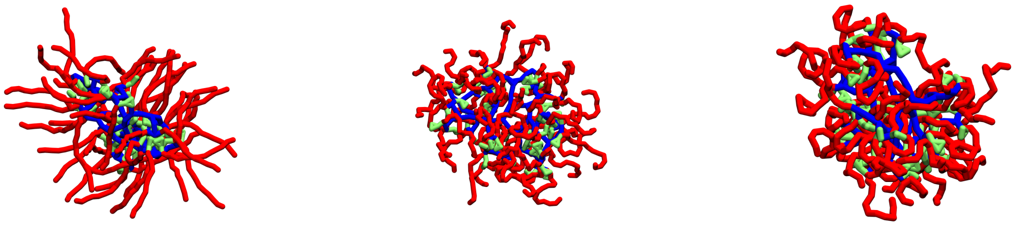

(d) Phe mod at fully-protonated state (e) Phe mod at semi-protonated state (f) Phe mod at non-protonated state

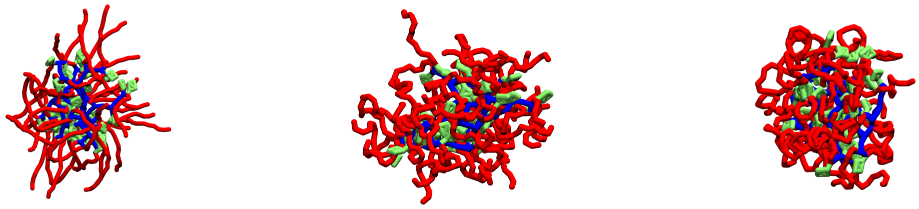

(g) Trp mod at fully-protonated state (h) Trp mod at semi-protonated state (i) Trp mod at non-protonated state

Figure 3.22: Structures for all modifications of PURE$_{G4}$-OEI$_{48}$, in all three different protonation states. Amino acids are represented in green color.

3.10.2 Membrane distance, contact and ionic distribution vs. original PURE$_{G4}$-OEI$_{48}$

Knowing that the distances and contacts plots may predict how the interactions with both membrane types take place, we check if there is any type of improvements or changes in the way that PURE$_{G4}$-OEI$_{48}$ responds to the chosen modifications. The following plots show the comparison between the original nanoparticle and all proposed modifications.

As expected, the non-protonated version of all modifications (fig. 3.23) does not display selectivity, following the same behavior as the original nanoparticle. In fact, analyzing the short distance region of the plot, it is possible to notice that all modifications have a deeper insertion than the original: all modifications have interactions as close as 8 Å from the center of the membranes, while the original nanoparticle only can get as close as around 12 Å. Also, deep membrane interactions are more frequent with the POPC membrane, probably due to a more favorable interaction geometry between the amino acids and the interface/tail regions of the membrane lipids.

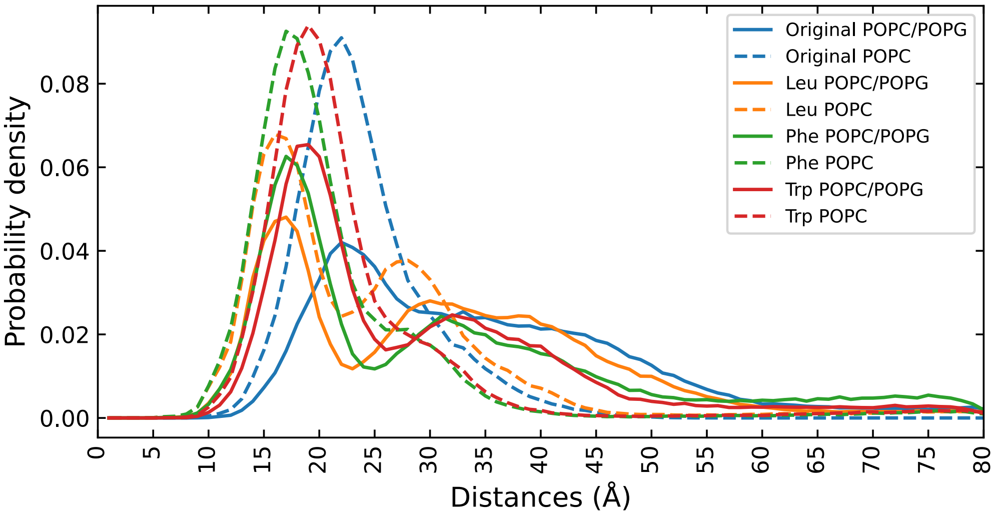

Figure 3.23: Distances probability of non-protonated nanoparticles at POPC/POPG (solid) and POPC(dashed) membranes.

From the fully-protonated plot (Fig. 3.24), one can see that while all modifications have a similar interaction with POPC/POPG membranes as the original nanoparticle, their distributions reach significantly lower distances, meaning that they can get closer to the center of the membrane. Interestingly, while leucine and tryptophan modifications do not significantly come to contact with the POPC membrane, the phenylalanine modification is able to interact with it (green dashed curve), going against what is expected for positively charge particles and its lack of selectivity toward neutral membranes. As an explanation to this action, it is possible that the hydrophobic character brought by the insertion of 48 phenylalanine residues can counter the effects of the charge and allows for the contact observed; its size and high hydrophobicity compared to the other two amino acids can also be factors behind this observation. Such increased membrane interaction extends to the POPC/POPG case, where the phenylalanine modification is able to penetrate much deeper than any other one, even when compared to the non-protonated cases.

When analyzing the semi-protonated state (fig. 3.25), membrane penetration is likewise increased relative to the original nanoparticle, with interactions for the leucine modification beginning at 9 Å and for tryptophan and phenylalanine around 11 Å (while for the original nanoparticles they start at 14 Å). Also, the first interaction peak becomes better defined relative to the fully protonated case, with maxima at 18, 19, 20 and 22.5 Å respectively for leucine, phenylalanine, tryptophan modifications and original nanoparticle. In contrast with what was observed in the fully-protonated state, the phenylalanine modification doesn't interact with the POPC membrane in this scenario.

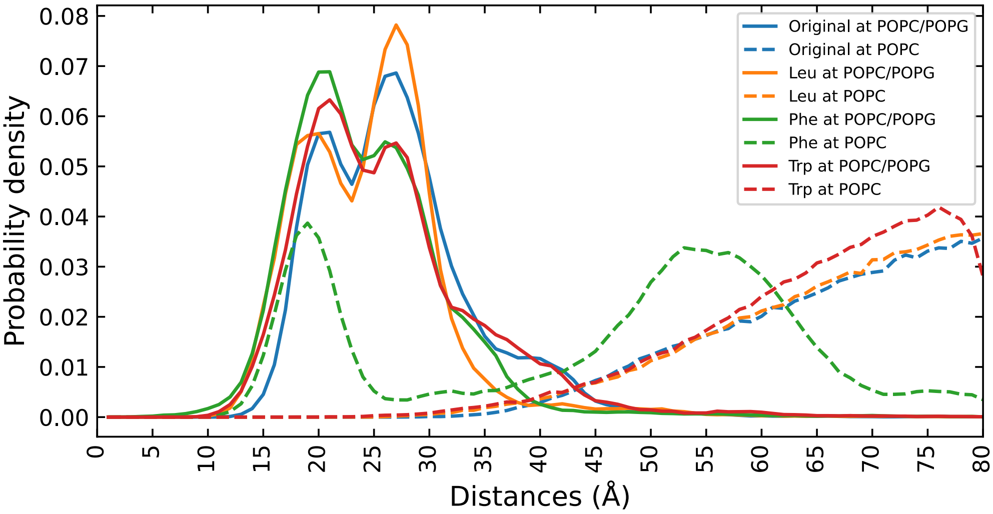

Figure 3.24: Distances probability of fully-protonated nanoparticles at POPC/POPG (solid) and POPC(dashed) membranes.

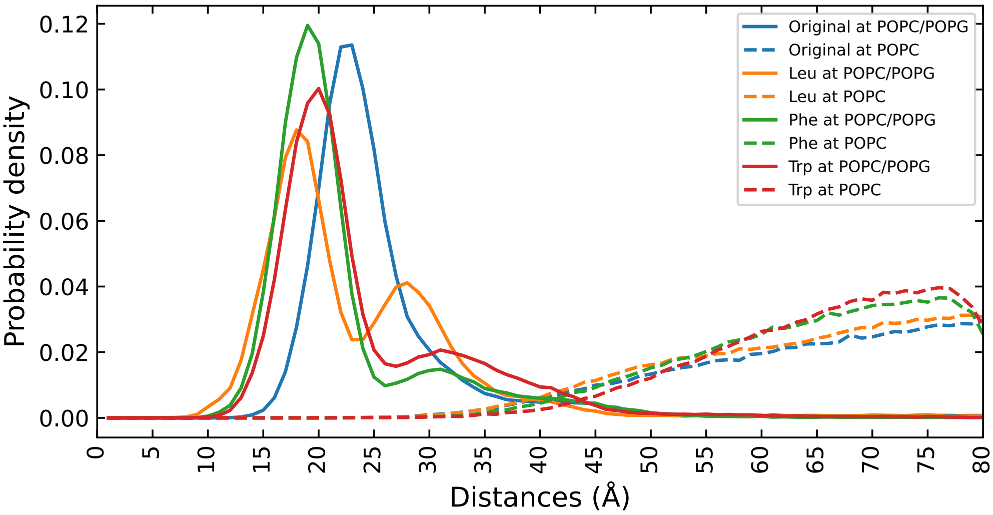

Figure 3.25: Distances probability of semi-protonated nanoparticles at POPC/POPG (solid) and POPC (dashed) membranes.

The contact plot (Fig. 3.26), again, is in agreement with the information acquired from the distances' distribution. For all nanoparticles, there is an increase in the total percentage of contacts when the protonation state goes from fully to semi protonation. The decrease in contacts for the non-protonated states shows the lower affinity for charged membranes, as already stated. In this aspect, a deeper interaction depth between the nanoparticle and a POPC/POPG membrane does not imply a higher number of contacts. The addition of the residues layer makes it harder for the dendrimer to enter in contact with any part of the membrane lipids, although the number of contacts is greater for the modifications that can get closer to the center of the membrane. In any case, care must be taken when interpreting these results as they will heavily depend on how long the nanoparticle diffuses before it interacts with the membrane.

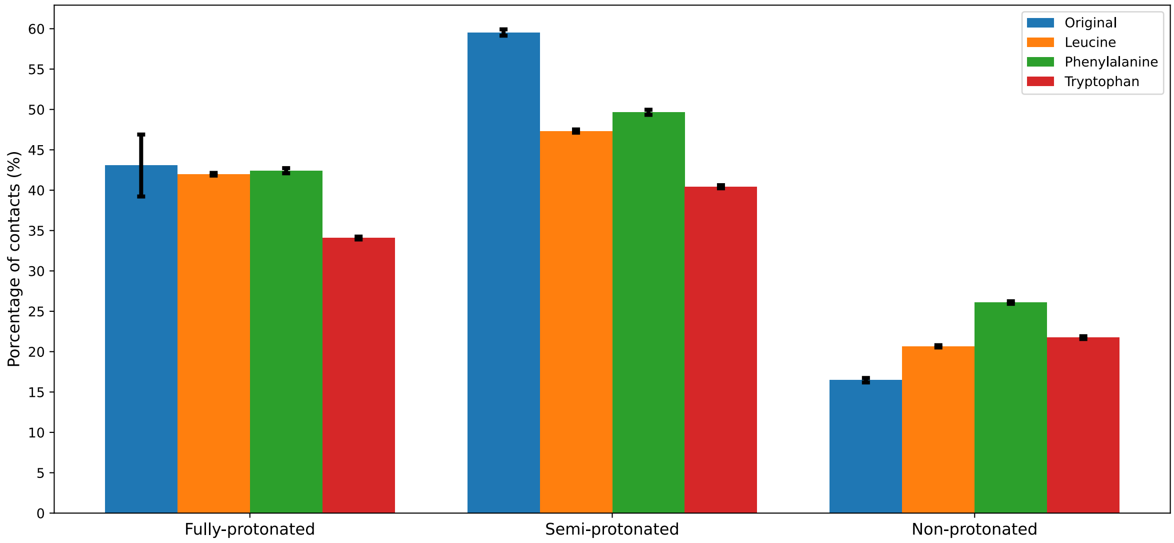

Figure 3.26: Percentage of contacts for all nanoparticle modifications and state of protonation at POPC/POPG membranes.

Continuing to explore the interactions in question, the visual inspection of the relevant trajectories come as another source of evidence from the analysis made so far. First, the mode of action for the fully-protonated phenylalanine modification among the two types of membrane can be observed in figure 3.27:

The overall charge density resulting from all polymer chains makes the interaction with POPC/POPG membrane to be quite similar to the one from the original nanoparticle. In this situation, it's possible to see that the amino acid moieties can pass between PO_4^- heads and better interact with the phospholipids' hydrophobic interface/tail region (Fig. 3.27a). This interaction may help to approximate the whole nanoparticle to the center of the bilayer and increase the tension of the cavity formed. In the scenario with the POPC membrane, the interaction is mainly ruled by the amino acids' residues. This visualization confirms that there is an equilibrium between the repulsion from the positives charges of the nanoparticle and the lipophilic affinity from amino acids. When the nanoparticle is able to get to a certain distance from the outer leaflet and expose the amino acids, it becomes anchored through the affinity of phenylalanine for the phospholipids (Fig. 3.27c and 3.27d). The prolate shape of the phenylalanine-modified nanoparticle leads to two possible interaction orientations (the upright stance seen in Fig. 3.27b and a horizontal one), explaining the two distance peaks in figure 3.24.

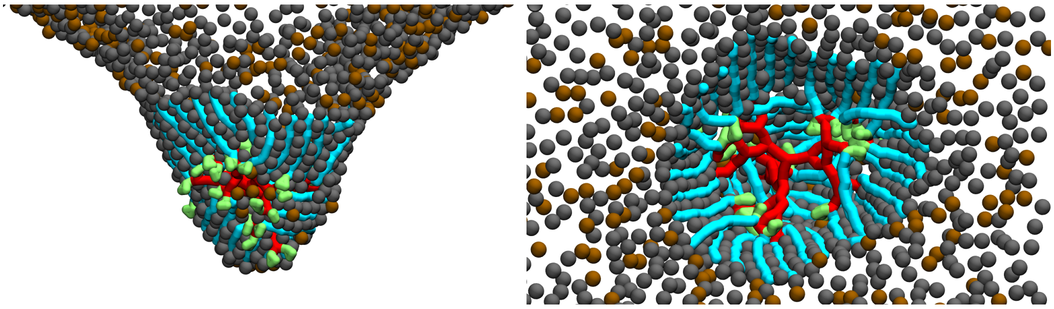

(a) Side view of interaction with POPC/POPG. (b) Top view of interaction with POPC/POPG.

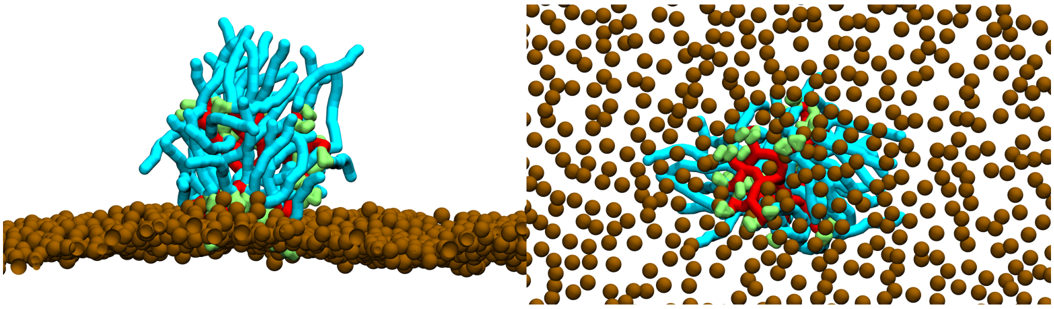

(c) Side view of interaction with POPC. (d) Bottom view of interaction with POPC.

Figure 3.27: Trajectory views of fully-protonated Phenylalanine mod PURE$_{G4}$-OEI$_{48}$ interaction with POPC/POPG and POPC membranes.

The interactions of the other two modifications, in the fully-protonated state, are presented in Figure 3.28. Both side views (Fig. 3.28a and 3.28c) show similar cavity formation as seen so far, although this effect is not as prominent for the tryptophan modification.

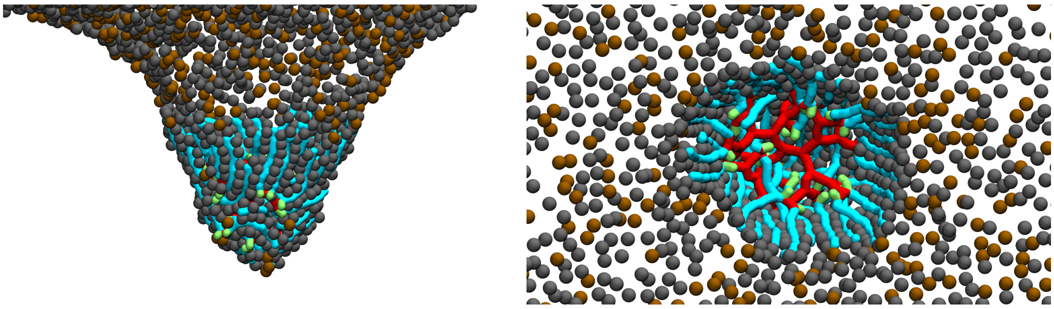

(a) Leucine mod side view interaction (b) Leucine mod top view interaction

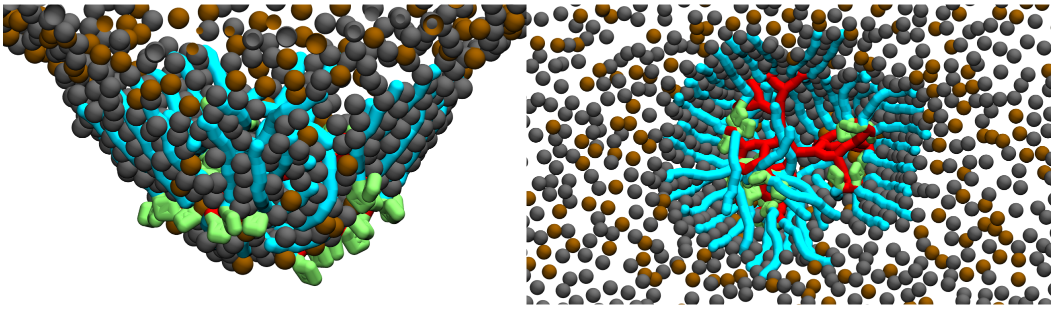

(c) Tryptophan mod side view interaction. (d) Tryptophan mod top view interaction.

Figure 3.28: Trajectory views of fully-protonated Leucine and Tryptophan mods PURE$_{G4}$-OEI$_{48}$ interaction with POPC/POPG membranes.

In contrast with the protonated state, the semi-protonated interaction of all modifications (Fig. 3.29) has significant deviations from the original one in that the formed cavity is not as deep. Here, cavity formation competes with a broader nanoparticle–membrane interaction due to increased amino acid solubility into the lipid tails, which does not become completed due to the anchoring of the positive charges at the membrane surface. From the interaction of the leucine modification (Fig. 3.29a) one can see that some parts of the dendrimer layer are able to pass the phosphate barrier. The same happens for the other two modifications, but to a lesser extent. From all the top views (fig. 3.29b, 3.29d and 3.29f) the number of residues that can interact at the same time with the membrane seems to be higher than in the previous state. This higher contribution of lipophilic groups seems to increase the proximity and may allow for stronger/different mechanisms of disruption.

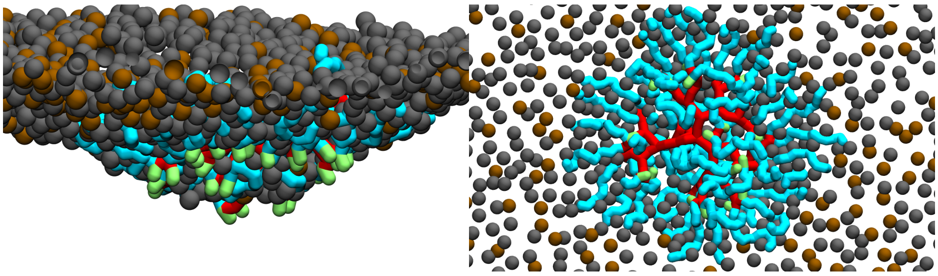

(a) Leucine mod side view interaction (b) Leucine mod top view interaction

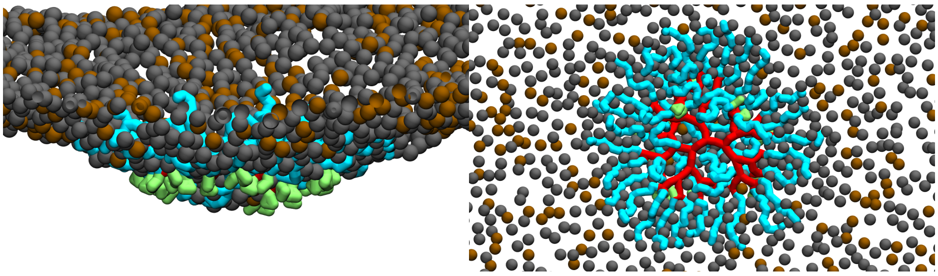

(c) Phenylalanine mod side view interaction. (d) Phenylalanine mod top view interaction.

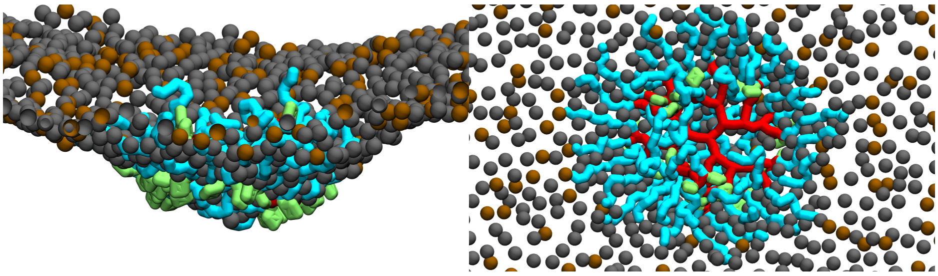

(e) Tryptophan mod side view interaction. (f) Tryptophan mod top view interaction.

Figure 3.29: Trajectory views of semi-protonated mods PURE$_{G4}$-OEI$_{48}$ interaction with POPC/POPG membranes.

Finally, the possible impact of the addition of amino acids on the ionic distribution of the system were investigated. The plots from Figures A.3, A.4 and A.5 demonstrate that the addition of the modifications has practically no influence at how ions distribute. For all the simulated scenarios, the protonation state still dictates the interaction with ions, closely following the same pattern displayed by the the original nanoparticle (Fig. 3.20, A.1 and A.2).

CHAPTER 4 - DISCUSSION

To determine the effects and mode of action of a novel therapeutic nanoparticle, several coarse-grained Molecular Dynamics assays against model of bilayer membranes were performed.

First, the nanoparticle in question - PURE$_{G4}$-OEI$_{48}$ - had to be modeled accordingly, and to do so it was divided into two different segments: the polyurea dendrimer and the oligo(ethylenimine) chains. Ethylenimine polymer has been extensively studied, mainly focused on its interaction with DNA/RNA [46, 71, 107] and its ability to serve as non-viral gene delivery systems [47]. Work has also been done in respect to its potential as antimicrobial agent [48, 50, 25] and recently some MD studies were also performed [84, 108, 71, 109]. However, due to the lack of specific atomistic FF parameters for the conditions desired, this work created a more refined model for linear OEI. This model considered three different protonation states and how the polymer chain behaves in a physiological salt concentration (150 nM of NaCl). The parameters of this model follow the recommended Martini 3 strategy to assign the bead type for each building block of the polymer based on chemical similarity and the bonded parameter were taken from an AA reference data. The necessary reference data was generated using amber99sb-ildn [72] with specific torsion parameters that we derived from a comprehensive body of basic *ab initio* characterization of three ethylenimine oligomers.

Since the beginning of the dihedral parameterization process at the atomistic level, results demonstrated the expected behavior, with higher protonations yielding more extended polymers. The overall quality of the parameters generated allowed for atomistic simulations that reflect the influence of both protonation and ionic strength, where statistical values for the average D_{ee} and R_g increase with protonation and decrease with the concentration of salt in the medium. This behavior is explained by the repulsion generated between charged amino groups from the backbone of the polymers chains and by the ions screening such interactions and reducing the repulsive effect. The results agree with observations made in previous MD studies [86, 109].

With a better suited AA topology, the Martini 3 model for the linear OEI chain could be built. The natural extended behavior of this polymeric chain led to unstable simulations when using the standard harmonic potentials. The use of a combined bending-torsion potential, proposed by Bulacu and Van Der Giessen[90], allowed a good representation of all dihedrals while keeping numerical stability without compromising the use of large timesteps, as is often the need when imposing torsion potentials in coarse-grain [90]. Indeed, in their parameterization Beu, Ailenei, and Costinaş[71] employed standard proper dihedral torsion potentials but had to sacrifice simulation velocity by using a time step twice smaller (10 fs instead of the regular 20 fs) than what is recommended when using Martini force fields.

Our CG model is able to faithfully reproduce the atomistic dynamics of the polymer under the extreme states of complete protonation and complete deprotonation, but disagrees with atomistic behavior when the chains are semi-protonated. This limitation of the CG model for this specific protonation state reflects the overall oversimplification of charge–charge interactions in Martini. It was also observed by Beu, Ailenei, and Costinaş [71], and shown by them to be mitigated by using a polarizable water model — which at the current time is still not available under the beta version of Martini 3. This opens up the opportunity to improve the derived coarse-grained topology after the release of the final version of Martini 3 and its polarizable water model.

The CG topology generated for the polyurea dendrimer was able to represent the overall shape and dynamics of the previously developed CHARMM model [110]. This indicates that the mapping choice along with the bead type assignment were properly done and fulfilled their objective to create the most suitable representation of this molecule. It is important to highlight that the used atomistic dataset was not simulated long enough to reach equilibrium of the dendrimer's dynamics. The structural dynamics of dendrimers have been previously investigated and their relaxation times can vary from a few hundred picoseconds, in the case of different generations of PAMAM [111], to more than 10 ns, in the case of poly-L-Lysine based dendrimers [112]. Also, the structural dynamics evolve differently within the dendrimer, with the core layer presenting slower dynamic compared to the periphery [113]. These factors may have introduced some bias in the CG parameters, specifically the torsion potentials, which may have a more defined behavior in longer atomistic simulations.

The assays performed against bilayer membrane models allowed us to better understand what are the likely elements that lead to the antimicrobial activity and selectivity of the nanoparticle and what may be potential points of improvement on its design. As expected, the positive net charge is crucial for the selectivity towards anionic phospholipid bilayers, where both the fully- and semi- protonated nanoparticles strongly interact with the POPC/POPG model. However, if the charge density is too high, further contact and penetration can not be achieved, as the comparison from figure 3.17 demonstrated. This goes in agreement with the main attributes found in AMPs [28] and their ability to induce curvature as the primary way to compromise barrier function [92]. Also, the ability to interfere with the ionic distribution and displace cations and anions around the system, can explain an added antimicrobial mechanism by means of disruption of ion dependent functions, and possibly even the membrane potential.

From the insights acquired from the simulations of the original nanoparticle, modifications were proposed with the objective of improving its attributes, mainly the ratio of hydrophobic components. With that, three amino acids with different hydrophobicity were incorporated in a layer between the dendrimer and the polymer chains, aiming at a deeper interaction with the membrane. The results showed that all proposed modifications do indeed average a closer distance to the center of the membrane than the original, indicating a better penetration. From all proposed modifications, the phenylalanine one was the only to show loss of selectivity for POPC/POPG membranes. The fact that it is the amino acid residue with highest hydrophobicity shows the importance of a well-balanced ratio to to the selectivity.

As a potential improvement to the original therapeutic nanoparticle, the leucine modification shows promising results, as it was able to display a closer distance to the center of the membrane than the tryptophan one, without impairing the desired selectivity as in the case of the phenylalanine modification.

CHAPTER 5 - CONCLUSIONS

The desire to better understand how therapeutic nanoparticles, designed from the principles behind the antimicrobial activity of AMPs, act against bacteria drove the development of this study and the use Molecular Dynamics as a powerful tool in the design of novel antibiotics molecules.

The ability to perform large scale studies, either in time and/or system size, favors the choice of a coarse-grained approach instead of an all-atom one. The Martini force field, being the most popular CG model to date and having a precise behavior in regard to lipid interaction becomes the most suitable choice. With the upcoming release of an updated version of this FF, Martini 3 has the potential to provide more refined and accurate models without the loss of its intrinsic low simulation cost.

The whole parameterization process expanded for the linear poly(ethylenimine) shows the importance of having a solid theoretical background to support the model created. The ability to investigate how this specific polymer chain behaves in different scenarios, mainly those that approach the conditions of their potential applications, helps demonstrate the strength of using MD simulations to screen multiple options and conditions prior laborious or costly experimental work is done. Here we were able to observe how different protonation states and the presence of ionic strength can impact the polymer's structural dynamics — including those of the linear OEI chain, of the polyurea dendrimer and of the assembled nanoparticle models. The nanoparticles were then simulated to infer how they interact with, and potentially disrupt, model membranes. These computational findings, including the proposal of increased activity modifications, lay the foundation for future experimental studies which can not only complement and validate our work by hopefully producing more potential therapeutic nanoparticles, but can also help in creating more refined and realistic molecular models.

The analysis made in this project contributed to the overall understanding of how custom designed nanoparticles interact with distinct types of membrane models. For a therapeutic nanoparticle to have an optimal antimicrobial effect, it requires a tight balance between the density of its overall positive charge and the extent of its hydrophobic groups. The results show that the positive net charge is crucial in dictating selectivity, allowing for the interaction with anionic phospholipids but, without a significant amount of hydrophobic interaction, the nanoparticle can't break the electrostatic barrier imposed by the membrane and diffuse into or disrupt the phospholipid bilayer. This work was able to improve the balance between charge and hydrophobicity by the insertion of leucine amino acids which results in improved interaction than the ones from the original nanoparticle.

In all, the work developed here is an important first step in search for insight into the killing mechanism of these types of nanoparticles. Further theoretical works can expand from this starting point, where new modifications (*e.g.* insertion of hydrophobic moieties at different regions of the polymer or dendrimer structure) and more robust bacterial membrane models can be tested and lead the design of polymeric nanoparticles. Likewise, as previously mentioned, future experimental studies can use this work as a guide, which can facilitate and assist at the production of more safe and effective therapeutic nanoparticles.

REFERENCES

[1] Merriam-Webster. *Antibiotic*. 2020. URL: `https://www.merriam-webster.com/dictionary/antibiotic` (visited on 01/18/2020).

[2] M. C. Maranan et al. “Antimicrobial resistance in staphylococci. Epidemiology, molecular mechanisms, and clinical relevance”. In: *Infectious Disease Clinics of North America* 11.4 (Dec. 1997), pp. 813–849. ISSN: 08915520. DOI: `10.1016/S0891-5520(05)70392-5`.

[3] Stuart B. Levy and Stuart B. Levy. “From Tragedy the Antibiotic Age is Born”. In: *The Antibiotic Paradox*. Springer US, 1992, pp. 1–12. DOI: `10.1007/978-1-4899-6042-9_1`.

[4] Rustam I. Aminov. “A Brief History of the Antibiotic Era: Lessons Learned and Challenges for the Future”. In: *Frontiers in Microbiology* 1.DEC (Dec. 2010), p. 134. ISSN: 1664-302X. DOI: `10.3389/fmicb.2010.00134`.

[5] Everett J. Bassett et al. “Tetracycline-labeled human bone from ancient Sudanese Nubia (A.D. 350)”. In: *Science* 209.4464 (Sept. 1980), pp. 1532–1534. ISSN: 00368075. DOI: `10.1126/science.7001623`.

[6] Megan Cook, El Molto, and C. Anderson. “Fluorochrome labelling in roman period skeletons from dakhleh oasis, Egypt”. In: *American Journal of Physical Anthropology* 80.2 (Oct. 1989), pp. 137–143. ISSN: 0002-9483. DOI: `10.1002/ajpa.1330800202`.

[7] Sojib Bin Zaman et al. “A Review on Antibiotic Resistance: Alarm Bells are Ringing”. In: *Cureus* 9.6 (June 2017). ISSN: 2168-8184. DOI: `10.7759/cureus.1403`.

[8] Ranjana Chopra et al. “The influence of pellet shape and surface properties on the drug release from uncoated and coated pellets”. In: *International Journal of Pharmaceutics* 239.1-2 (June 2002), pp. 171–178. ISSN: 03785173. DOI: `10.1016/S0378-5173(02)00104-7`.

[9] Ramanan Laxminarayan and Gardner M. Brown. “Economics of antibiotic resistance: A theory of optimal use”. In: *Journal of Environmental Economics and Management* 42.2 (Sept. 2001), pp. 183–206. ISSN: 00950696. DOI: `10.1006/jeem.2000.1156`.

[10] Herman Goossens et al. “Outpatient antibiotic use in Europe and association with resistance: a cross-national database study”. In: *The Lancet* 365.9459 (Feb. 2005), pp. 579–587. ISSN: 01406736. DOI: `10.1016/s0140-6736(05)17907-0`.

[11] Charles W. Hoge et al. “Trends in Antibiotic Resistance Among Diarrheal Pathogens Isolated in Thailand Over 15 Years”. In: *Clinical Infectious Diseases* 26.2 (Feb. 1998), pp. 341–345. ISSN: 1058-4838. DOI: `10.1086/516303`.

[12] Ahmed Ehsanur Rahman et al. “Managing Neonatal and Early Childhood Syndromic Sepsis in Sub-District Hospitals in Resource Poor Settings: Improvement in Quality of Care through Introduction of a Package of Interventions in Rural Bangladesh”. In: *PLOS ONE* 12.1 (Jan. 2017). Ed. by Umberto Simeoni, e0170267. ISSN: 1932-6203. DOI: `10.1371/journal.pone.0170267`.

[13] Thomas D. Gootz. “Discovery and development of new antimicrobial agents”. In: *Clinical Microbiology Reviews* 3.1 (Jan. 1990), pp. 13–31. ISSN: 08938512. DOI: `10.1128/CMR.3.1.13`.

[14] M. Patricia Jevons. *“Celbenin” -resistant Staphylococci*. Jan. 1961. DOI: `10.1136/bmj.1.5219.124-a`.

[15] P. C. Appelbaum. *The emergence of vancomycin-intermediate and vancomycin-resistant Staphylococcus aureus*. Jan. 2006. DOI: `10.1111/j.1469-0691.2006.01344.x`.

[16] Ram H. Dahal and Dhiraj K. Chaudhary. “Microbial Infections and Antimicrobial Resistance in Nepal: Current Trends and Recommendations”. In: *The Open Microbiology Journal* 12.1 (Aug. 2018), pp. 230–242. ISSN: 1874-2858. DOI: `10.2174/1874285801812010230`.

[17] C Lee Ventola. “The antibiotic resistance crisis: causes and threats.” In: *P & T journal* 40.4 (2015), pp. 277–83. ISSN: 1052-1372. DOI: `Article`. arXiv: `/ehis.ebscohost.com/ [http:]`.

[18] Dalila Mil-homens et al. “KPC- and OXA-48-producing Klebsiella pneumoniae clinical isolates : In vitro virulence assessment in Galleria mellonella and potential therapeutics by polycationic oligoethyleneimine”. In: (2020), pp. 1–13.

[19] Calvin M. Kunin. “Book Review The Antibiotic Paradox: How Miracle Drugs Are Destroying the Miracle By Stuart B. Levy. 279 pp., illustrated. New York, Plenum, 1992. $24.95. 0-306-44331-7”. In: *New England Journal of Medicine* 328.24 (June 1993), pp. 1792–1792. ISSN: 0028-4793. DOI: `10.1056/nejm199306173282418`.

[20] Scott A. McEwen and Paula J. Fedorka□Cray. “Antimicrobial Use and Resistance in Animals”. In: *Clinical Infectious Diseases* 34.s3 (June 2002), S93–S106. ISSN: 1058-4838. DOI: `10.1086/340246`.

[21] Javier Garau et al. “Emergence and dissemination of quinolone-resistant Escherichia coli in the community”. In: *Antimicrobial Agents and Chemotherapy* 43.11 (Nov. 1999), pp. 2736–2741. ISSN: 00664804. DOI: `10.1128/aac.43.11.2736`.

[22] Zhe Wang and Guangshun Wang. “APD: The antimicrobial peptide database”. In: *Nucleic Acids Research* 32.DATABASE ISS. (Jan. 2004), pp. D590–D592. ISSN: 03051048. DOI: `10.1093/nar/gkh025`.

[23] World Economic Forum. *Global Risks 2013 Eighth Edition An Initiative of the Risk Response Network Insight Report*. Tech. rep. 2013.

[24] World Health Organization. *Global Action Plan on Antimicrobial Resistance*. Tech. rep. 2015.

[25] Katherine A. Gibney et al. “Poly(ethylene imine)s as antimicrobial agents with selective activity”. In: *Macromolecular Bioscience* 12.9 (Sept. 2012), pp. 1279–1289. ISSN: 16165187. DOI: `10.1002/mabi.201200052`.

[26] Cansu Ergene, Kazuma Yasuhara, and Edmund F. Palermo. *Biomimetic antimicrobial polymers: Recent advances in molecular design*. May 2018. DOI: `10.1039/c8py00012c`.

[27] Guangshun Wang, Xia Li, and Zhe Wang. "APD2: The updated antimicrobial peptide database and its application in peptide design". In: *Nucleic Acids Research* 37.SUPPL. 1 (Jan. 2009), pp. 933–937. ISSN: 03051048. DOI: `10.1093/nar/gkn823`.

[28] Guangshun Wang, Xia Li, and Zhe Wang. "APD3: The antimicrobial peptide database as a tool for research and education". In: *Nucleic Acids Research* 44.D1 (Jan. 2016), pp. D1087–D1093. ISSN: 13624962. DOI: `10.1093/nar/gkv1278`.

[29] Emilie A. Porter, Bernard Weisblum, and Samuel H. Gellman. "Mimicry of host-defense peptides by unnatural oligomers: Antimicrobial β-peptides". In: *Journal of the American Chemical Society* 124.25 (June 2002), pp. 7324–7330. ISSN: 00027863. DOI: `10.1021/ja0260871`.

[30] Yun Lan et al. "Cationic amphipathic D-enantiomeric antimicrobial peptides with in vitro and ex vivo activity against drug-resistant Mycobacterium tuberculosis". In: *Tuberculosis* 94.6 (Dec. 2014), pp. 678–689. ISSN: 1873281X. DOI: `10.1016/j.tube.2014.08.001`.

[31] El Rafaie Kenawy, S. D. Worley, and Roy Broughton. *The chemistry and applications of antimicrobial polymers: A state-of-the-art review*. May 2007. DOI: `10.1021/bm061150q`.

[32] T. Ikeda, S. Tazuke, and Y. Suzuki. "Biologically Active Polycations : Synthesis and Antimicrobial Activity of Poly(trialkyl vinylbenzyl ammonium chloride)s". In: *Makromol. Chem.* 185.5 (May 1984), pp. 869–876. ISSN: 0025-116X. DOI: `10.1002/macp.1984.021850503`.

[33] D. Liu and W. F. DeGrado. "De novo design, synthesis, and characterization of antimicrobial β-peptides". In: *Journal of the American Chemical Society* 123.31 (2001), pp. 7553–7559. ISSN: 00027863. DOI: `10.1021/ja0107475`.

[34] Margaret A. Schmitt, Bernard Weisblum, and Samuel H. Gellman. "Unexpected relationships between structure and function in α,β-peptides: Antimicrobial foldamers with heterogeneous backbones". In: *Journal of the American Chemical Society* 126.22 (June 2004), pp. 6848–6849. ISSN: 00027863. DOI: `10.1021/ja048546z`.

[35] Yun Mi Song et al. "Cell selectivity and mechanism of action of antimicrobial model peptides containing peptoid residues". In: *Biochemistry* 44.36 (Sept. 2005), pp. 12094–12106. ISSN: 00062960. DOI: `10.1021/bi050765p`.

[36] Kenichi Kuroda, Gregory A. Caputo, and William F. DeGrado. "The role of hydrophobicity in the antimicrobial and hemolytic activities of polymethacrylate derivatives". In: *Chemistry - A European Journal* 15.5 (Jan. 2009), pp. 1123–1133. ISSN: 09476539. DOI: `10.1002/chem.200801523`.

[37] M. Firat Ilker et al. "Tuning the hemolytic and antibacterial activities of amphiphilic polynorbornene derivatives". In: *Journal of the American Chemical Society* 126.48 (Dec. 2004), pp. 15870–15875. ISSN: 00027863. DOI: `10.1021/ja045664d`.

[38] Runhui Liu et al. “Structure-activity relationships among antifungal nylon-3 polymers: Identification of materials active against drug-resistant strains of Candida albicans”. In: *Journal of the American Chemical Society* 136.11 (Mar. 2014), pp. 4333–4342. ISSN: 15205126. DOI: `10.1021/ja500036r`.

[39] Brendan P. Mowery et al. “Mimicry of antimicrobial host-defense peptides by random copolymers”. In: *Journal of the American Chemical Society* 129.50 (Dec. 2007), pp. 15474–15476. ISSN: 00027863. DOI: `10.1021/ja077288d`.

[40] Edmund F. Palermo et al. “Role of cationic group structure in membrane binding and disruption by amphiphilic copolymers”. In: *Journal of Physical Chemistry B* 115.2 (Jan. 2011), pp. 366–375. ISSN: 15205207. DOI: `10.1021/jp1083357`.

[41] Marie Paule Lefranc et al. *IMGT, the international ImMunoGeneTics database*. Jan. 1999. DOI: `10.1093/nar/27.1.209`.

[42] Edmund F. Palermo and Kenichi Kuroda. “Chemical structure of cationic groups in amphiphilic polymethacrylates modulates the antimicrobial and hemolytic activities”. In: *Biomacromolecules* 10.6 (June 2009), pp. 1416–1428. ISSN: 15257797. DOI: `10.1021/bm900044x`.

[43] Zoha M. Al-Badri et al. “Investigating the effect of increasing charge density on the hemolytic activity of synthetic antimicrobial polymers”. In: *Biomacromolecules* 9.10 (Oct. 2008), pp. 2805–2810. ISSN: 15257797. DOI: `10.1021/bm800569x`.

[44] Katherine E.S. Locock et al. “Guanylated polymethacrylates: A class of potent antimicrobial polymers with low hemolytic activity”. In: *Biomacromolecules* 14.11 (Nov. 2013), pp. 4021–4031. ISSN: 15257797. DOI: `10.1021/bm401128r`.

[45] Sarah E. Exley et al. “Antimicrobial Peptide Mimicking Primary Amine and Guanidine Containing Methacrylamide Copolymers Prepared by Raft Polymerization”. In: *Biomacromolecules* 16.12 (Dec. 2015), pp. 3845–3852. ISSN: 15264602. DOI: `10.1021/acs.biomac.5b01162`.

[46] Blandine Brissault et al. “Synthesis of linear polyethylenimine derivatives for DNA transfection”. In: *Bioconjugate Chemistry* 14.3 (May 2003), pp. 581–587. ISSN: 10431802. DOI: `10.1021/bc0200529`.

[47] Sangram Keshari Samal et al. “Cationic polymers and their therapeutic potential”. In: *Chemical Society Reviews* 41.21 (Oct. 2012), pp. 7147–7194. ISSN: 14604744. DOI: `10.1039/c2cs35094g`.

[48] Jian Lin et al. “Bactericidal properties of flat surfaces and nanoparticles derivatized with alkylated polyethylenimines”. In: *Biotechnology Progress* 18.5 (Jan. 2002), pp. 1082–1086. ISSN: 87567938. DOI: `10.1021/bp025597w`.

[49] Ilkka M. Helander et al. “Polyethyleneimine is an effective permeabilizer of Gram-negative bacteria”. In: *Microbiology* 143.10 (Oct. 1997), pp. 3193–3199. ISSN: 13500872. DOI: `10.1099/00221287-143-10-3193`.

[50] Nebojša M. Milović et al. “Immobilized N-alkylated polyethylenimine avidly kills bacteria by rupturing cell membranes with no resistance developed”. In: *Biotechnology and Bioengineering* 90.6 (June 2005), pp. 715–722. ISSN: 00063592. DOI: `10.1002/bit.20454`.

[51] Mayandi Venkatesh et al. “Antimicrobial activity and cell selectivity of synthetic and biosynthetic cationic polymers”. In: *Antimicrobial Agents and Chemotherapy* 61.10 (2017). ISSN: 10986596. DOI: `10.1128/AAC.00469-17`.

[52] Maral Aminpour, Carlo Montemagno, and Jack A. Tuszynski. “An Overview of Molecular Modeling for Drug Discovery with Specific Illustrative Examples of Applications”. In: *Molecules* 24.9 (Apr. 2019), p. 1693. ISSN: 1420-3049. DOI: `10.3390/molecules24091693`.

[53] Martin Karplus and J. Andrew McCammon. *Molecular dynamics simulations of biomolecules*. 2002. DOI: `10.1038/nsb0902-646`.

[54] B. J. Alder and T. E. Wainwright. *Phase transition for a hard sphere system*. Nov. 1957. DOI: `10.1063/1.1743957`.

[55] Romelia Salomon-Ferrer et al. “Routine microsecond molecular dynamics simulations with AMBER on GPUs. 2. Explicit solvent particle mesh ewald”. In: *Journal of Chemical Theory and Computation* 9.9 (Sept. 2013), pp. 3878–3888. ISSN: 15499618. DOI: `10.1021/ct400314y`.

[56] Scott A. Hollingsworth and Ron O. Dror. *Molecular Dynamics Simulation for All*. Sept. 2018. DOI: `10.1016/j.neuron.2018.08.011`.

[57] John E. Stone et al. “Evaluation of emerging energy-efficient heterogeneous computing platforms for biomolecular and cellular simulation workloads”. In: *Proceedings - 2016 IEEE 30th International Parallel and Distributed Processing Symposium, IPDPS 2016*. Institute of Electrical and Electronics Engineers Inc., July 2016, pp. 89–100. ISBN: 9781509021406. DOI: `10.1109/IPDPSW.2016.130`.

[58] M.J. Abraham et al. “GROMACS User Manual version 2018”. In: *GROMACS User Manual* (2018).

[59] Siewert J. Marrink et al. “The MARTINI force field: Coarse grained model for biomolecular simulations”. In: *Journal of Physical Chemistry B* 111.27 (July 2007), pp. 7812–7824. ISSN: 15206106. DOI: `10.1021/jp071097f`.

[60] Nidhi Singh and Wenjin Li. “Recent Advances in Coarse-Grained Models for Biomolecules and Their Applications”. In: *International Journal of Molecular Sciences* 20.15 (Aug. 2019), p. 3774. ISSN: 1422-0067. DOI: `10.3390/ijms20153774`.

[61] Alexander J. Pak and Gregory A. Voth. *Advances in coarse-grained modeling of macromolecular complexes*. Oct. 2018. DOI: `10.1016/j.sbi.2018.11.005`.

[62] MARTINI Group. *Introduction to Martini*. 2019. URL: `http://cgmartini.nl/index.php/about` (visited on 01/30/2020).

[63] Tatsuki Negami, Kentaro Shimizu, and Tohru Terada. “Coarse-grained molecular dynamics simulations of protein-ligand binding”. In: *Journal of Computational Chemistry* 35.25 (Sept. 2014), pp. 1835–1845. ISSN: 01928651. DOI: `10.1002/jcc.23693`.

[64] Yan Lu and Freddie Salsbury. “Recapturing the Correlated Motions of Protein Using Coarse- Grained Models”. In: *Protein & Peptide Letters* 22.7 (June 2015), pp. 654–659. ISSN: 09298665. DOI: `10.2174/0929866522666150511150332`.

[65] Bartholomé Delort et al. “Coarse-Grained Prediction of Peptide Binding to G-Protein Coupled Receptors”. In: *Journal of Chemical Information and Modeling* 57.3 (Mar. 2017), pp. 562–571. ISSN: 15205142. DOI: `10.1021/acs.jcim.6b00503`.

[66] Naresh Thota and Jianwen Jiang. “Self-assembly of amphiphilic peptide (AF)6H5K 15 derivatives: Roles of hydrophilic and hydrophobic residues”. In: *Journal of Physical Chemistry B* 118.10 (Mar. 2014), pp. 2683–2692. ISSN: 15205207. DOI: `10.1021/jp500406p`.

[67] Toru Ekimoto and Mitsunori Ikeguchi. *Multiscale molecular dynamics simulations of rotary motor proteins*. Apr. 2018. DOI: `10.1007/s12551-017-0373-4`.

[68] MARTINI Group. *Martini 3 open-beta*. URL: `http://cgmartini.nl/index.php/martini3beta` (visited on 11/23/2020).

[69] Rita B. Restani et al. “Biocompatible polyurea dendrimers with pH-dependent fluorescence”. In: *Angewandte Chemie - International Edition* 51.21 (May 2012), pp. 5162–5165. ISSN: 14337851. DOI: `10.1002/anie.201200362`.

[70] Helgi I. Ingólfsson et al. “Lipid organization of the plasma membrane”. In: *Journal of the American Chemical Society* 136.41 (Oct. 2014), pp. 14554–14559. ISSN: 15205126. DOI: `10.1021/ja507832e`.

[71] Titus Adrian Beu, Andrada□Elena Ailenei, and Răzvan□Ioan Costinaş. “Martini Force Field for Protonated Polyethyleneimine”. In: *Journal of Computational Chemistry* 41.4 (Feb. 2020), pp. 349–361. ISSN: 0192-8651. DOI: `10.1002/jcc.26110`.

[72] Kresten Lindorff-Larsen et al. “Improved side-chain torsion potentials for the Amber ff99SB protein force field”. In: *Proteins: Structure, Function and Bioinformatics* 78.8 (June 2010), pp. 1950–1958. ISSN: 08873585. DOI: `10.1002/prot.22711`.

[73] D.A. Case et al. *Amber 2020*. Tech. rep. San Francisco: University of California, 2020.

[74] Bryan Leland et al. *AMBER ADVANCED TUTORIALS TUTORIAL A1*. URL: `https://ambermd.org/tutorials/advanced/tutorial1/section1.htm` (visited on 08/24/2020).

[75] James C. Phillips et al. *Scalable molecular dynamics with NAMD*. 2005. DOI: `10.1002/jcc.20289`.

[76] K. Vanommeslaeghe et al. “CHARMM general force field: A force field for drug-like molecules compatible with the CHARMM all-atom additive biological force fields”. In: *Journal of Computational Chemistry* 31.4 (Mar. 2010), pp. 671–690. ISSN: 01928651. DOI: `10.1002/jcc.21367`.

[77] K. Vanommeslaeghe and A. D. MacKerell. “Automation of the CHARMM general force field (CGenFF) I: Bond perception and atom typing”. In: *Journal of Chemical Information and Modeling* 52.12 (Dec. 2012), pp. 3144–3154. ISSN: 15499596. DOI: `10.1021/ci300363c`.

[78] K. Vanommeslaeghe, E. Prabhu Raman, and A. D. MacKerell. “Automation of the CHARMM General Force Field (CGenFF) II: Assignment of Bonded Parameters and Partial Atomic Charges”. In: *Journal of Chemical Information and Modeling* 52.12 (Dec. 2012), pp. 3155–3168. ISSN: 15499596. DOI: `10.1021/ci3003649`.

[79] Tsjerk A. Wassenaar et al. “Computational lipidomics with insane: A versatile tool for generating custom membranes for molecular simulations”. In: *Journal of Chemical Theory and Computation* 11.5 (May 2015), pp. 2144–2155. ISSN: 15499626. DOI: `10.1021/acs.jctc.5b00209`.

[80] William Humphrey, Andrew Dalke, and Klaus Schulten. “VMD: Visual molecular dynamics”. In: *Journal of Molecular Graphics* 14.1 (Feb. 1996), pp. 33–38. ISSN: 02637855. DOI: `10.1016/0263-7855(96)00018-5`.

[81] Ruxandra I. Dima and D. Thirumalai. “Asymmetry in the shapes of folded and denatured states of proteins”. In: *Journal of Physical Chemistry B* 108.21 (2004), pp. 6564–6570. ISSN: 15206106. DOI: `10.1021/jp037128y`.

[82] Naveen Michaud-Agrawal et al. “MDAnalysis: A toolkit for the analysis of molecular dynamics simulations”. In: *Journal of Computational Chemistry* 32.10 (July 2011), pp. 2319–2327. ISSN: 01928651. DOI: `10.1002/jcc.21787`.

[83] Richard Gowers et al. “MDAnalysis: A Python Package for the Rapid Analysis of Molecular Dynamics Simulations”. In: *Proceedings of the 15th Python in Science Conference*. SciPy, Sept. 2016, pp. 98–105. DOI: `10.25080/majora-629e541a-00e`.

[84] Chandan Kumar Choudhury and Sudip Roy. “Structural and dynamical properties of polyethylenimine in explicit water at different protonation states: A molecular dynamics study”. In: *Soft Matter* 9.7 (Feb. 2013), pp. 2269–2281. ISSN: 17446848. DOI: `10.1039/c2sm26290h`.

[85] Caleb E. Gallops et al. “Effect of the Protonation Level and Ionic Strength on the Structure of Linear Polyethyleneimine”. In: *ACS Omega* 4.4 (Apr. 2019), pp. 7255–7264. ISSN: 24701343. DOI: `10.1021/acsomega.9b00066`.

[86] Titus Adrian Beu, Andrada-Elena Ailenei, and Alexandra Farcaş. “CHARMM force field for protonated polyethyleneimine”. In: *Journal of Computational Chemistry* 39.31 (Dec. 2018), pp. 2564–2575. ISSN: 01928651. DOI: `10.1002/jcc.25637`.

[87] Lucia Ya Zakharova et al. “Nanosized reactors based on polyethyleneimines: From microheterogeneous systems to immobilized catalysts”. In: *Langmuir* 23.6 (Mar. 2007), pp. 3214–3224. ISSN: 07437463. DOI: `10.1021/la0629633`.

[88] Igor Perevyazko et al. “Linear poly(ethylene imine)s: True molar masses, solution properties and conformation”. In: *Polymer Chemistry* 8.46 (Dec. 2017), pp. 7169–7179. ISSN: 17599962. DOI: `10.1039/c7py01634d`.

[89] Monica Bulacu et al. “Improved angle potentials for coarse-grained molecular dynamics simulations”. In: *Journal of Chemical Theory and Computation* 9.8 (2013), pp. 3282–3292. ISSN: 15499618. DOI: `10.1021/ct400219n`.

[90] Monica Bulacu and Erik Van Der Giessen. “Effect of bending and torsion rigidity on self-diffusion in polymer melts: A molecular-dynamics study”. In: *Journal of Chemical Physics* 123.11 (Sept. 2005), p. 114901. ISSN: 00219606. DOI: `10.1063/1.2035086`.

[91] Semen O. Yesylevskyy et al. “Polarizable water model for the coarse-grained MARTINI force field”. In: *PLoS Computational Biology* 6.6 (June 2010), pp. 1–17. ISSN: 1553734X. DOI: `10.1371/journal.pcbi.1000810`.

[92] Nathan W. Schmidt and Gerard C.L. Wong. *Antimicrobial peptides and induced membrane curvature: Geometry, coordination chemistry, and molecular engineering*. Aug. 2013. DOI: `10.1016/j.cossms.2013.09.004`.

[93] Elena Beltrán-Heredia et al. “Membrane curvature induces cardiolipin sorting”. In: *Communications Biology* 2.1 (2019). ISSN: 23993642. DOI: `10.1038/s42003-019-0471-x`.

[94] Semen Yesylevskyy, Timothée Rivel, and Christophe Ramseyer. “Curvature increases permeability of the plasma membrane for ions, water and the anti-cancer drugs cisplatin and gemcitabine”. In: *Scientific Reports* 9.1 (2019). ISSN: 20452322. DOI: `10.1038/s41598-019-53952-2`.

[95] Arnoud H. M. van Vliet, Stefan Bereswill, and Johannes G. Kusters. “Ion Metabolism and Transport”. In: *Helicobacter pylori*. ASM Press, Apr. 2014, pp. 193–206. ISBN: 1555812139. DOI: `10.1128/9781555818005.ch17`.

[96] L.N. Csonka and W. Epstein. “Osmoregulation”. In: *Escherichia coli and Salmonella: Cellular and Molecular Biology*. Ed. by F. C. Neidhardt. 2nd. ASM Press, Washington, D.C., 1996, pp. 1210–1223.

[97] Franklin M. Harold and P. C. Maloney. “Energy transduction by ion currents”. In: *Escherichia coli and Salmonella: Cellular and Molecular Biology*. Ed. by F. C. Neidhardt. 2nd. ASM Press, Washington, D.C., 1996, pp. 283–306.

[98] Hui Guo, Toshiharu Suzuki, and John L. Rubinstein. “Structure of a bacterial atp synthase”. In: *eLife* 8 (Feb. 2019). ISSN: 2050084X. DOI: `10.7554/eLife.43128`.

[99] M. Majtyka and J. Kłos. “Monte Carlo simulations of a charged dendrimer with explicit counterions and salt ions”. In: *Physical Chemistry Chemical Physics* 9.18 (May 2007), pp. 2284–2292. ISSN: 14639076. DOI: `10.1039/b616575c`.

[100] Pedro B.P.S. Reis et al. “Role of Counterions in Constant-pH Molecular Dynamics Simulations of PAMAM Dendrimers”. In: *ACS Omega* 3.2 (Feb. 2018), pp. 2001–2009. ISSN: 24701343. DOI: `10.1021/acsomega.7b01708`.

[101] Mónika Kéri et al. “Beware of phosphate: Evidence of specific dendrimer-phosphate interactions”. In: *Physical Chemistry Chemical Physics* 19.18 (May 2017), pp. 11540–11548. ISSN: 14639076. DOI: `10.1039/c7cp00875a`.

[102] Shiqun Shao et al. “A non-cytotoxic dendrimer with innate and potent anticancer and anti-metastatic activities”. In: *Nature Biomedical Engineering* 1.9 (Sept. 2017), pp. 745–757. ISSN: 2157-846X. DOI: `10.1038/s41551-017-0130-9`.

[103] Carolyn L. Mazzitelli and Jennifer S. Brodbelt. “Investigation of Silver Binding to Polyamidoamine (PAMAM) Dendrimers by ESI Tandem Mass Spectrometry”. In: *Journal of the American Society for Mass Spectrometry* 17.5 (May 2006), pp. 676–684. ISSN: 10440305. DOI: `10.1016/j.jasms.2006.01.010`.

[104] Stephen H. White and William C. Wimley. *Hydrophobic interactions of peptides with membrane interfaces*. Nov. 1998. DOI: `10.1016/S0304-4157(98)00021-5`.

[105] Stephen H. White and William C. Wimley. "Membrane protein folding and stability: Physical principles". In: *Annual Review of Biophysics and Biomolecular Structure* 28 (1999), pp. 319–365. ISSN: 10568700. DOI: `10.1146/annurev.biophys.28.1.319`.

[106] Ryan Bradley and Ravi Radhakrishnan. "Coarse-Grained Models for Protein-Cell Membrane Interactions". In: *Polymers* 5.3 (July 2013), pp. 890–936. ISSN: 2073-4360. DOI: `10.3390/polym5030890`.

[107] Diana A. Kondinskaia et al. "Atomic-Scale Molecular Dynamics Simulations of DNA-Polycation Complexes: Two Distinct Binding Patterns". In: *Journal of Physical Chemistry B* 120.27 (July 2016), pp. 6546–6554. ISSN: 15205207. DOI: `10.1021/acs.jpcb.6b03779`.

[108] Zonghui Wei and Erik Luijten. "Systematic coarse-grained modeling of complexation between small interfering RNA and polycations". In: *Journal of Chemical Physics* 143.24 (Dec. 2015), p. 243146. ISSN: 00219606. DOI: `10.1063/1.4937384`.

[109] Saswati Basu et al. "Mannobiose-Grafting Shifts PEI Charge and Biphasic Dependence on pH". In: *Macromolecular Chemistry and Physics* 220.3 (2019), pp. 1–14. ISSN: 15213935. DOI: `10.1002/macp.201800423`.

[110] Nuno Martinho et al. "Rational design of novel, fluorescent, tagged glutamic acid dendrimers with different terminal groups and in silico analysis of their properties". In: *International Journal of Nanomedicine* Volume 12 (Sept. 2017), pp. 7053–7073. ISSN: 1178-2013. DOI: `10.2147/IJN.S135475`.

[111] Ming Han, Peiquan Chen, and Xiaozhen Yang. "Molecular dynamics simulation of PAMAM dendrimer in aqueous solution". In: *Polymer* 46.10 (Apr. 2005), pp. 3481–3488. ISSN: 00323861. DOI: `10.1016/j.polymer.2005.02.107`.

[112] Sofia E. Mikhtaniuk et al. "Comparison of structure and local dynamics of two peptide dendrimers with the same backbone but with different side groups in their spacers". In: *Polymers* 12.8 (Aug. 2020), p. 1657. ISSN: 20734360. DOI: `10.3390/POLYM12081657`.

[113] Luiz F. Pinto et al. "The dynamics of dendrimers by NMR relaxation: Interpretation pitfalls". In: *Journal of the American Chemical Society* 135.5 (Feb. 2013), pp. 1972–1977. ISSN: 00027863. DOI: `10.1021/ja311908n`.

APPENDIX A - PARTIAL ATOMIC CHARGES

Table A.1: *pei*+ final charges

Residue TPEIQ		Residue PEIQ	
Atom type	Q_{final}	Atom type	Q_{final}
N3	-0.356059	CT	-0.041049
H	0.374141	HP	0.131996
H	0.374141	HP	0.131996
H	0.374141	N3	-0.034268
CT	-0.073587	H	0.294191
HP	0.153611	H	0.294191
HP	0.153611	CT	-0.041049
CT	0.063679	HP	0.131996
HP	0.124669	HP	0.131996
HP	0.124669	-	-
N3	-0.108487	-	-
H	0.299450	-	-
H	0.299450	-	-
CT	-0.055806	-	-
HP	0.126188	-	-
HP	0.126188	-	-
Q_{total}	2.000000	Q_{total}	1.000000

Table A.2: *peis* final charges

Residue TPEIS		Residue PEIQ	
Atom type	Q_{final}	Atom type	Q_{final}
N3	-0.575560	CT	0.360975
H	0.372439	HP	0.009080
H	0.372439	HP	0.009080
H	0.372439	N3	-0.124726
CT	0.375897	H	0.183228
HP	0.041173	H	0.183228
HP	0.041173	CT	0.360975
CT	0.029515	HP	0.009080
H1	0.101535	HP	0.009080
H1	0.101535	-	-
N3	-0.842576	-	-
H	0.392899	-	-
CT	0.024452	-	-
H1	0.096320	-	-
H1	0.096320	-	-
Q_{total}	1.000000	Q_{total}	1.000000

Table A.3: *pein* final charges

Residue TPEI		Residue PEI	
Atom type	Q_{final}	Atom type	Q_{final}
N3	-1.16478800	CT	0.5419245
H	0.4031055	H1	-0.0744985
H	0.4031055	H1	-0.0744985
CT	0.4559390	N3	-1.1244600
H1	-0.0486810	H	0.3386050
H1	-0.0486810	CT	0.5419245
CT	0.4498730	H1	-0.0744985
H1	-0.0379165	H1	-0.0744985
H1	-0.0379165	-	-
N3	-1.1526950	-	-
H	0.3833280	-	-
CT	0.5223930	-	-
H1	-0.0635330	-	-
H1	-0.0635330	-	-
Q_{total}	0.000000	Q_{total}	0.000000

APPENDIX B - FORCE FIELDS PARAMETERS

Table A.1: AMBER final dihedral parameters for all protonation states. Shifts angles ϕ_s in degrees, force constants k_ϕ in kcal/mol and multiplicities n_i.

Dihedral	ϕ_s	k_ϕ	n_i	Dihedral	ϕ_s	k_ϕ	n_i
fully-protonated PEI dihedrals							
N3-CT-CT-N3	180.0	9.50109225	1	CT-CT-N3-CT	180.0	4.96338949	1
	0.0	5.32413790	2		0.0	0.78233765	2
	0.0	6.71726895	3		0.0	5.01396659	3
	0.0	0.86002943	4		0.0	1.06246863	4
semi-protonated PEI dihedrals							
N3-CT-CT-N3	0.0	3.07057930	1	CT-CT-N3-CT	180.0	4.32520846	1
	0.0	0.45577418	2		180.0	1.99217400	2
	0.0	7.93335488	3		0.0	5.37126809	3
	0.0	0.45189333	4		0.0	0.82621376	4
non-protonated PEI dihedrals							
N3-CT-CT-N3	0.0	4.01755461	1	CT-CT-N3-CT	0.0	3.58076517	1
	0.0	6.57331633	3		0.0	2.06481023	2
					0.0	4.77072192	3
					0.0	0.18491141	4
					0.0	0.50829787	5

Table A.2: Martini 3 bond parameters for all PEI models. b_0 in nm and k_b in kJ·mol^{-1}·nm^{-2}.

Fully-protonated			semi-protonated			non-protonated		
Bonds	b_0	k_b	Bonds	b_0	k_b	Bonds	b_0	k_b
TBP-MBP	0.275	13000	TBP-MBN	0.283	20000	TBN-MBN	0.285	12000
MBP-MBP	0.310	15000	MBN-MBP	0.330	8000	MBN-MBN	0.345	8000

Table A.3: Martini 3 bending angle parameters for all PEI models. θ_0 in degrees and k_θ in kJ·mol^{-1}.

Fully-protonated			semi-protonated			non-protonated		
Angles	θ_0	k_θ	Angles	θ_0	k_θ	Angles	θ_0	k_θ
TBP-MBP-MBP	153	250	TBP-MBN-MBP	111	125	TBN-MBN-MBN	125	120
MBP-MBP-MBP	170	225	MBN-MBP-MBN	113	45	MBN-MBN-MBN	112	80
			MBP-MBN-MBP	107	60			

Table A.4: Martini 3 torsion angle parameters for all PEI models. All values in kJ·mol^{-1}.

Dihedrals	k_ϕ	a_0	a_1	a_2	a_3	a_4
Fully-protonated						
TBP-MBP-MBP-MBP	75	1.41	2.95	1.36	1.33	1.00
MBP-MBP-MBP-MBP	65	1.41	2.95	1.36	1.33	1.00
semi-protonated						
TBP-MBN-MBP-MBN	4	4.00	-3.00	-1.00	0.50	0.50
MBN-MBP-MBN-MBP	4	3.00	0.00	-1.25	-1.25	0.00
Non-protonated						
TBN-MBN-MBN-MBN	10	2.41	-2.00	0.00	1.00	0.00
MBN-MBN-MBN-MBN	10	2.41	-2.00	0.00	1.00	0.00

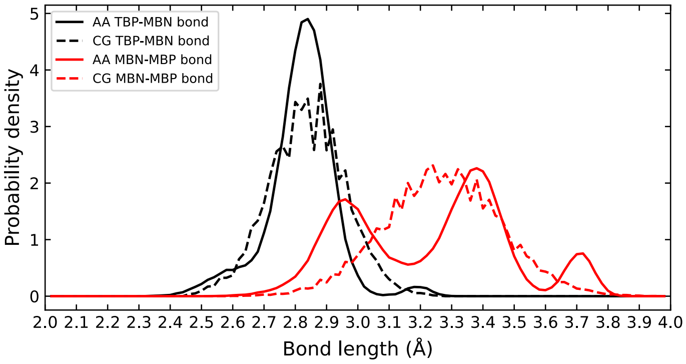

Figure A.1: Atomistic (solid) and CG (dashed) probability distribution for the TBP-MBN (black) and MBN-MBP (red) bead bond distances of semi-protonated PEI.

Table A.5: Martini 3 bond and angle parameters for Polyurea models. b_0 in nm, k_b in kJ·mol^{-1}·nm^{-2}, θ_0 in degrees and k_θ in kJ·mol^{-1}.

Bonds			Angles		
Bonds	b_0	k_b	Angles	θ_0	k_θ
AM-UR	0.467	5000	AM-UR-AM	180	80
AM-NT	0.260	6500	UR-AM-UR	130	30
NT-NT	0.425	1750	UR-AM-NT	50	50
			NT-AM-NT	117	40

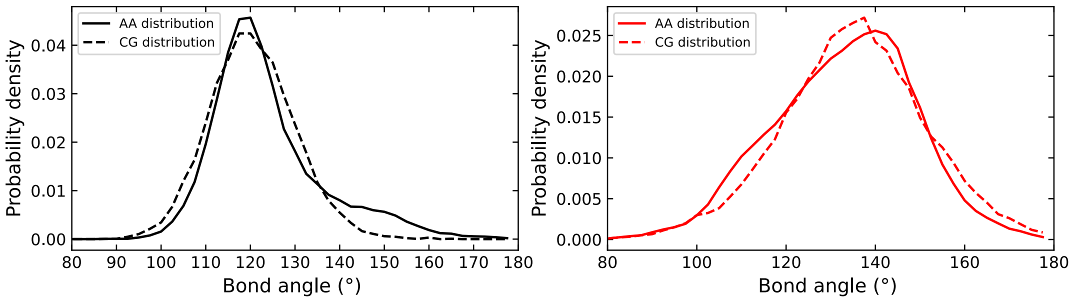

(a) TBP-MBN-MBP bending angle distribution.

(b) MBN-MBP-MBN bending angle distribution.

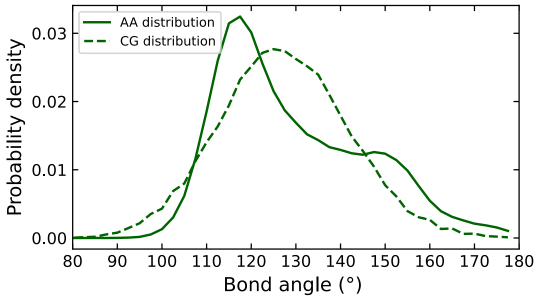

(c) MBP-MBN-MBP bending angle distribution.

Figure A.2: Atomistic (solid) and CG (dashed) probability distribution for the TBP-MBN-MBP (black), MBN-MBP-MBN (red) and MBP-MBN-MBP (green) bending angles of semi-protonated PEI.

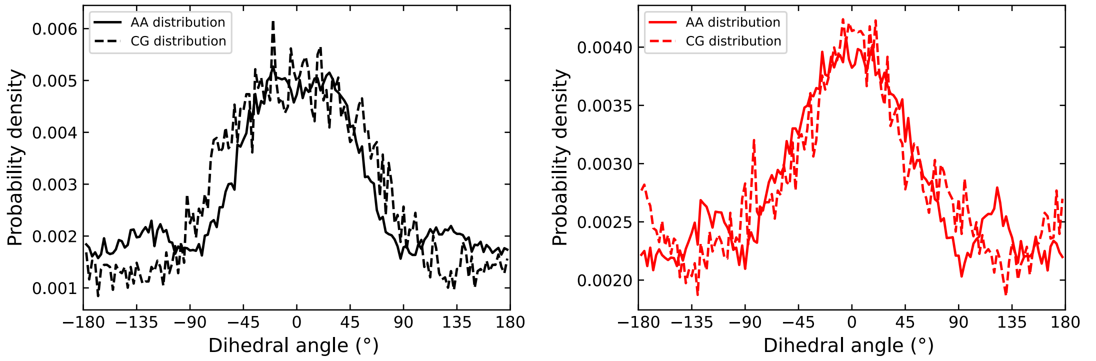

(a) TBP-MBN-MBP-MBN torsion angle distribution.

(b) MBN-MBP-MBN-MBP torsion angle distribution.

Figure A.3: Atomistic (solid) and CG (dashed) probability distribution for the TBP-MBN-MBP-MBN (black) and MBN-MBP-MBN-MBP (red) dihedral angles of semi-protonated PEI.

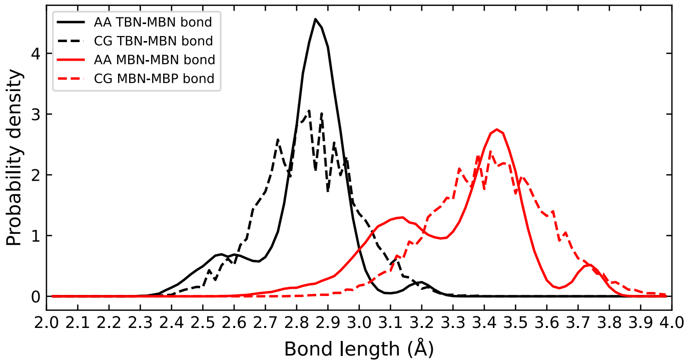

Figure A.4: Atomistic (solid) and CG (dashed) probability distribution for the TBN-MBN (black) and MBN-MBN (red) bead bond distances of non protonated PEI.

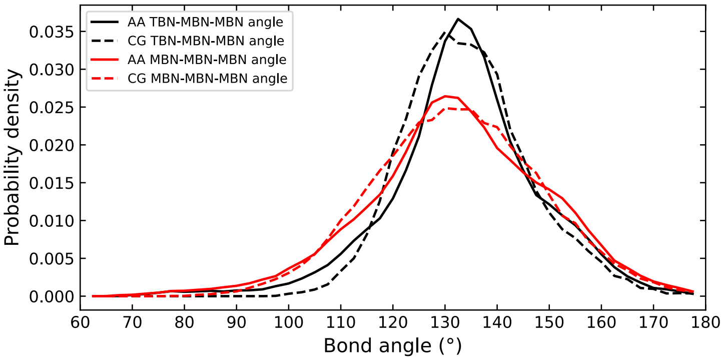

Figure A.5: Atomistic (solid) and CG (dashed) probability distribution for the TBN-MBN-MBN (black) and MBN-MBN-MBN (red) bending angles of non protonated PEI.

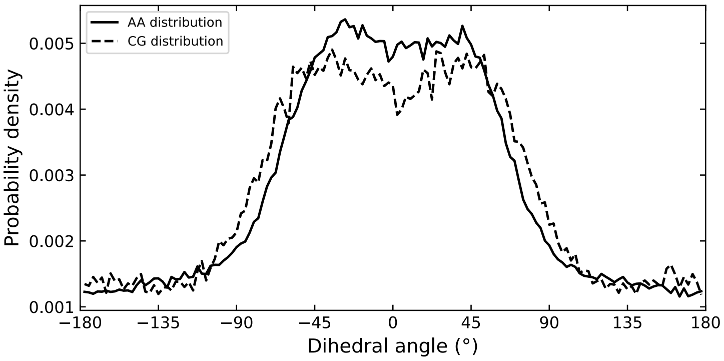

Figure A.6: Atomistic (solid) and CG (dashed) probability distribution for all the dihedrals angles of non protonated PEI.

APPENDIX C - RDF PLOTS

Radial distribution function plots for semi- and non-protonated PURE$_{G4}$-OEI$_{48}$

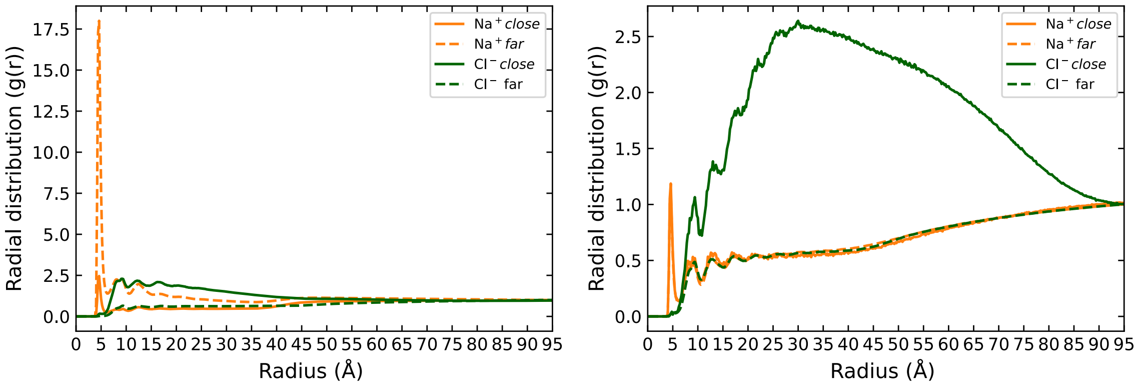

(a) Original nanoparticle at POPC/POPG

(b) Original nanoparticle at POPC

Figure A.1: Radial distribution function of ions around outer leaflet of membranes under presence of semi-protonated PURE$_{G4}$-OEI$_{48}$.

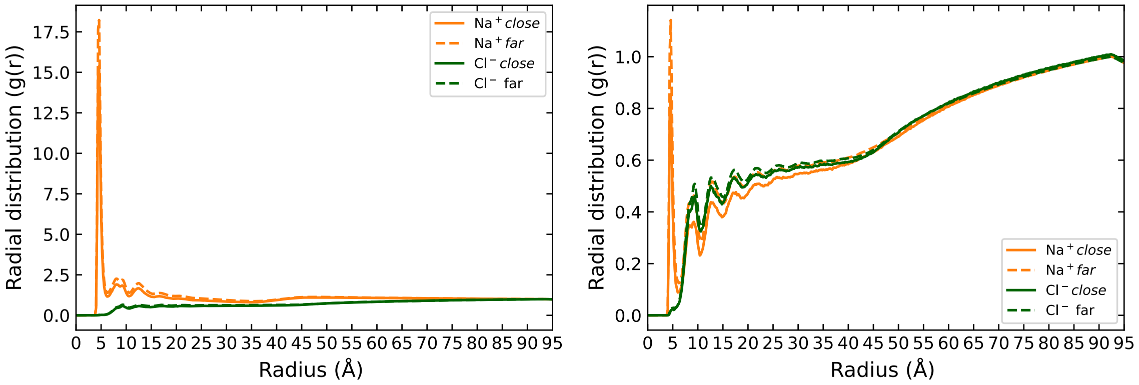

(a) Original nanoparticle at POPC/POPG

(b) Original nanoparticle at POPC

Figure A.2: Radial distribution function of ions around outer leaflet of membranes under presence of non-protonated PURE$_{G4}$-OEI$_{48}$.

Radial distribution function plots for all modifications

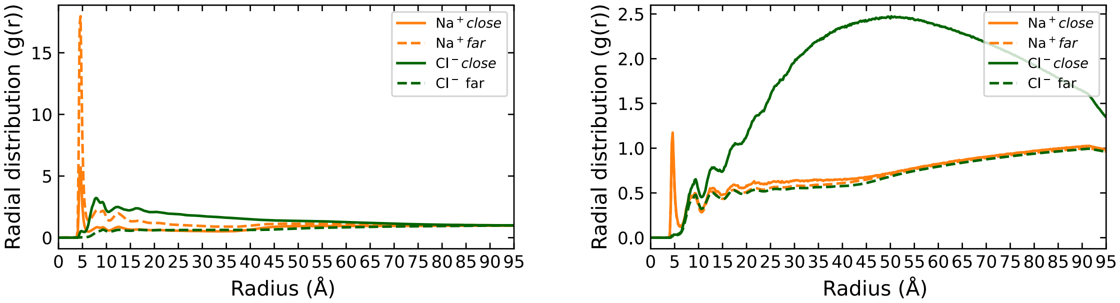

(a) Fully Leucine modification at POPC/POPG

(b) Fully Leucine modification at POPC/POPG

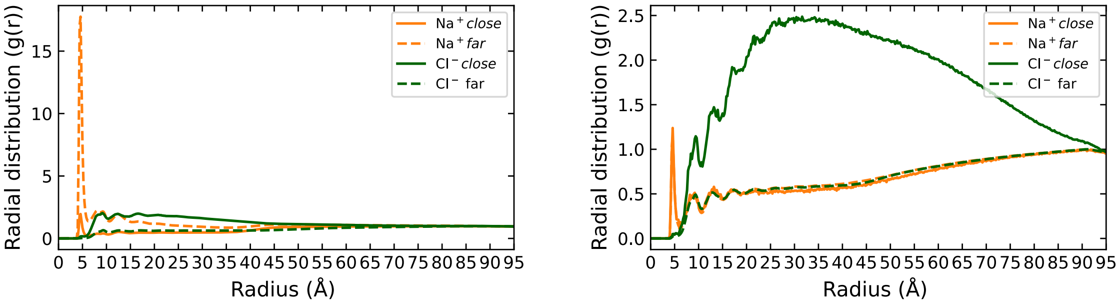

(c) Semi Leucine modification at POPC/POPG

(d) Semi Leucine modification at POPC/POPG

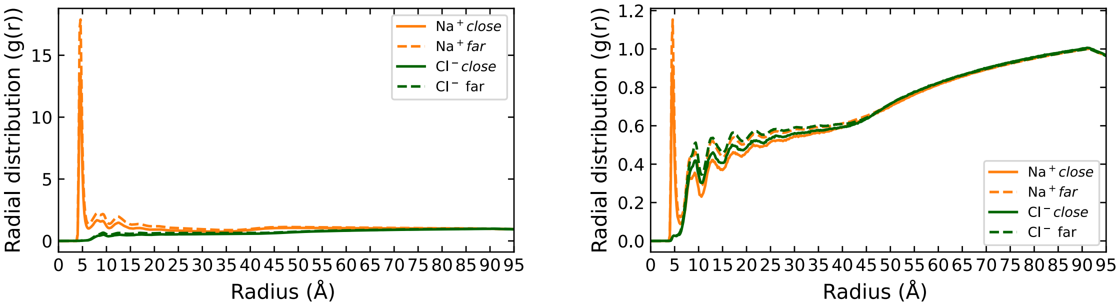

(e) Non Leucine modification at POPC/POPG

(f) Non Leucine modification at POPC/POPG

Figure A.3: Radial distribution function of ions around outer leaflet of membranes under presence of all Leucine modification PURE$_{G4}$-OEI$_{48}$.

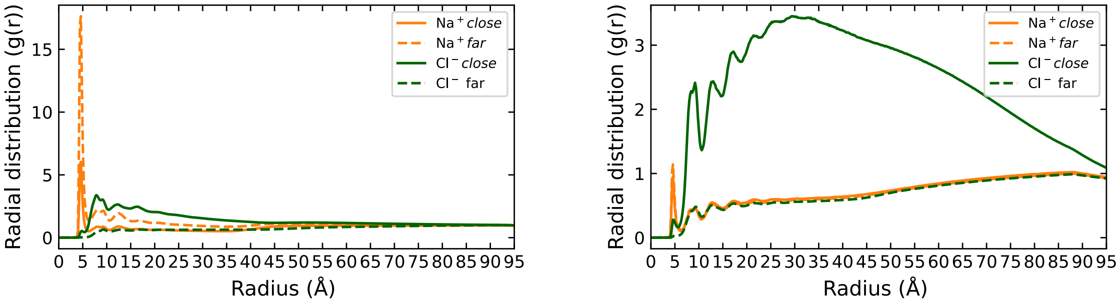

(a) Fully Phenylalanine modification at POPC/POPG (b) Fully Phenylalanine modification at POPC/POPG

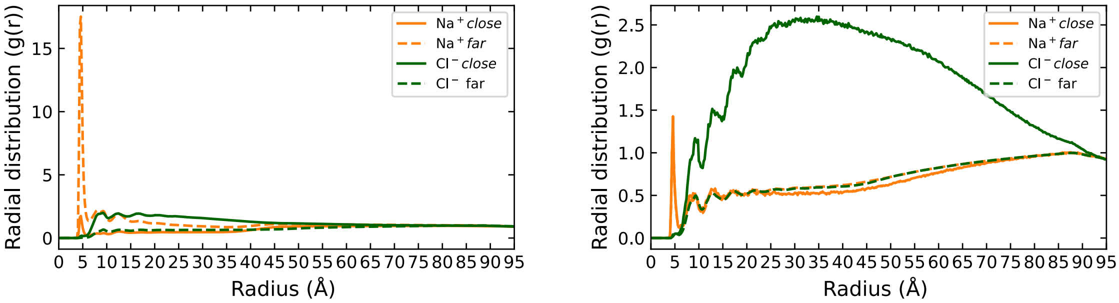

(c) Semi Phenylalanine modification at POPC/POPG (d) Semi Phenylalanine modification at POPC/POPG

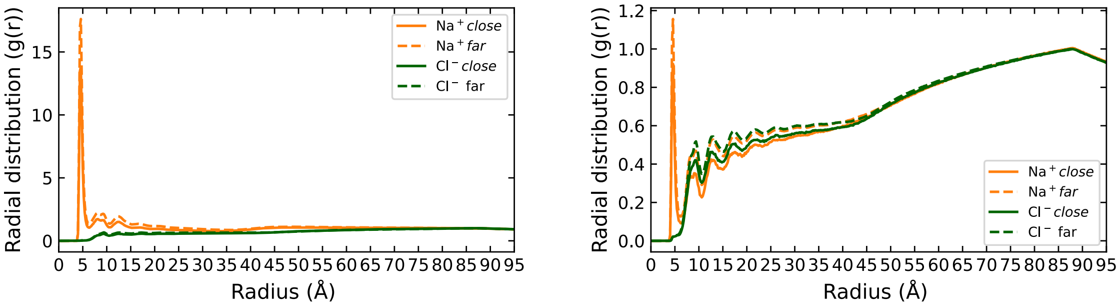

(e) Non Phenylalanine modification at POPC/POPG (f) Non Phenylalanine modification at POPC/POPG

Figure A.4: Radial distribution function of ions around outer leaflet of membranes under presence of all Phenylalanine modification PURE$_{G4}$-OEI$_{48}$.

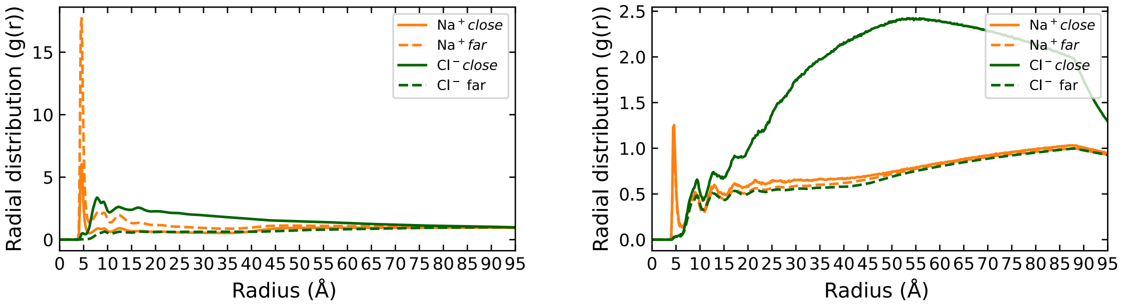

(a) Fully Tryptophan modification at POPC/POPG

(b) Fully Tryptophan modification at POPC/POPG

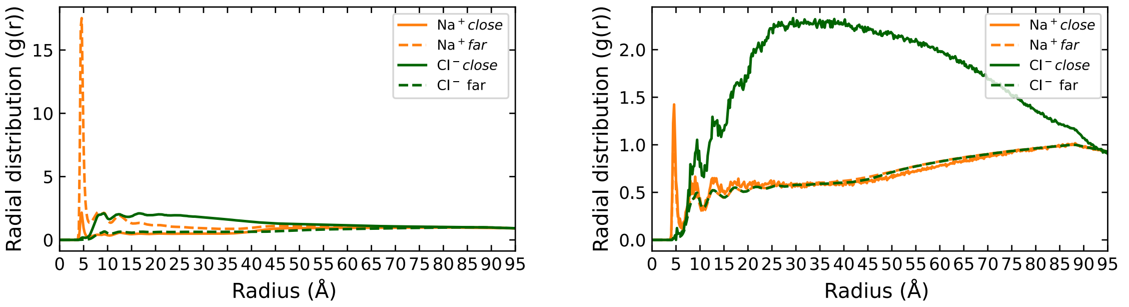

(c) Semi Tryptophan modification at POPC/POPG

(d) Semi Tryptophan modification at POPC/POPG

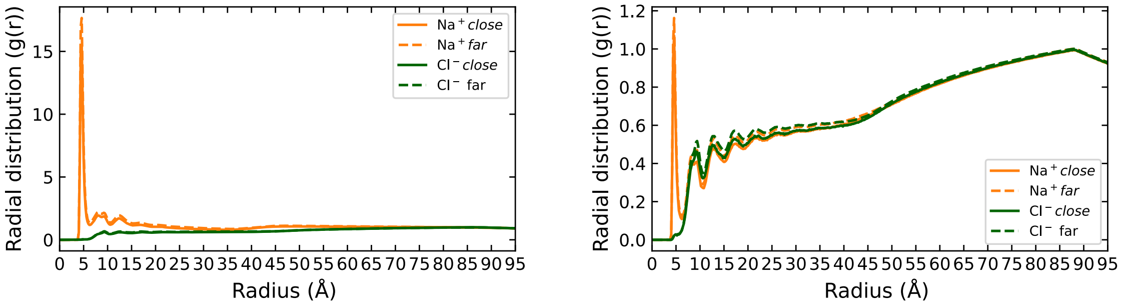

(e) Non Tryptophan modification at POPC/POPG

(f) Non Tryptophan modification at POPC/POPG

Figure A.5: Radial distribution function of ions around outer leaflet of membranes under presence of all Tryptophan modification PURE$_{G4}$-OEI$_{48}$.